Dynamical impacts on marine ecosystem of coastal and marginal seas around Japan

ZHANG, XU

(Degree)
博士（学術）

(Date of Degree)
2021-03-25

(Date of Publication)
2023-03-25

(Resource Type)
doctoral thesis

(Report Number)
甲第8066号

(URL)
https://hdl.handle.net/20.500.14094/D1008066

Doctoral Dissertation

Dynamical impacts on marine ecosystem of coastal and marginal seas around Japan

日本の沿岸および周辺海域における海洋生態系への力学的影響

January 2021

Graduate School of Engineering,
Kobe University
ZHANG XU

Doctoral Dissertation

Dynamical impacts on marine ecosystem of coastal and marginal seas around Japan

日本の沿岸および周辺海域における海洋生態系への力学的影響

January 21, 2021

Department of Civil Engineering
Graduate School of Engineering
Kobe University
ZHANG XU
167T142T

Dynamical impacts on marine ecosystem of coastal and marginal seas around Japan

ZHANG XU
167T142T
Department of Civil Engineering
Graduate School of Engineering
Kobe University

January 21, 2021

Abstract

Ocean covers over 70% of the Earth's surface and is among the most productive ecosystems in the world. Marine ecosystem is an open system that is affected by currents, seasons and other oceanographic processes and provides essential goods and services for human being. Japan is an island country in East Asia situated in the northwest Pacific Ocean, where the local marine ecosystem is broadly influenced by anthropogenic and biological process in coastal and marginal seas.

The Seto Inland Sea (SIS) is the largest semi-enclosed estuary in Japan. The Kuroshio has a considerable impact on the SIS circulation due to sporadic intrusions and meandering of the Kuroshio path. This area is taken out for the current study about anthropogenic impacts on the marine ecosystem, because approximate 24% of Japan's population resides within its watershed basins, leading to heavy nutrient loading of the SIS and thus an increased occurrence of harmful algal bloom. The Tarumi Sewage Treatment Plant (TSTP), one of the largest wastewater treatment plants in Osaka Bay, is located near the narrow Akashi Strait with complex tidal flows, having possible impacts on seaweed farming. On the other hand, the natural biological processes have more extensive and complex impacts on the marine ecosystem. Carbon exchange between the atmosphere and ocean substantially regulates the climate change. The biogeochemistry controls and feedbacks on global ocean primary productivity. Carbon cycling in the coastal waters is a major component of global carbon cycles and budgets. The Kuroshio is one of the most energetic western boundary currents accompanied by vigorous eddy activity at mesoscale and submesoscale, significantly affecting the primary productivity in the Kuroshio Region (KR) and Kuroshio Extension (KE) regions. Historically, there are abundant researches concerning the influences of vertical nitrate transport on the primary productivity. However, studies on the seasonal variability of the primary production in the KR and KE are limited particularly in conjunction with the Kuroshio currents affected by the ridge topography in the KR.

Nutrient transport is one of key influencers in the marine ecosystem. We consider the nutrient source from two major aspects, sewage from treatment plant located in estuary and upward entrainment to surface layer from subsurface in the open sea area.

The sewage transport is noticeably affected by the tidal current in estuarine region. By contrast, the vertical eddy-induced nutrient upwelling is an essential source to maintain the primary production, further affecting human being's life on global scale. Therefore, the researches concerning primary production in the coastal seas are important for marine ecosystem-based management, spatial planning for the future. In the present study, we aim to examine possible driving mechanisms in Osaka Bay, an estuarine area with densely population. We also quantify the impact of the diversion of sewage effluent on the seaweed farm and possible improvement with different discharge operations to examine the anthropogenic effect on marine ecosystem. In addition, to understand the biological processes in the coastal seas, we analyze the seasonal variability of the eddy-driven vertical nutrient fluxes that play essential roles in maintaining the upper-ocean primary production, as well as its driving mechanisms in the KR and KE regions.

In Section 2, we developed a quadruple-nested, high-resolution model with a horizontal of 20 m based on Regional Oceanic Modeling System (ROMS). A Eulerian near-field effluent dilution model was employed to reproduce 3-D advection-dispersion processes of the under-resolved, bottom-released buoyant effluent plume at the TSTP. In addition, in Section 3, we conducted two more alternative scenarios to assess the impacts of wastewater effluents from the standard diversion outfall by reducing the sewage discharge rate and changing the wastewater density. A twin numerical experiment for cases with normal and western diversion outfalls of the TSTP enabled us to quantitatively evaluate the effect of the diversion. The effluent flux budget analysis revealed that the cumulative nondimensional effluent of the seaweed farm is reduced by ~0.81×10^4 m^3 on average compared with that of the normal outfall (~2.83×10^4 m^3), exhibiting a ~28% reduction of the effluent from the TSTP by the diversion, which could lead to favorable influences on the growth of seaweeds. Based on above conclusion, two more operations were set up to analyze the effects of sewage discharge rate and sewage density. We discovered that 16.7% of the wastewater discharge rate decreased from the standard diversion operation resulted in an overall 25.4% reduction in the sewage effluent accumulating on average in the seaweed farm. In turn, the addition of ambient seawater to the freshwater effluent did not substantially alter the effluent accumulation and associated hydrodynamics at the farm.

We have understood the anthropogenic impacts on the marine ecosystem in our research domain. In turn, the natural biological processes are summarized as follows. Carbon cycling in the coastal waters is a major component of global carbon cycles and budgets, further affecting the climate. Therefore, we enlarged our study area to focus on the impacts of upward eddy-induced nitrate transport on the marine ecosystem in the following two sections. Section 4 investigated seasonal variability of eddy fluxes that sustain the upper ocean primary productions and the driving mechanisms behind them in the KR and KE regions. To this end, we conducted a submesoscale eddy-permitting ocean modeling based on ROMS coupled with a nitrogen-based NPZD biogeochemical model,

including the KR and KE regions. Furthermore, in Section 5, a synoptic, retrospective downscaling ocean modeling was developed to investigate inter-annual variability of vertical eddy-induced nutrient fluxes, when several large meanders occur in the KR. We found the segmentations of surface chlorophyll-a (Chl-a) on both sides of the Kuroshio with a higher Chl-a concentration on the northern area. Enhanced vertical mixing in winter and subsequent improvement of the light condition in spring results in active primary productions around the Kuroshio both in the KR and KE. The overall upward entrainment from the nutrient-rich subsurface to the nutrient-exhausted surface is substantial for maintaining the near-surface primary productivity. However, a downward eddy nitrate fluxes are found in winter in the upstream (Enshu-nada Sea region) and the downstream regions relative to the ridge in the KR. In winter, the topographic eddy shedding, positive barotropic conversation rate (K_mK_e), and baroclinic conversion rate (P_eK_e) jointly promote eddy-driven downward nitrate fluxes through shear instability and baroclinic instability along the Kuroshio path and its northern side in the KR. In the KE, upward eddy flux due to the combination of positive K_mK_e and P_eK_e enhances the primary production in the upper ocean. By contrast, in summer, the mixed layer depth becomes very shallow and thus makes the upper ocean P_eK_e almost vanish in both KR and KE. Positive K_mK_e and P_eK_e arise mostly at depth beneath the mixed layer, which considerably interact with the ridge topography in the KR to increase in the upstream while decrease in the downstream regions. In the KE, as P_eK_e is prominently reduced in summer, eddy nitrate flux is decreased significantly in particular on the north of the Kuroshio. Therefore, baroclinic instability is the key influencer on seasonal variability in eddy generation near the surface, where vertical eddy mixing is inevitably important to promote the subsurface nutrient supply to the upper ocean. In addition, impacts of the oceanic ridge (Izu-Ogasawara Ridge) are examined in the KR. Turbulence associated with the Kuroshio trends to be less energetic in the upstream, while the ridge generates intensive eddy mixing more broadly and deeply in the downstream mainly due to the interaction between the Kuroshio front and ridge topography that results in mesoscale eddy-generating baroclinic instability. We detected three obvious meanders during our analysis period with the synoptic configuration. When the meander happens in summer, more significant nitrate depletion occurs in the surface layer, resulting in relative weak primary productivity but larger distribution. In the offshore region, mean and transient nitrate flux decreases during the meander, while diffusive flux plays important role in maintaining nutrient upwelling near surface. In the coastal part, mean component is essential for the active primary production during the meandering.

Contents

1 Introduction

Ocean covers over 70% of the Earth's surface and is among the most productive ecosystems in the world. Marine ecosystem is an open system that is affected by currents, seasons and other oceanographic processes and provides essential goods and services for human being. Japan is a developed and island country in East Asia situated in the northwest Pacific Ocean, so that Japan relies on marine much more than other countries. It is worth understanding how the local marine ecosystem is influenced by anthropogenic and natural biological impacts in the coastal and marginal seas around Japan. In the present study, we focus on two types of unique research areas, estuarine area and open seas region.

The Seto Inland Sea (SIS) is the largest semi-enclosed estuary in Japan, encompassing a total water area of 23,203 km^2.It has unique geographical characteristics and consists of seven main sub-basins interconnected by narrow straits and > 3000 islands, which form a complex "basin-strait" system. The SIS is a partially stratified tidal estuary that is concurrently affected by: 1) energetic tidal currents up to 3 m s^{-1} near straits (Fujiwara et al., 1994) under dominant semidiurnal, mesotidal conditions with a maximum tidal range of ± 1.2 m; 2) seasonally varying freshwater discharge from 28 major rivers; and 3) quasi-persistent eastward residual circulation (the SIS through-flow) primarily driven by the eastward drifting Kuroshio offshore of the two openings that connect the SIS with the Pacific (e.g., Kosako et al., 2016). The Kuroshio is known to have a considerable impact on the SIS circulation due to sporadic intrusions (Takeoka et al., 1993; Tada et al., 2017) and meandering of the Kuroshio path (e.g., Kawabe, 1987, 1995). In such a strait-basin system, the water is well mixed near straits due to strong tidal currents, while it is rather stratified in basins under more quiescent conditions (e.g., Guo et al., 2004; Chang et al., 2009). Approximately 24% of Japan's population resides within its watershed basins (Tsuge and Washida, 2003), which leads to heavy nutrient loading of the SIS (Miller et al., 2010) and thus an increased occurrence of harmful algal bloom (HABs; e.g., Imai et al., 2006). Historically, the SIS has been extensively used by fisheries and in aquaculture, although it is viewed as a general dumpsite for wastewater from sewage treatment plants. This has caused the critical deterioration of the water quality and coastal marine ecosystems for many years (Tsujimoto et al., 2006). The number of "red tide" events due to HAB, an indicator of eutrophication, has raised remarkably with the in- creased nutrient loading (Takeoka, 2002; Imai et al., 2006). Red tides have occurred much more frequently and in a larger area in the SIS since the 1960s due to Japan's economic development and the associated pollutant emission, with the maximum of 299 incidents in 1976 (Imai et al., 2006). The aquaculture and marine ecosystem have been seriously affected by deterioration. Terawaki et al. (2003) reported that ~6400 ha of seaweed and seagrass beds along the Japanese coast have been destroyed from 1978 to 1991. A series of environmental preservation policies that regulate the total amount of

nitrogen and phosphorus in effluent has been enacted, which had adequately improved the water quality in recent years (Tomita et al., 2016). However, deterioration is not entirely avoidable; ~100 red tides have occurred per year in the SIS since the 2000s. Osaka Bay, located in the eastern part with the most densely populated hinterland around the SIS, still suffers from severe water pollution.

On the other hand, as compared with anthropogenic influence, the natural biological processes have more extensive and complex impacts on the marine ecosystem. Carbon exchange between the atmosphere and ocean substantially regulates the climate change. Previous studies have reported that approximately one-half of total CO_2 emission is taken up by the combination of terrestrial and marine carbon reservoirs (e.g., Schinel et al., 2001; Ballantyne et al., 2012). Nellemann et al. (2009) reported 55% of all the biological carbon is captured by marine living organisms, commonly referred to as "blue carbon". Falkowski et al. (1998) analyzed the biogeochemical controls and feedbacks on global ocean primary productivity. Carbon cycling in the coastal waters is a major component of global carbon cycles and budgets (Bauer et al., 2013). The researches concerning biological processes are important for marine ecosystem-based management, spatial planning and policy development. In general, localized upwelling due to mesoscale cyclonic eddies brings nutrient-rich subsurface water to the surface to enhance near-surface primary productivity. Particularly in the deep ocean, the subsurface nutrients are the only source, which are greatly influenced by vertical transport due to eddies-induced localized upwelling (e.g., Falkowski et al., 1991). Satellite observations revealed that the spatial variability in the surface chlorophyll is distributed on both mesoscale and submesoscale. In addition to observations, numerical simulations have also been conducted with particular concerns about biological responses to the mesoscale and submesoscale variability. It has been recognized that the biogeochemical cycles could be affected by mesoscale eddies in the upper ocean (e.g., Chelton et al., 2011; Gaube et al., 2013). For instance, Lee and Kim (2018) investigated the regional variability and turbulent characteristics of submesoscale surface chlorophyll concentrations, showing the spring (fall) blooms are more active on the near-shore side due to the stronger submesoscale horizontal shear and vertical processes that increase the vertical mixing. Liu and Levine (2015) also concluded that chlorophyll concentration is increased by 38% on average (83% maximum) at submesoscale during the cold season in the North Pacific Subtropical Gyre. The offshore transport of nutrients and carbon driven by filaments and mesoscale eddies in the California Current System was discussed based on a coupled physical-biogeochemical model in a climatological configuration (Nagai et al., 2015). In contrast, a climatological modeling study has revealed that topographic eddy shedding as well as baroclinic instability around the Kuroshio front concurrently promote diapycnal eddy-driven downward nutrient transport in the Enshunada Sea, Japan (Uchiyama et al., 2017). This downward transport competes with upwelling-induced nutrient supply, substantially suppressing the upper-ocean primary productivity.

The Kuroshio is one of the most energetic western boundary currents accompanied by vigorous eddy activity at mesoscale and submesoscale. It originates from the eastern area of the Philippines, drifts northward along the East China Sea shelf, and veers northeastward to flow past the southern coast of Japan. Then the Kuroshio separates from the shelf near 140°E and 35°N, forming a free jet known as the Kuroshio Extension in the North Pacific Ocean (Kawai, 1972; Qiu, 2002). Both nutrient concentrations and their inventories in the northern South China Sea is affected by abrupt Kuroshio intrusions through the Luzon Strait significantly on spatial and seasonal scales (Du et al., 2013). A total annual nitrogen input due to the frontal eddies could result in a carbon production rate of 40 g C m^{-2} y^{-1} in the Enshunada Sea (Kimura et al., 1997; Nakata et al., 2000). Kaneko et al. (2013) reported that segmentation of vertical nitrate fluxes on both sides of the Kuroshio is observed in the Kuroshio region (hereinafter referred to as KR**)**. Kodama et al. (2014) analyzed the seasonal and spatial variability of the nitrate concentration in the upper ocean along 138°E in the KR with a higher value in winter. In the eastern part of the KR, the Kuroshio passes over the Izu-Ogasawara Ridge, a unique shallow topography consisting of two major island chains located off the south coast of Japan along 140–141°E. Sugimoto and Hanawa (2012) reported the Kuroshio tends to be unstable in the downstream after it passes over the shallower part of the ridge with a depth of ~1000 m, leading to intense eddy mixing. Studies on the volume transport of the Kuroshio (e.g., Isobe and Imawaki, 2002) and the westward eddies propagation near the Izu-Ogasawara ridge (e.g., Ebuchi and Hanawa, 2001; Xu et al., 2016) have been extensively conducted in spite of lack of the biogeochemical connections to a large degree. On the contrary, in the Kuroshio Extension (KE) region, primary production in spring is occasionally lowered by a lack of nitrate and silicic acid (Nishibe et al., 2015). Intermittent nutrient transports induced by ageostrophic vertical circulation and mixing have been detected on time scale of a few days near the Kuroshio front in the KE (Clayton et al., 2014) due to the combination of the diabatic turbulence and the adiabatic subduction (Nagai et al., 2012). The importance of cyclonic (anticyclonic) eddy generation and related eddy core migration for enhancement (reduction) of phytoplankton production in the KE has been discussed (e.g., Sasai et al., 2010; Kouketsu et al., 2014).

There are abundant studies concerning seasonal and interannual variability of the primary production and related parameterization including that was conducted by Uitz et al. (2010), who analyzed the seasonal and interannual variability of global phytoplankton class-specific primary production. Analyses in several specific regions have been also carried out. For example, subsurface chlorophyll maxima are seasonal features and have strong effects on depth-integrated primary production estimates in the Arctic Ocean when the surface nitrate is depleted, while its inter-annual variability is very limited (Ardyna et al., 2013). Lomas et al. (2012) reported seasonal primary production on the Eastern Bering Sea shelf in spring and summer 2008 and 2009, concluding that the integrated rate of net primary production is generally lower in summer, while the phytoplankton growth

rate is higher. The pattern of seasonally integrated primary production dynamics in the Kara Sea, Russia, was discussed based on the satellite data obtained in 2003–2015 (Demidov et al., 2017). The seasonal variability of the integrated net primary production dominates over the inter-annual signal in the Mediterranean Sea (Lazzari et al., 2012).

We have introduced two kinds of typical topographies in marine environment. In the semi-enclosed estuary (viz., Osaka Bay), the sewage from treatment plant (viz., Tarumi Sewage Treatment Plant, TSTP) is the major the nutrient source, resulting in serious oceanic pollution and reduced aquaculture production. The TSTP is situated in the 3.6 km narrow Akashi Strait with a maximum depth of 140 m and prevailing energetic and complex tidal flow. A sandbank known as the "Okinose" shoal with the shallowest depth of 23 m is formed southeast of the strait, influenced by intense tidal currents and residual clockwise circulation (Fujiwara and Nakata, 1991; Fujiwara et al., 1994). The area around the Akashi Strait is famous for seaweed farming in the nation. Edible seaweed ("nori" in Japanese) is very common in Asia, which is made from a type of red algae, Porphyra, including widely cultivated Porphyra yezoensis and Porphyra tenera (Niwa and Aguga, 2006). Local fishermen keep complaining about the possible impact from sewage effluent on seaweed farming to the east of the TSTP. In seaweed farming, spores are rather vulnerable to the surrounding environment, in particular to nutrients and salinity.

To avoid overdose that stunts seaweeds, a reduction of nutrients in the effluent is inevitable in fall. The City of Kobe, the local government, has constructed a new western diversion outfall 500 m away from the central normal outfall in the TSTP to reduce the possible impact of the effluent on farming by seasonal diversion from October to December. Bricker et al. (2006) described the general behavior of wastewater released from the western outfall of the TSTP based on conductivity, temperature, and depth (CTD) field measurements for one M_2 tidal cycle under mixed influences from riverine water from the adjacent small stream (Fukuda River). Bricker and Nakayama (2007; hereinafter BN07) further diagnosed the sewage effluent transport and diffusion from dilution quantified based on the filtered temperature and salinity fields that enable the separation of wastewater from ambient seawater influenced by the stream. Although both studies were conducted over a short duration under well-mixed winter conditions without any consideration of the normal outfall, the far-field freshwater plume behaves like those in a canonical open channel flow with respect to the vertical mixing, while horizontal mixing occurs with a diffusivity two (one) orders of magnitude larger than that of meandering (straight) channel flows. They anticipated that the estimated large lateral diffusivity may be due to topographically generated eddies, transient tidal flow, and baroclinicity in the buoyant plume. However, the effects of the western diversion have not been fully investigated, particularly in comparison to the case with effluent from the normal outfall. Multi-nested high-resolution numerical ocean modeling is useful to examine the far-field dispersal of effluent under such complex dynamical conditions. Uchiyama et al. (2014) comprehensively assessed the effects of diversion and dispersal of effluent with a

quadruple-nested ocean circulation model coupled with a buoyant plume and passive Eulerian tracer in an open ocean configuration for Southern California bays. They found that lateral mixing and the associated effluent dispersal predominantly occur with submesoscale turbulence rather than tidal mixing.

In the present study, we firstly assess the dilution and far-field dispersal of the bottom-released buoyant effluent discharged from the central and western outfalls corresponding to normal and diversion discharges at the TSTP. We expect to quantitatively compare two scenarios when the treated wastewater is released from different outfalls, although the distance between the two outfalls is only 500 m in the alongshore direction. After that, based on the local government's requests, two more potential plans are discussed to reduce the TSTP influences on the seaweed farm. We check whether the environment improves, when 1) the discharged volume rate was decreased; 2) the sewage density was changed by mixing with the ambient seawater. Osaka Bay, located in the SIS, is strongly affected by the through-flow due to the Kuroshio. The marine ecosystem is also impacted by the nutrient stream from open seas in Osaka Bay except the land-derived nutrient source. Therefore, we enlarge the study area to compass the KR and KE regions to analyze the biogeochemical processes in regional seas. In the open sea area, the impacts from natural biological processes are more noticeable. The eddy-induced nitrate upwelling plays a dominant role on maintaining primary production, which is important for global carbon circles. There are abundant researches about the primary productivity in the KR and KE. However, studies on the seasonal variability of the primary production in the KR and KE are limited particularly in conjunction with the Kuroshio currents affected by the ridge topography in the KR. We concentrate on how the seasonal vertical nutrient transport impact the upper ocean primary production, and difference between the upstream and downstream regions relative to the Izu-Ogasawara Ridge.

Therefore, we aim to examine possible driving mechanisms in Osaka Bay, an estuarine area with densely population. We also quantify the impact of sewage effluent of the diversion on the seaweed farm and possible improvement with different discharge operations to examine the anthropogenic effect on marine ecosystem. In addition, to understand the biological processes in the coastal seas, we analyze the seasonal variability of the eddy-driven vertical nutrient fluxes that play essential roles in maintaining the upper-ocean primary production, as well as its driving mechanisms in the KR and KE regions. Especially, we will emphasize the impacts of an oceanic ridge (Izu-Ogasawara ridge) on the Kuroshio currents and the associated biogeochemical responses in the KR. At last, we concentrate on the biological responses to the physical surrounding during the Kuroshio meandering.

This thesis is organized as follows. Section 2 confirms the improvement of the western diversion outfall of the TSTP on the local marine ecosystem and gives the related driving mechanisms. Section 3 focuses on scientific insights and qualitative guidelines

on the alternative discharge operations for reducing the TSTP influence on the farm. Section 4 illustrates the seasonal variability of eddy-driven nitrate fluxes that maintain the upper ocean primary productivities and the associated driving mechanisms in the KR and KE regions, particularly in conjunction with the Kuroshio currents affected by the ridge topography in the KR. Section 5 investigates the inter-annual variability of surface primary production because of the Kuroshio meander.

We developed three models to research the above problems. It should be noted that all the outer-most initial and boundary conditions were provided by the assimilative Japan Coastal Ocean Predictability Experiments (JCOPE2) oceanic reanalysis (Miyazawa et al., 2009) in each model. First of all, in Section 2 and Section 3, we conducted a multi-nested, high-resolution, synoptic ocean circulation modeling based on Regional Oceanic Modeling System (ROMS; Shchepetkin and McWilliams, 2005; 2008) to assess the dilution and far-field dispersal of the bottom-released buoyant effluent discharged from the central and western outfalls corresponding to normal and diversion discharges at the TSTP. We primarily aimed to examine possible driving mechanisms of the flow field near the TSTP and to quantify the impact of the diversion of sewage effluent on the seaweed farm. Section 2 investigated the detailed study about the improvement of the western diversion outfall as compared with the central normal outfall, while Section 3 did the further analysis concerning the reduction of the TSTP influence in the western diversion outfall by reducing the discharged volume and adjusting the effluent density and provided optimization plans to reduce the TSTP influences on the seaweed farm. By contrast, to understand the natural biological process, a more complex coupled hydrodynamic-biogeochemical model is necessary. To this end, in Section 4, we employed a high-resolution model based on ROMS coupled with a nitrogen-based NPZD (Nutrient, Phytoplankton, Zooplankton, and Detritus) biogeochemical model described in Fasham et al. (1991). The model encompasses both the KR and KE regions with horizontal grid spacing of 3 km and is run in a climatological configuration for 10 years. This model was originally developed and validated in the preceding study (Uchiyama et al., 2017). This section focuses more on the seasonal variability of the eddy-driven vertical nutrient fluxes that play essential roles in maintaining the upper-ocean primary production, as well as its driving mechanisms in the KR and KE regions with emphasis on the ridge topography. Above climatological model can only provide periodic output results. Therefore, in Section 5, a synoptic, retrospective downscaling ocean modeling is developed for the marginal seas along the Kuroshio off Japan based on ROMS coupled with an NPZD biogeochemical model. The model domain encompasses both the KR and KE regions with horizontal grid spacing of 3 km, which is same with the above climatological ROMS-NPZD model. The simulation is conducted for 8 years from 2008 to 2015 to account for spatiotemporal variability of the Kuroshio path. We focus on the effects of the transient Kuroshio path on the marine surrounding and associated biological responses in the KR during the meandering.

2. Residual effects of treated effluent diversion on a seaweed farm

2.1 Numerical simulation

2.1.1 Hydrodynamic model

We develop a quadruple-nested downscaling ocean modeling (hereinafter we call the L1–L4 models) based on the Regional Oceanic Modeling System (ROMS; Shchepetkin and McWilliams, 2005; 2008), coupled with an Eulerian passive tracer model (Sec. 2.1.2) based on the one proposed in Uchiyama et al. (2014) that enables us to keep track of the effluent. The outermost boundary conditions for the ROMS models are imposed from the assimilative Japan Coastal Ocean Predictability Experiments (JCOPE2) oceanic reanalysis (Miyazawa et al., 2009) at the perimeter of the L1 model as described in Uchiyama et al. (2017a; 2017b). Then the one-way offline nesting technique successively conveys the large-scale information into the embedded child models with a gradual grid resolution refinement (e.g., Mason et al., 2010; Buijsman et al., 2012; Romero et al., 2013; Kamidaira et al., 2017). The lateral grid spacing is thus reduced from 1/12° (~10 km, JCOPE2) down to 2 km (L1), 600 m (L2), 100 m (L3), and finally 20 m (L4) as shown in **Figure 2.1**. The surface- and bottom- following, vertically stretched *s*-coordinate (Shchepetkin and McWilliams, 2005) with 32 *s*-layers is used for all the four ROMS models with the grid height refinement near the surface and bottom to resolve the boundary layers. The bathymetry for the L1 and L2 models is provided from the SRTM30_PLUS product (Rodriguez et al., 2005; Rodriguez et al., 2006; Becker et al., 2009), which covers the global ocean at 30 geographic arc seconds (~1 km), supplemented by the J-EGG500 (http://www.jodc.go.jp/data_set/jodc/jegg_intro.html) at 500-m resolution for the coastal region. For the L3 and L4 models, the bathymetries are obtained from the dataset complied by the Central Disaster Prevention Council, Japan, at horizontal resolution of 50 m.

The hourly operational atmospheric product of the Grid-Point Values–MesoScale Model (GPV-MSM; Isoguchi et al., 2010) of the Japan Meteorological Agency (JMA) provides the surface momentum flux (*viz*., wind stress). The surface heat and freshwater fluxes for L1 and L2 are provided by Coupled Ocean/Atmosphere Mesoscale Prediction System (COAMPS; Hodur, 1997) bulk formula, while the surface fluxes for L3 and L4 are from the monthly climatology of the Comprehensive Ocean-Atmosphere Data Set (COADS; Woodruff et al., 1987), principal tidal constituents from the TPXO7.0 global reanalysis (Egbert et al., 1994; Egbert and Erofeeva, 2002), and freshwater discharge of major rivers from “Annual Record of Rainfall and Discharge Database” issued by Japan River Association (http://www.japanriver.or.jp/publish/book/nenpyou_dvd.htm) and of the TSTP (City of Kobe, unpublished data). Wave-driven currents (e.g., Uchiyama et al., 2010; 2017c) are omitted as for limited fetch effects that diminish wind waves and swells

significantly. The innermost L4 model encompasses the TSTP and the whole seaweed farm area at 20-m horizontal grid spacing to sufficiently represent the complicated bathymetry and horizontal topography including coastal structures.

Because seaweed spores are vulnerable to the environmental stresses when they are sown to the farm in fall, we focus on the boreal fall condition, from September to November, when diversion occurs. In particular, the L4 model is run for about 50 days to include the whole month of October 2015, when the sewage effluent is most influential to the seaweed farm. **Table 2.1** summarizes the numerical configuration for the L3 and L4 models.

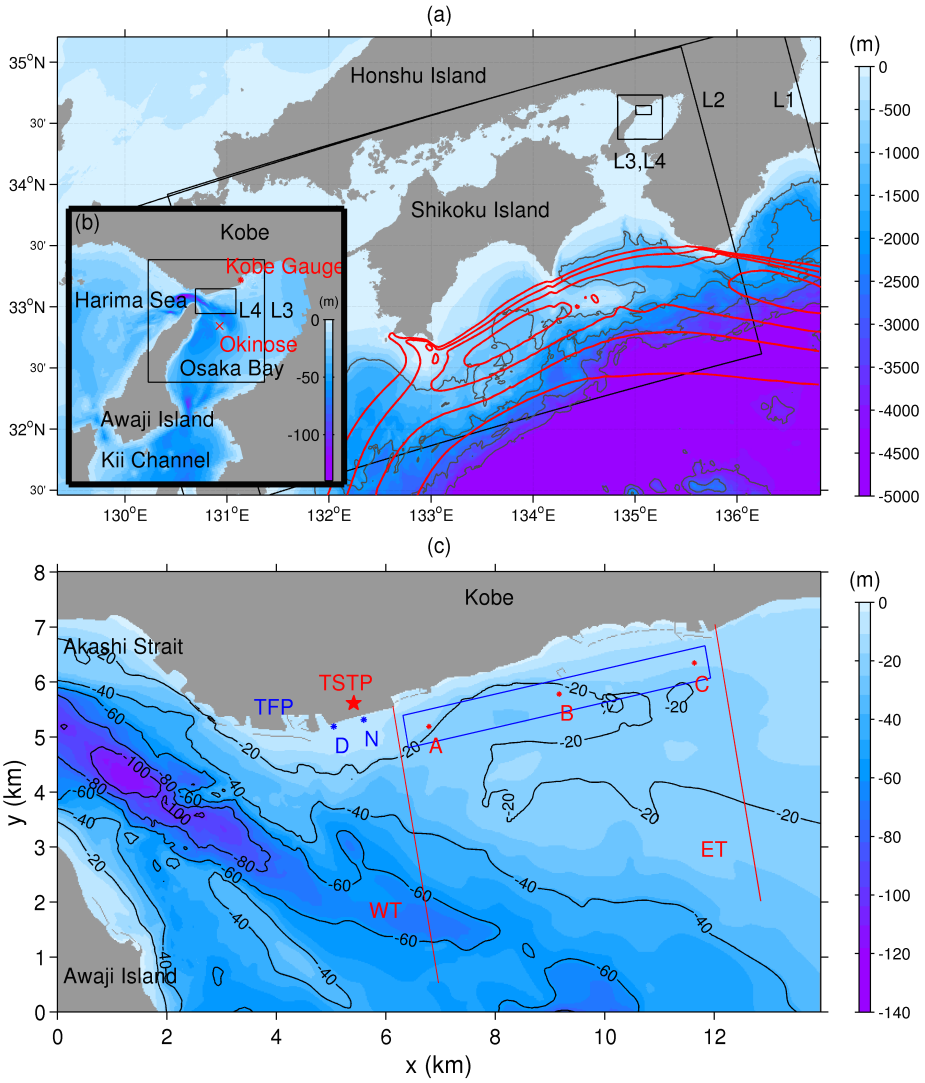

Figure 2.1. Quadruple nested ROMS model domains and bathymetry (color: m). (a) The ROMS-L1, L2, L3, and L4 domains (black boxes) embedded in the JCOPE2 domain (outside of the perimeter of the L1). The gray contours are the isobaths with intervals of 1,000 m, while the red contours indicate the approximate Kuroshio region with the surface velocity magnitude greater than 0.5 m/s at intervals of 0.25 m/s. (b) The enlarged area around Osaka Bay encompassing the L3 and L4 domains. The red dot and cross mark indicate the locations of the Kobe tidal gauge and the shallowest part of the "Okinose" shoal at the depth of 23 m. (c) The entire L4 domain with isobaths at intervals of 20 m. The blue box is the approximate extend of the seaweed farm area; TFP is the Tarumi Fishery Port area; the red star shows the location of the Tarumi Sewage Treatment Plant (TSTP); the blue dots are the two outfalls (D: diversion, N: normal); the red dots (Station A-C) are used for time series plots for **Figures 2.5, 2.6, 2.7** and **2.11**; and the red lines are two transects for the cross-sectional plots of **Figures 2.9 and 2.10**.

Table 2.1. Model configurations

Models	L1	L2
Computational period	3/1/2006-11/31/2015	9/1/2006-11/9/2015
Grid cells	320 x 320 (x 32 layers)	800 x 480 (x 32 layers)
Horizontal grid resolution	2 km	600 m
Baroclinic time step	120 s	30 s
Surface wind stress	JMA-MSM (hourly)	JMA-MSM (hourly)
Surface flux	COAMPS bulk formula	COAMPS bulk formula
Boundary/Initial condition	JCOPE2 (daily)	ROMS-L1 (daily)
T-S nudging	JCOPE2 (10-day averaged)	None
Topography	SRTM30+JEGG500	SRTM30+JEGG500

Table 2.1. Model configurations (continue)

Models	L3	L4
Computational period	9/1/2015-11/9/2015	9/21/2015-11/9/2015
Grid cells	400 x 400 (x 32 layers)	696 x 400 (x 32 layers)
Horizontal grid resolution	100 m	20 m
Baroclinic time step	8.0 s	1.0 s (diversion); 1.5 s (normal)
Surface wind stress	JMA-MSM (hourly)	JMA-MSM (hourly)
Surface flux	COADS (monthly climatology)	COADS (monthly climatology)
Boundary/Initial condition	ROMS-L2 (hourly)	ROMS-L3 (hourly)
T-S nudging	None	None
Topography	CDPC	CDPC

CDPC: Central Disaster Prevention Council, Japan (50m resolution)

2.1.2 Sewage effluent submodel

Sewage effluent from diffusers at the sea bottom immediately rises and advects as a buoyant plume. During the period between releasing from diffusers and reaching the sea surface, the effluent also mixes with ambient sea water, which is called near-field dilution. Subsequently, far-field dilution takes over due to advection and diffusion by the background currents. Because the ROMS is based on hydrostatic assumption and the L4 model still under-resolves the detailed design of diffusers, it is inappropriate to explicitly model near-field dilution that accompanies intense buoyancy-driven vertical transport. Therefore, we rely on the near-field dilution model proposed by Uchiyama et al. (2014) embedded in the 3-D transport equation of the buoyant effluent, which is explicitly applicable to far-field behavior. A submodel for buoyant sewage effluent is implemented in the L4 model as an additional 3-D advection-diffusion model for an arbitrary conservative Eulerian passive tracer, in which near-field dilution is modeled as the source term, $\mathcal{P}$:

$$\frac{\partial c}{\partial t} + \nabla \cdot \mathbf{u}c = \mathcal{D} + \mathcal{P}, \tag{2.1}$$

where c is pollutant concentration normalized by C_p, $\mathbf{u}$ is the 3-D velocity of the ambient flow, $\mathcal{D}$ is the diffusion term, ∇ is the 3-D gradient operator, and C_p [kg m^{-3}] is the input pollutant concentration at the outfall. The under-resolved non-dimensional tracer source function $\mathcal{P}$ [s^{-1}] may be represented in the following form:

$$\mathcal{P}(x, y, z; t) = P_s(t)A(x, y)H(z), \tag{2.2}$$

where P_s is the normalized tracer flux from the diffusers, and A and H are the spatial shape functions of plume above the outfall diffusers. The values of A and H are non-dimensional and close to one in the source region and zero outside it. They are also utilized to resolve the spatial distribution in the source region. The associated spatial integral relations are:

$$\iint A\, d_x d_y = A_s, \ \int H\, d_z = H_s, \tag{2.3}$$

where A_s is the horizontal area, H_s is the vertical size, $V_s = A_s H_s$ is the volume of the prescribed plume. Hence, $P_s(t) = Q_p(t)/V_s$, where $Q_p(t)$ [m^3 s^{-1}] is the volume flux. Since the variable c is a non-dimensional concentration, we can retrieve any arbitrary conservative concentration such as colored dissolved organic matter (CDOM), nitrate, and ammonium by multiplying a factor C_p, which corresponds to the mean concentration at the point source. Note that a similar source term is added to the 3-D mass, momentum, salinity, and temperature conservation equations to account for near-field dilution effects.

The shape functions A and H are described also according to Uchiyama *et al*. (2014). We assume that the peak of released sewage flux occurs at sea surface with downward exponential decay following a Gaussian distribution:

$$H(z) = \exp\left[-\frac{(z-z_s)^2}{d_s^2}\right], \tag{2.4}$$

where z_s is the plume center height, and d_s is the vertical scale of the plume. For our outfall design, z_s is set to be 0 m for the surface confined shape with d_s of 7 m, the local mean depth. The sewage effluent is applied at the locations of the two outfalls (normal and diversion) as a bottom-released freshwater plume at a constant volume rate of 1.80×10^5 m^3 d^{-1}. The discharged no-dimensional passive tracer is set to always be unity (one) with temperature of the ambient seawater and zero salinity. The diversion and normal outfalls are represented by two and four grid points, respectively (*viz*., a footprint of 20 m × 40 m for diversion and 20 m × 80 m for normal). Their centers are located 80 m and 40 m offshore from the sea wall of the TSTP, which are approximately correspond to the pipe lengths of the central (normal) and western (diversion) outfalls.

2.2 Validation

2.2.1 Temperature and salinity

The newly developed L3 and L4 models are validated with observed data, while the parent L1 and L2 models were demonstrated to agree well with *in situ* measurement of temperature, salinity, and tides for the 9-year period from 2006–2015 in Kosako et al. (2016). **Figure 2.2** shows scatter plots of the modeled and measured sea-surface temperature (SST) and salinity (SSS). The observed data are based on repeated CTD measurement from vessels, and are available as a part of "The Comprehensive Water Quality Survey in the Seto Inland Sea" collected and maintained by the Ministry of Land Infrastructure and Transport, Japan (http://www.pa.cgr.mlit.go.jp/chiki/suishitu/). The areas outside of the L3 and L4 domains are supplemented by the L2 result. The model shows an outstanding reproducibility of SST (**Figures 2.2a** and **3**), whereas it is moderate for SSS with a correlation coefficient of 0.379 (**Figure 2.2b**). Such an overall reasonable reproducibility is inherited from their parent models (Kosako et al., 2016). The modeled SSS is overestimated because our model accounts merely for the monthly climatology of the major rivers (Section 2.1.1) that leads to much less freshwater input to the SIS. Nevertheless, the estimated average density error of the surface layer caused by the erroneous freshwater input is only 0.14%, leading to subtle effects on the near-field submodel (Section 2.1.2) and the result presented below. The inclusion of temporally varying synoptic freshwater discharge from the rivers, hundreds of unnamed small streams, and groundwater seepage ubiquitous along the shoreline, should improve the salinity reproducibility. Apparently our implementation is suboptimal, yet detailed freshwater data has not been publically available for the SIS thus far. Kurosawa et al. (2017) supported this speculation from the same L2 SIS model with data assimilation and indicated that precipitation has prominent influence on the river discharge in September and October, leading to the overestimation of the simulated SSS. Our choice is considered as the least bad option, which must be reconciled in future upon data availability.

It is worth mentioning that a more elaborate near-field mixing model could be alternatively used for the source term $\mathcal{P}$ in order to reflect realistic behavior of a transient buoyancy plume at the outfall pipes. A possible direction is to employ a sophisticated 3-D near-field model such as the one based on a non-hydrostatic LES model (Nakayama and Nizamani, 2016). Such an implementation into the present system is viable, and should be conducted in future work.

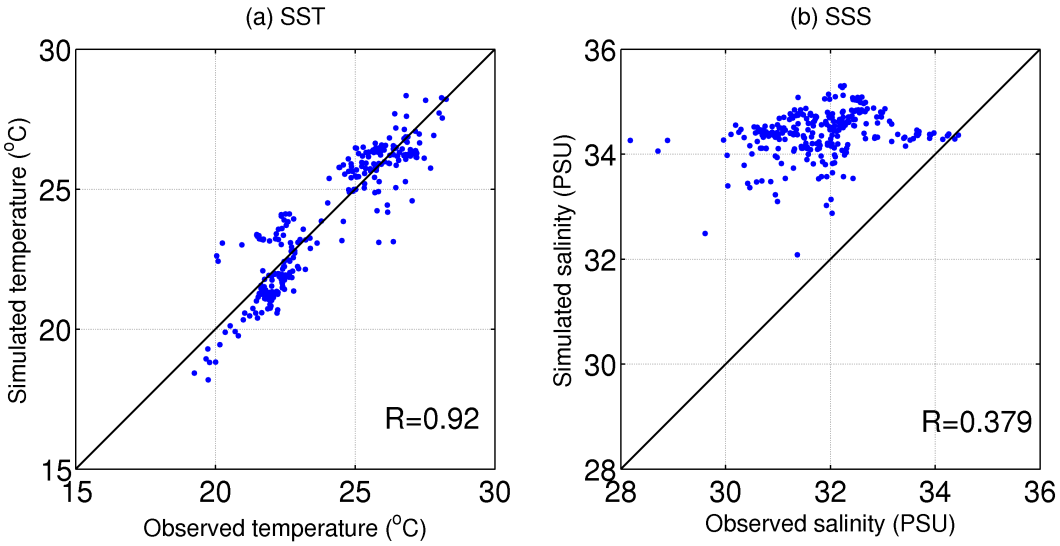

Figure 2.2. Scatter plots of (a) SST (temperature) and (b) SSS (salinity) at surface from the discrete ship observation versus the corresponding model results.

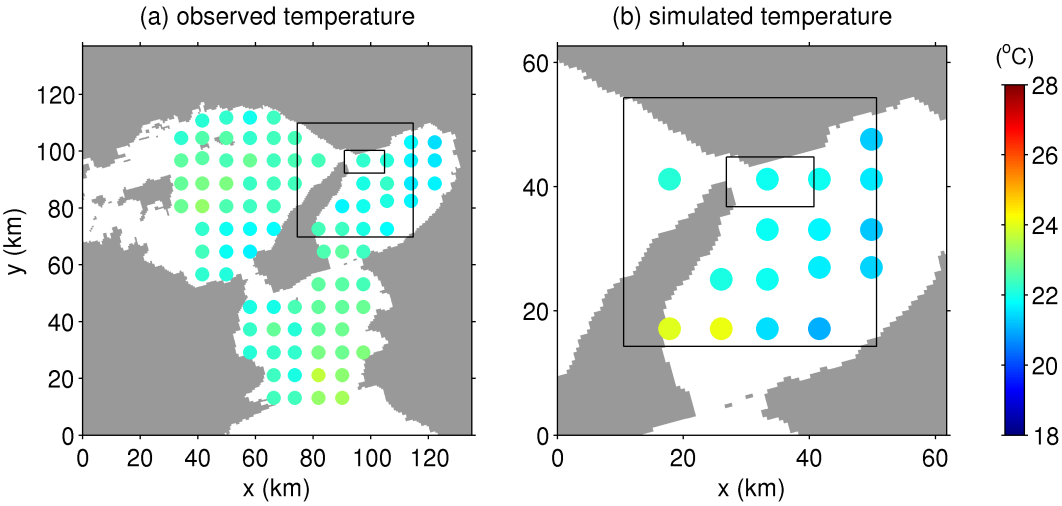

Figure 2.3. Spatial maps of (a) the observed SST shown in **Figure 2** and (b) the corresponding computed SST from the ROMS-L4. The black boxes are the L3 and L4 domains. Note that the observations were conducted from vessels for 7 days in October 2015.

2.2.2 Tidal harmonic analysis

We next verify the time-varying surface elevations mainly due to tides at the Kobe tide gauge station (**Figure 2.1b**) operated by the JMA and maintained by Japan Oceanographic Data Center (JODC; http://jdoss1.jodc.go.jp/vpage/tide_j.html). A tidal harmonic analysis is conducted with the modeled and measured hourly surface elevation as summarized in **Table 2.2** for four selected principal tidal constituents (M_2, S_2, K_1, and O_1). The tidal amplitudes and phases are reasonably well reproduced by the model with correlation coefficients of 0.9785 and 0.9996 respectively. Slightly less agreement is obtained in the two semi-diurnal constituents, whereas these biases are already contained in the TPXO7.0 that provides the lateral boundary conditions for the barotropic tides along the L2 perimeter (Sec. 2.1). Nevertheless, the estimated average density error of the surface layer caused by the erroneous freshwater input is only 0.14%, leading to subtle effects on the near-field submodel (Section 2.1.2) and the result presented below. In general, the high-resolution L3 and L4 models exhibit a reasonable reproducibility in the hydrodynamics around Osaka Bay, although there certainly is a room for improvement. We leave these issues for future works.

Table 2. Result of the tidal harmonic analysis of the modeled (ROMS-L3) and observed (JMA) hourly surface elevation at the Kobe tidal gauge.

	Amplitude (m)			Phase (°)		
	OBS	MDL	DIF	OBS	MDL	DIF
M_2	0.3112	0.4216	-0.1104	307.8853	300.0558	7.8295
S_2	0.1846	0.2647	-0.0801	310.6101	304.0042	6.6059
K_1	0.1915	0.2345	-0.0430	53.9154	61.8425	-7.9271
O_1	0.1405	0.2116	-0.0711	47.0540	45.0413	2.0127

OBS: JMA observation data; MDL: ROMS-L3 model data;
DIF: Difference (observation - model)

2.2.3 Surface wastewater transport

Bulk behavior of the modeled sewage effluent is compared with the measured freshwater plume from the western diversion outfall of the TSTP (**Figure 2.1c**). We chose to qualitatively compare with the *in situ* measurement described in BN07, where an empirical, *ad hoc* filter was used to the T-S diagram to separate out the sewage effluent from the ambient seawater and riverine freshwater. Their vessel-based acoustic Doppler current profiler (ADCP) and tow-body CTD measurement had been repeatedly conducted on December 1, 2005, ~3 days before a spring tide, for almost one M_2 tidal cycle (~10 hours) in a narrow 1 km × 1 km region off the TSTP diversion outfall. Nevertheless, the signals of the freshwater effluent represented by the filtered salinity fraction were detected mostly in this 1 km × 1 km box and barely extended further in the offshore and alongshore directions. The most striking finding in BN07 (see their **Figure 2.4**) is the asymmetric, alongshore confined effluent transport due to prevailing alongshore currents constrained by topographies. During phases from slack to flood tides, westward alongshore currents developed to induce westward effluent transport towards the Akashi Strait, while the breakwater of the adjacent fishing port located in the west of the TSTP notably affected both of them to generate southward offshore current and transport. As a result, the effluent mostly stayed within ~400 m from the outfall. Subsequently, an ebbing phase manifested to promote shore-confined eastward currents and associated shore-trapped eastward effluent transport, followed by another flow inversion with more prominent flood tide than the previous flooding. Interestingly, the shore-trapped effluent in the east of the outfall kept staying there for several hours even with the reverted westward offshore currents for the flooding tide. BN07 speculated that a nearshore clockwise recirculation with the cross-shore extent of ~200 m was formed to entrain the effluent within the overall westward current. Honda et al. (2007) extended the Eulerian analysis of BN07 by using Lagrangian surface drifters equipped with conductivity-temperature sensors, reassuring the alongshore asymmetric effluent dilution, where relatively stagnated, less diffusive eastward transport took place during an ebb, while more diffusive westward transport was provoked in conjunction with remote influences from intense offshore tidal currents generated in the Akashi Strait. Such small-scale, coastally trapped dispersal of the buoyant effluent is solid evidence why we need high-resolution modeling with larger scale ambient currents.

Figure 2.4 shows sea surface elevation on the top panel, and sequential five pairs of snapshots of relative vorticity (left panels) and corresponding normalized passive tracer concentration c in the enlarged area near the TSTP (right panels) at the surface with subsampled surface velocity vectors for the western diversion case on October 1st, 2015. Because the prevailing westward currents are formed during a flood tide (**Figure 2.4b**, **c**) and reach maximum at the highest slack tide (**Figure 2.4d**, **e**), the surfaced sewage released from the bottom-mounted diffusers is also transported westward at the surface and confined near the shore (**Figure 2.4c**, **e**). Subsequently, the currents weaken and

change direction during an ebb, resulting to eastward sewage transport (**Figure 2.4f, g**). The wastewater distribution is largely affected by the fishing port at just west of the TSTP during this period, in particular by its detached breakwater located ~150 m offshore to entrain tracer notably in the port (**Figure 2.4g**). Then a flow reversal occurs at a lowest slack tide (**Figure 2.4h, i**) with retaining the eastward currents formed around the offshore deep channel of the strait, while westward flow is predominant in the nearshore shallow area. Such a cross-shore inversion of the alongshore flow direction results in quite strong vorticity in the channel and near the coastline bend next to the TSTP (**Figure 2.4h**). A counter-clockwise circulation also forms around the eastern tip of the breakwater to transport the sewage offshore (**Figure 2.4i**). As a consequence, the tracer is widely distributed in the cross-shore direction at the low tide. The sewage is transported westward again during the flood due to the counter-clockwise lateral circulation formed off TSTP that promotes nearshore westward flow (**Figure 2.4j, k**). In summary, the model successfully reproduces tidally-driven, asymmetric, alongshore dominated, shore trapped effluent dispersal patterns consistent with those observed in BN07, yet there are several minor discrepancies attributed mainly to the different periods.

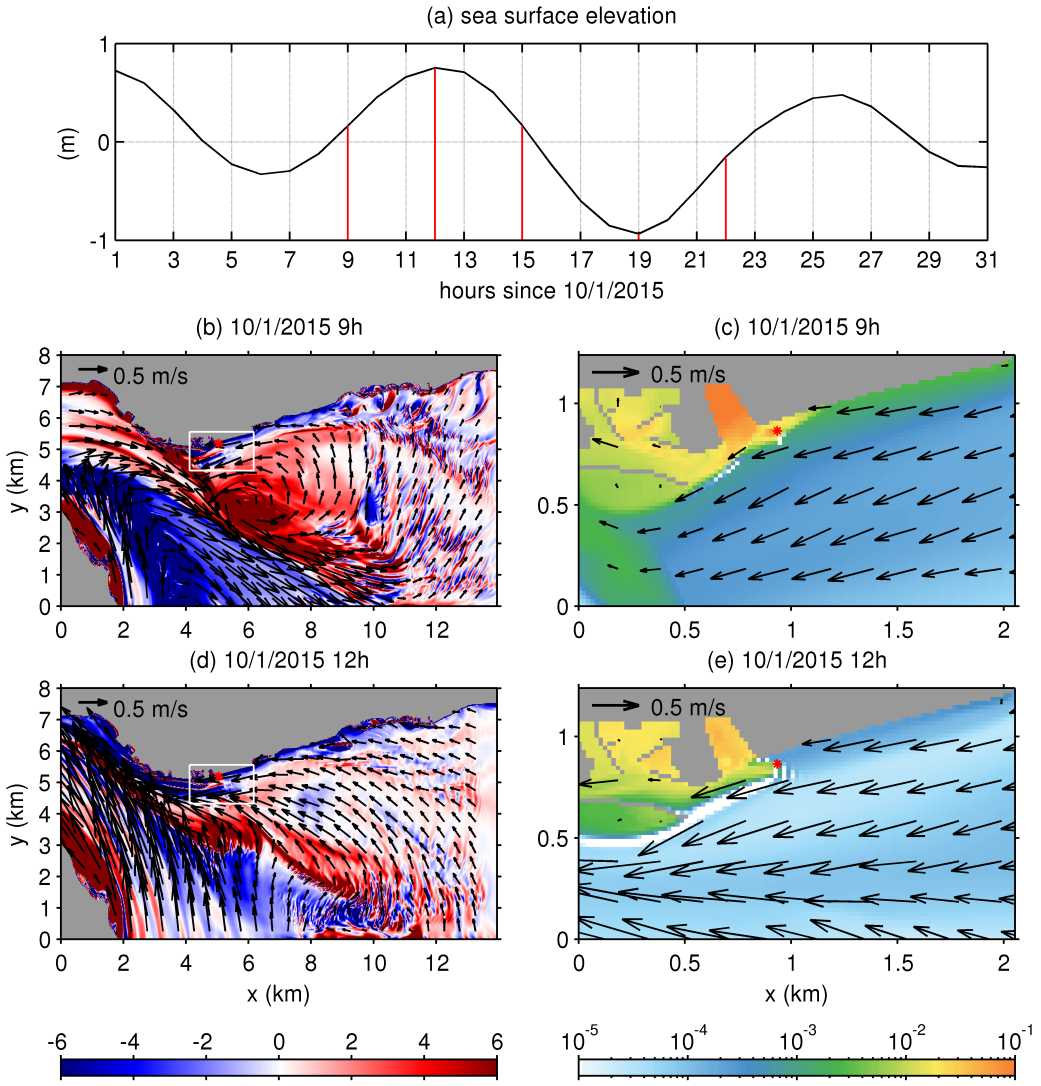

Figure 2.4. (a) Time series plot of sea surface elevation at Tarumi Area, which is located in 1 km offshore, since 1:00 UTC, October 1st, 2015. The five red vertical lines indicate the selected survey rounds at 9th, 12th, 15th, 19th and 22th hours on October 1st, 2015, as shown in panels (b) – (k). Snapshots (hourly-averaged data) of vertical component of relative vorticity (s^{-1}) at surface normalized by the local Coriolis parameter (color) are on the left at each survey round with the indicated time. Depicted in the right panels are the corresponding normalized passive tracer concentrations, *c* (color), in the enlarged area near the TSTP shown by the white boxes in the left panels. The red dots represent the location of the western diversion outfall. The vectors are superposed to show subsampled instantaneous surface velocity. The arrows on the top-left corner of each plot indicate the velocity scale of 0.5 m/s.

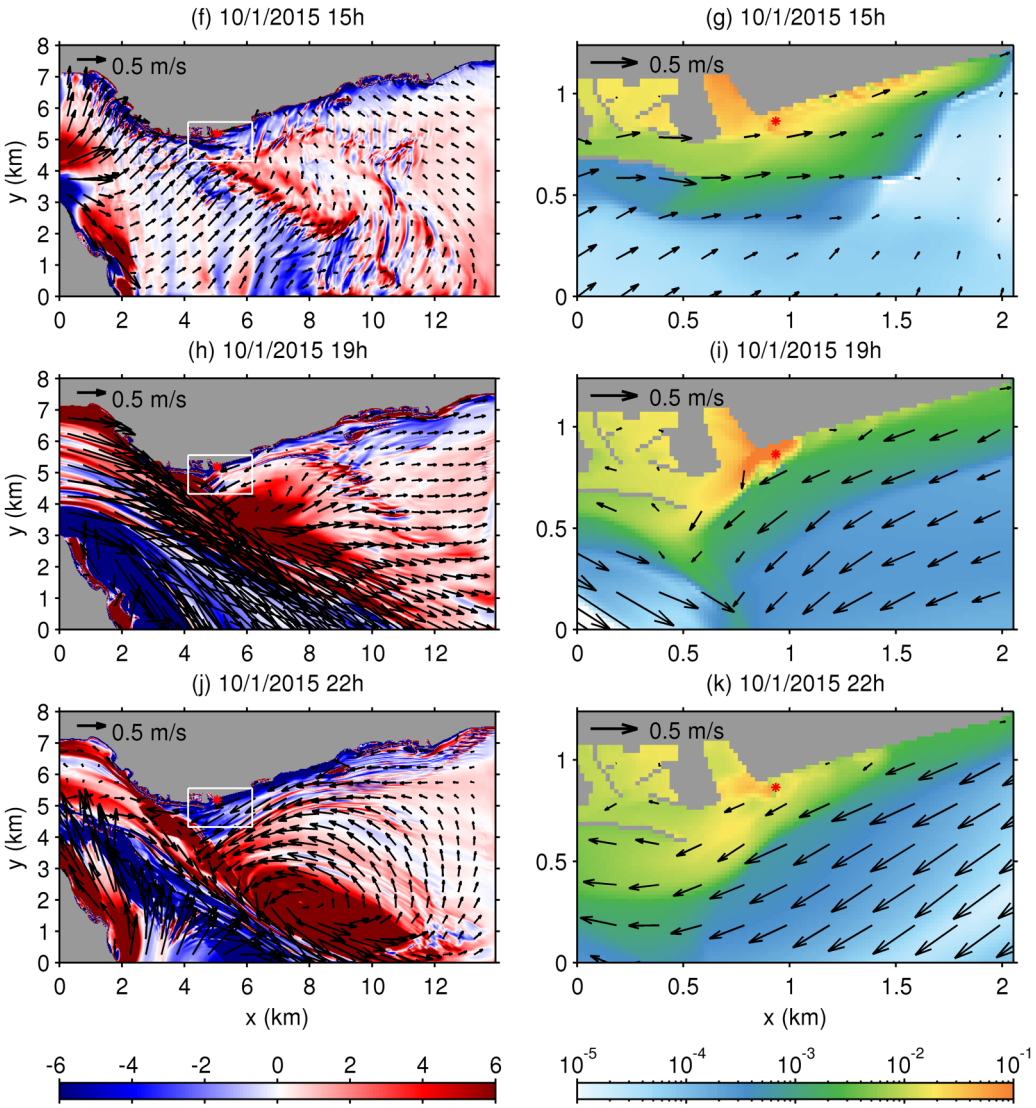

Figure 2.4. Continued.

2.3 Dynamics

2.3.1 Surface currents

Spatiotemporally varying currents driven mainly by tides near narrow straits have been of great interest (e.g., Imasato, 1983; Imasato et al., 1994; Li et al., 2015, among many others). Our study area is in such a set-up, where the narrow Akashi Strait repeatedly generates quite intense tidally driven currents that affect both transient and residual dynamics and the resultant effluent dispersal near the TSTP. **Figure 2.5** shows the surface residual velocity vectors as the monthly-averaged velocity with colors illustrating their magnitude, and a time-series plot of hourly surface velocity at Sta. A (**Figure 2.1c**), for the diversion case. Strong tidal currents are repeatedly formed to intrude southeastward (northwestward) into Osaka Bay (Harima Sea) through the narrow Akashi Strait flanked by Honshu and Awaji islands (**Figure 2.1b**). Both the zonal (alongshore) and meridional (cross-shore) surface velocities fluctuate considerably at the semidiurnal period with a peak speed of 0.6 m s^{-1} and 0.2 m s^{-1}, respectively. Such a velocity variation is consistent with the ADCP measurement in the SIS (e.g., Kobayashi et al., 2009).

The residual currents are complicatedly distributed (**Figure 2.5a**), primarily consisting of 1) the northwestward coastal current along the northeastern shore of Awaji Island, 2) the clockwise circulation off the Awaji Island and the TSTP, which is often referred to as the "Okinose Circulation" (e.g., Nakatsuji et al., 1994; Mishima et al., 1999), while only the northern part of that is depicted here, and 3) the counterclockwise circulation off the TSTP, consistent with the model result in Imasato (1983). The velocity magnitudes are largest in the three predominant currents. The coastal current along Awaji Island veers clockwise to point northeastward at $y \approx 5$ km, then further turns clockwise to form the southeastward currents that detaches from the Honshu Island near the bend of the coastline at $x \approx 3$ km next to the TSTP, and eventually merges with the Okinose Circulation. The counterclockwise circulation near the TSTP accompanies the westward nearshore current, which veers left to the offshore, and then coalesces with the Okinose Circulation off the TSTP. Therefore, the surface currents mostly converge off the coastline bend near the TSTP. As shown in **Figure 2.4**, the effluent from the TSTP drifts westward near the shore after the release, and turns offshore. Subsequently it is entrained in the Okinose Circulation, and then transported southeastward toward Osaka Bay. Such a transport pattern is readily anticipated to reduce the direct impact of the effluent to the seaweed farm located in the east of the TSTP.

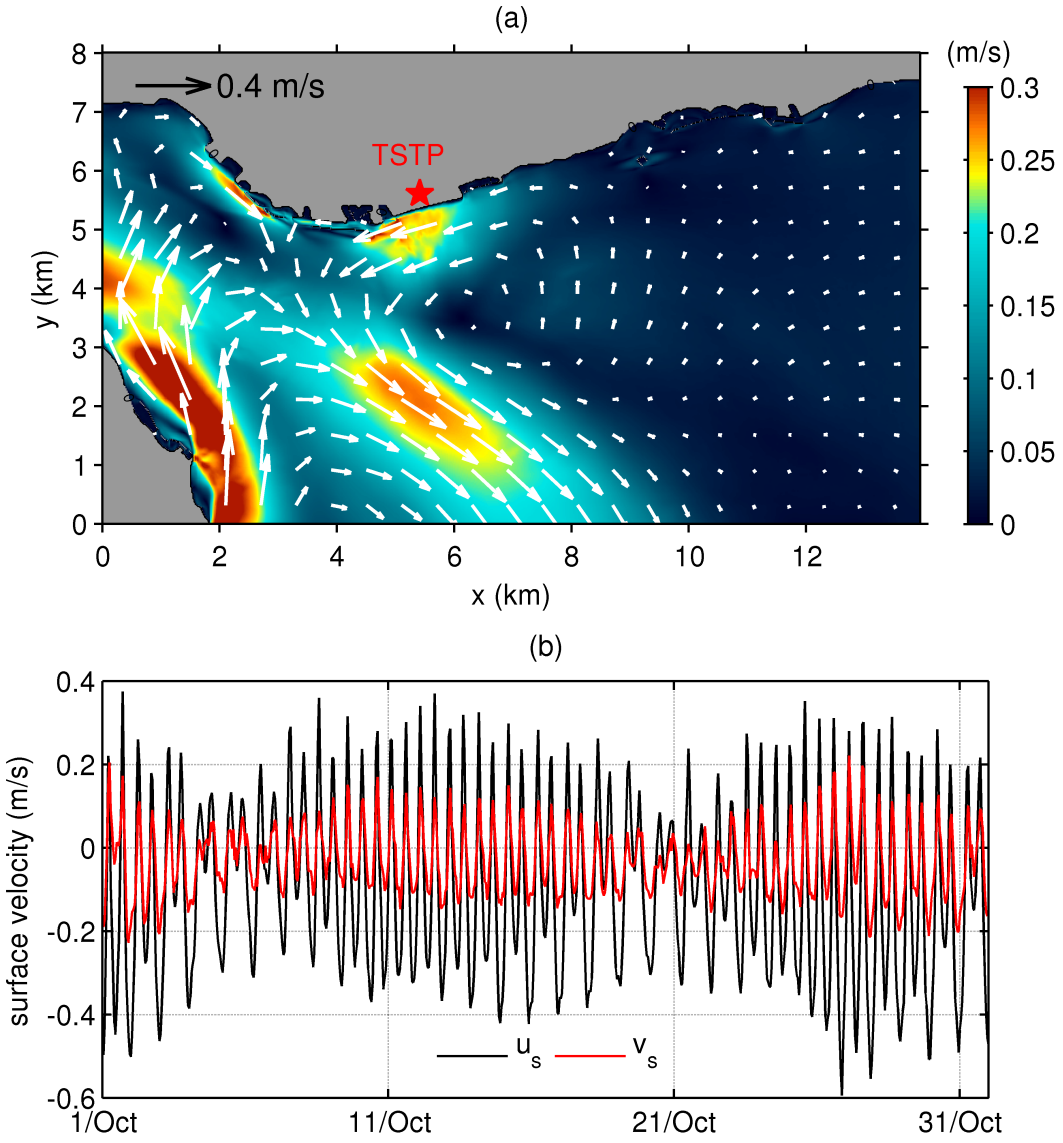

Figure 2.5. (a) Monthly mean surface velocity vectors (white arrows) on their own magnitude (color). (b) Temporal variability of the eastward (u_s, black) and northward (v_s, red) surface currents at Stn. A (**Figure 2.1c**) for the diversion case.

2.3.2 Underlying mechanism

We next carry out a spectral analysis to examine possible driving mechanisms of the flow field around the seaweed farm. **Figure 2.6** compares the frequency spectra of surface currents $\mathbf{u}_s = (u_s, v_s)$, wind stress at 10 m above the sea surface $\tau_s = (\tau_u, \tau_v)$, and surface elevation ζ at Stn. A (**Figure 2.1c**) for October 2015. u_s and τ_u are the meridional (eastward) component, while v_s and τ_v are the zonal (northward) component. Two distinctive peaks commonly appear in both the components at the diurnal and semidiurnal frequencies in the surface velocity and ζ with moderate semidiurnal predominance. The wind stress spectra are "red" with low-frequency prevalence and no notable peaks, whereas the diurnal variability manifests modestly, presumably reflecting land-sea breeze cycles

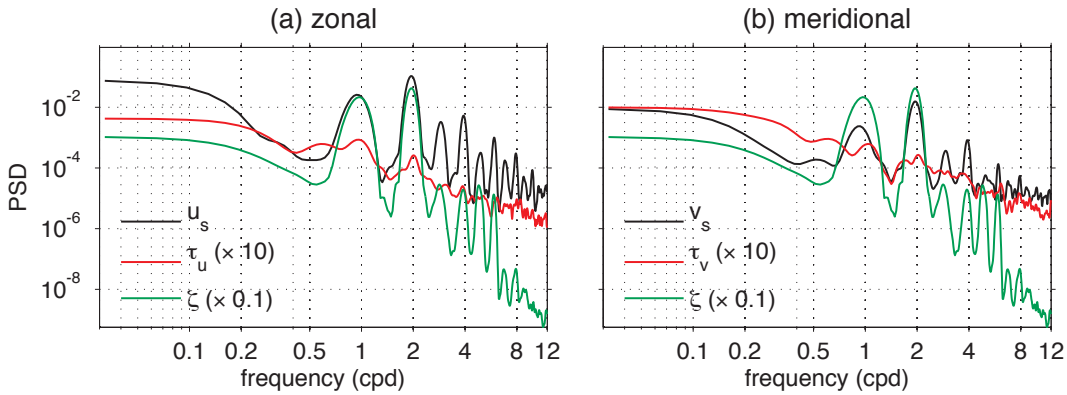

Figure 2.6. Power spectral densities (PSDs) of (a) the eastward surface velocity, u_s, eastward wind stress, τ_u, and sea surface elevation, ζ, and the northward surface velocity, v_s, northward wind stress, τ_v, and ζ at Stn. A (**Figure 2.1c**). The units of PSDs for velocity, wind stress, and elevation are (m^2/s^2)/cpd, (N^2/m^4)/cpd and (m^2)/cpd, respectively.

Such similarity in the spectral shapes is further investigated with spectral coherences among the variables (**Figure 7**) at the three selected locations, Stn. A – C in the seaweed farm (**Figure 1c**). The coherences of the alongshore velocity u_s against τ_u and ζ (left column) are distributed similarly at all the three stations. The coherences are commonly high at the diurnal and semidiurnal frequencies. However, the coherences between u_s and ζ are much higher (> 0.9) than those between u_s and τ_u (< 0.5), demonstrating that tidal currents dominate over wind stresses to generate the alongshore surface currents in the farm and thus the resultant effluent dispersal. In the higher subtidal frequency band for about 0.2 – 0.5 cpd, u_s is influenced by both tidal current and wind stress at Stn. A (**Figure 7a**). In contrast, the coherence against τ_u decreases gradually at Stns. B and C as going away from the TSTP (**Figure 7c**, **e**), exhibiting wind becomes less influential. In the much lower frequency band than 0.2 cpd, the lower subtidal ζ and low frequency wind jointly affect the surface current at Stn. C with coherence by ~0.4, which in turn decreases at Stns. A and B. Nevertheless, the coherence of cross-shore velocity v_s (right column) substantially differs from that of u_s. Although the coherence between v_s and ζ is high at the diurnal and semidiurnal frequencies near the TSTP (*viz*., Stn. A), it rapidly decreases as leaving from the TSTP. The semidiurnal and diurnal coherence against wind stress is always low. In contrast, the subtidal coherence against ζ and τ_v for the band lower than 0.5 cpd, particularly for 0.2 – 0.5 cpd, is much larger than that for u_s.

These results clearly indicate that the tidal currents prevail near the TSTP to primarily provoke the alongshore currents that are rectified by the coastline and topography, whereas such topographic constraint is relaxed at Stn. A, where tidal ellipse is more circular (not shown). At locations distant from the Akashi Strait on the shallow shelf (Stns. B and C), tidal currents are intensely constrained by topography, and the cross-shore currents vary mostly with low-frequency wind and . The low-frequency variability is obviously attributed to subinertial motions forced by low-frequency wind variability. Eddies may play another important role. The seaweed farm is located under unique hydrodynamic condition on a shallow shelf in the north of the deep channel where the Okinose Circulation develops (**Figure 5a**). The western part of the farm (*viz*., Stn. A) is intensively controlled by tides as well as subtidal cross-shore currents. The central (Stn. B) and eastern (Stn. C) parts of the farm are in a mixed configuration, in which the alongshore currents are tidally driven, while the cross-shore currents are influenced notably by low-frequency wind, not by tides. In the subtidal frequency band lower than 0.2 cpd, the subtidal solely contributes to the cross-shore subtidal currents, reflecting much larger-scale flows including the quasi-persistent eastward SIS through flow maintained by the transient Kuroshio (*e.g*., Kosako et al., 2016).

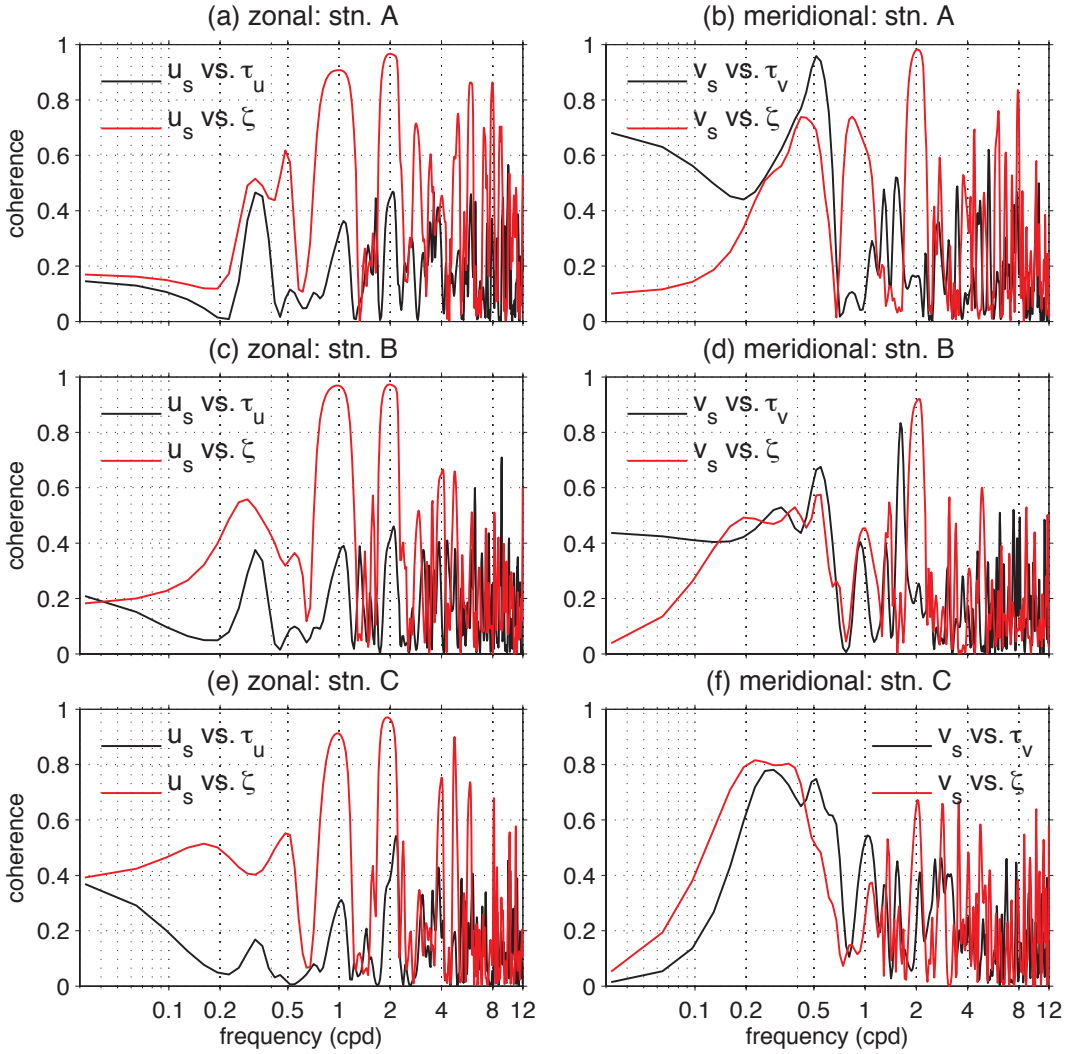

Figure 2.7. Left: spectral coherences of u_s versus τ_u (black) and ζ (red), and right: spectral coherences of v_s versus τ_v (black) and ζ (red) at Stn. A (panels a & b), B (c & d) and C (e & f). The locations of the three stations are shown in **Figure 2.1c**.

2.4 Impacts of diversion

2.4.1 Time-averaged horizontal structure

Because seaweed growth is crucial to adequate light to drive photosynthesis (Abowei et al., 2013), they are inhabitable in the near-surface euphotic layer. Therefore, surface effluent transport and its accumulation are the most essential factors to be assessed. **Figure 8** shows the monthly averaged SSS (contours) and passive tracer concentration c normalized by the source concentration C_p (Section 2.2) at surface representing effluent far-field dilution (color), averaged for the month of October 2015. The result for the case with the diversion discharge from the western outfall is depicted on the top, while the differences (diversion case – normal case) are on the bottom. A weak, lateral salinity gradient is formed with lower SSS in the northeast (**Figure 2.8a**), owing primarily to riverine freshwater discharge from the major rivers in the inner Osaka Bay in the further east, as well as influences from the buoyant plume of the freshwater effluent. The difference of SSS between the two cases is non-trivial with a factor of several percent relative to the spatial difference of SSS (**Figure 2.8b**). The western diversion results in overall salinity increase near the coast including the eastern shore close to the seaweed farm, except for the area just off the TSTP, where freshening occurs about 3 km from the shore. A similar pattern is observed in the temperature field, although it is subtle with SST differences no more than 0.01°C (not shown). Hence, the effect of the locations of the outfall on buoyancy-driven dynamics is not significant.

The surface effluent dilution c is distributed similarly to SSS for the diversion case and confined mostly near the shore on the both zonal sides relative to the TSTP with a pronounced eastward bias in particular around the TSTP (**Figure 2.8a**). On the eastern shallow area, c is widely extended to the offshore with notable cross-shore dilution for depths less than ~40 m (see **Figure 2.1c**). This pattern is consistent with that of the surface residual currents, where the strong currents are formed mostly in the deeper channel constrained by topography. The diversion successfully reduces the nearshore c (cold color) significantly, particularly near the shore inclusive of the majority of the seaweed farm area depicted by the white box (**Figure 2.8b**). Similarly to SSS, the diversion increases c just offshore the TSTP (warm color) with offshore extent of ~3 km. Such spatial differences in the effluent concentration and salinity are considered to be attributed to the counter-clockwise circulation formed off the TSTP as a part of the Okinose Circulation, where the westward currents developed near the eastern shore transport the released tracers westward and then seaward off the TSTP, and entrain in the circulation to promote eastward transport in the offshore area.

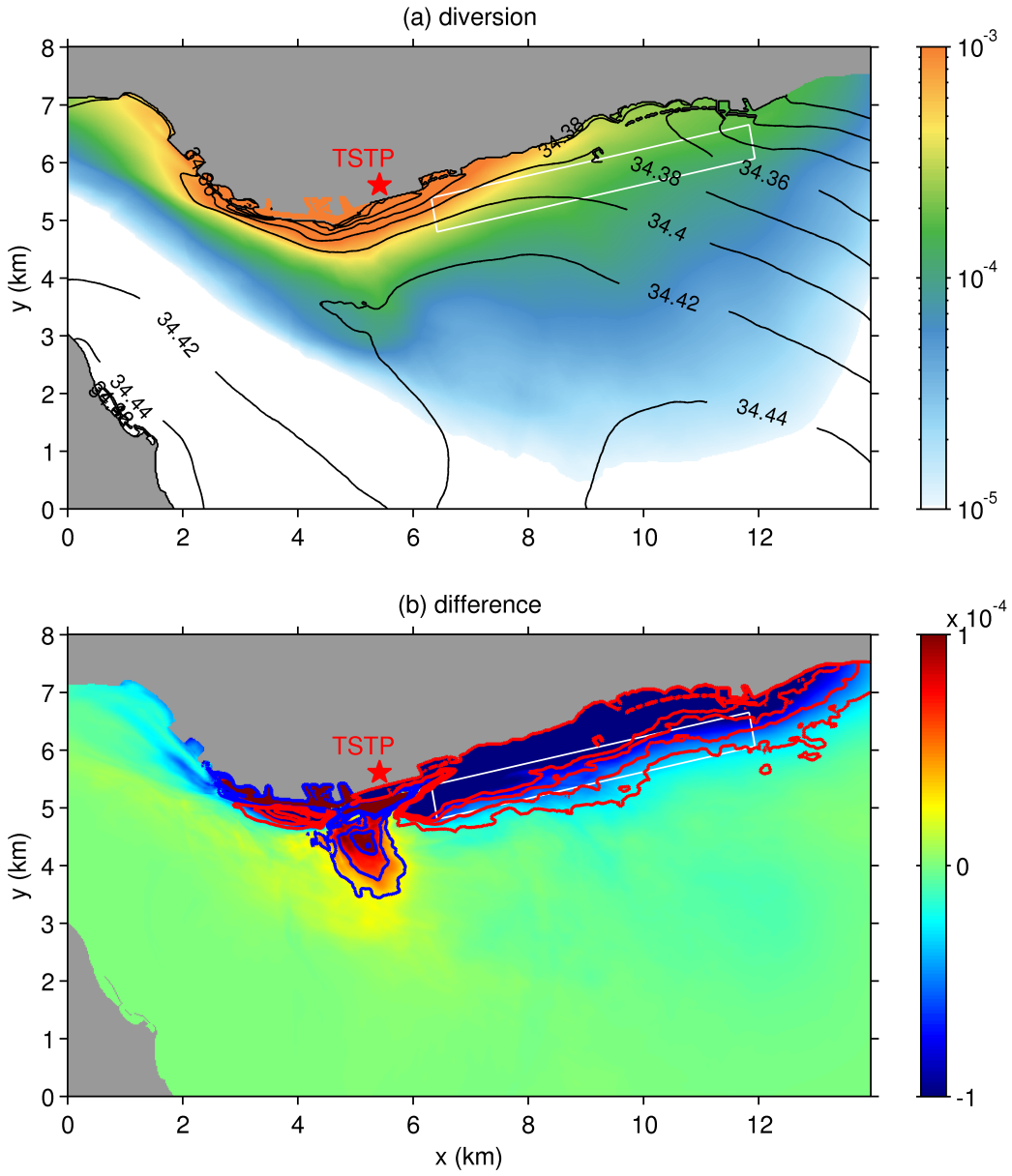

Figure 2.8. (a) Monthly mean passive tracer concentration, *c* (color, non-dimension) at surface for the diversion case. The black contours and labels denote sea surface salinity (SSS; intervals: 0.02 psu). (b) The difference of *c* (color, non-dimension) and SSS (contours) between two cases (diversion - normal). The red and blue contours are positive and negative value (intervals: 0.001 psu).

2.4.2 Time-averaged vertical structure

While our primary interests are in the near-surface processes, vertical structures of the time-averaged c and salinity (S) are briefly discussed. We introduce two nearshore transects normal to the shore defined approximately at the western and eastern boundaries of the seaweed farm area indicated by the red lines in **Figure 2.1c**. **Figure 2.9** shows the cross-sectional plots of monthly averaged c (color) and S (contours) along the western transect for October of 2015 for the diversion case in **Figure 2.9a**, the difference between two cases (diversion – normal) in **Figure 2.9b**, denoted by ΔS and Δc, and the corresponding enlarged plots for the nearshore area in **Figure 2.9c** and **d**. The red contours in **Figure 2.9b** and **d** represent the isohalines for $\Delta S = 0$ psu, while the solid and dotted white contours are positive and negative values (intervals: 0.005 psu). The spatial distributions of c and S are largely consistent each other (**Figure 2.9a**), exhibiting that the buoyant effluent plume from the outfall transports increased c and decreased S simultaneously. The effluent plume affects most considerably in the nearshore area, where S is lowered near the surface to form buoyantly stable stratification. As a consequence, c is consistently distributed mostly in the area where freshening takes place. The diversion alters c and S only in the limited area by ~1 km from the shore with somewhat different spatial patterns (**Figure 2.9b** and **d**). With the diversion, S is increased near the surface due to the reduced freshwater effects from the TSTP (solid white contours), while decreased in the lower layer near the shore (dotted white contours). Likewise, the diversion generally decreases (increases) c where S is increased (decreased). In particular, c is always diminished in the near-surface layer shallower than ~3 m depth with the diversion outfall, which reduces the influence of the effluent from the TSTP on the seaweed farm. However, the diversion lowers c in the shallow area no farther than ~200 m from the shore, where S is enhanced (**Figure 2.9d**). This minor difference in the cross-sectional spatial patterns of the deviations in c and S due to the diversion is most likely caused by the river-originated fresher S source mainly from the east, that promotes more intense recurring westward effluent transport formed in front of the TSTP extending to the northwestern corner of the farm than that of c (**Figure 2.8b**). On the other hand, the diversion results in increase of the near-surface S to promote a vertical overturning circulation cell that acts to entrain c in the middle of the cell and forms the subsurface positive Δc maximum.

As shown in **Figure 2.10**, the cross-sectional structures of c and S along the eastern transect (**Figure 2.1c**) and their differences associated with the diversion are much simpler with smaller values than those along the western transect. In the diversion case (**Figure 2.10a**) the freshening due to the riverine water from the east is notable within ~2 km from the shore, as shown in SSS in **Figure 2.8a**. The offshore extent of the effluent c is approximately in the same range as that for S. Increase of S and decrease of c due to the diversion are more confined to the shore, by ~1 km to the sea, whereas the former is negligibly small. The surface-trapped diversion effects in **Figure 2.10b** are not as evident

as that observed along the western transect **(Figure 2.9b)**, supporting that the TSTP-originated buoyant plume is much less influential near the surface along the eastern transect. The above results suggest that buoyancy effects due to freshwater effluent moderately alter the nearshore 3-D flow and the associated *c* distribution, particularly near the TSTP.

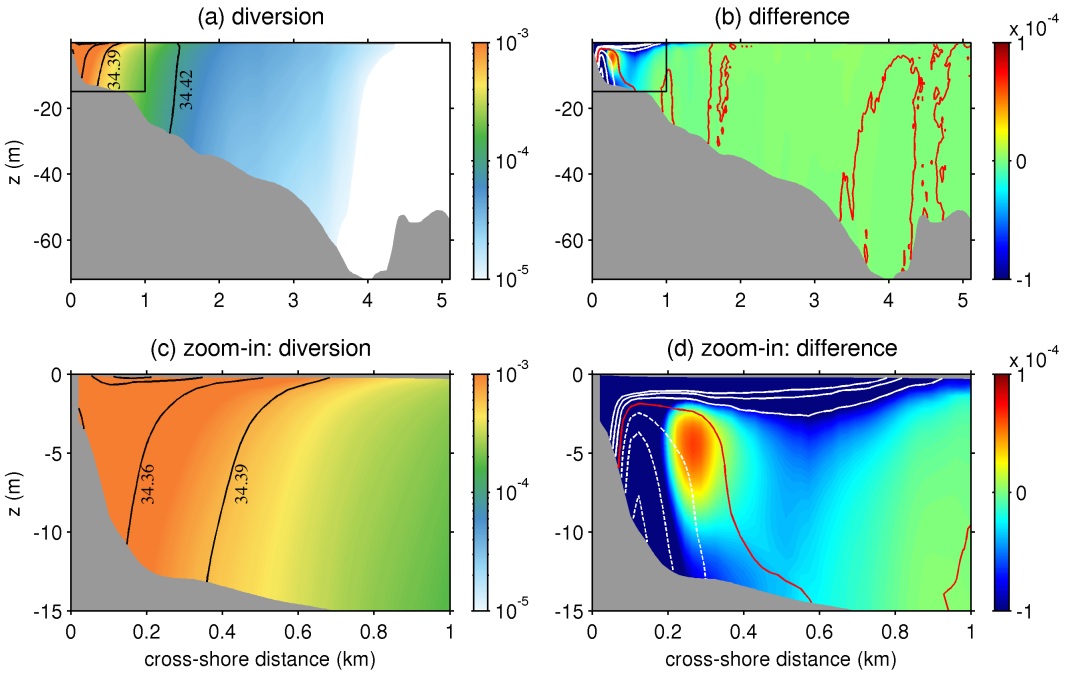

Figure 2.9. (a) Cross-sectional plot of monthly mean tracer concentration, *c* (color, non-dimension) at the western transect (WT in **Figure 2.1c**) for the diversion case. The black contours and labels denote the salinity (intervals: 0.03 psu). (b) Cross-sectional plot of the difference of *c* (color, non-dimension) and salinity (contours) between two cases: (diversion - normal). The red contours represent zero, while the solid and dotted white contours are positive and negative values (intervals: 0.005 psu). (c) and (d) show the enlarged nearshore areas depicted by the thin black boxes around the upper-left corners of (a) and (b), respectively.

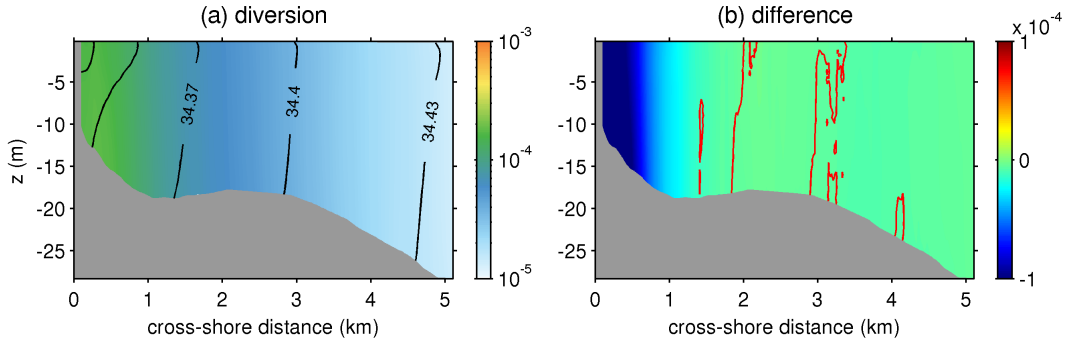

Figure 2.10. Same as **Figure 2.9a** and **b**, but for the eastern transect (ET in **Figure 2.1c**).

2.4.3 Spatiotemporal variability

Effects of the sewage effluent from the two outfalls on the seaweed farm are examined with time-series plots of the surface *c* (**Figure 2.11**) at the three selected locations in the farm defined in **Figure 2.1c**. The effluent concentration *c* gradually decreases from Sta. A to C with increased distances from the TSTP. Because the differences of the surface *c* at the three stations depicted by green curves have apparent negative biases, the diversion outfall is ensured to work adequately in the reduction of *c* in the farm. Temporal fluctuations of *c* for both the normal and diversion cases occur differently at the three stations. Although high frequency tidal variability is clearly observed at the western-most station A located ~1 km from the TSTP, much lower frequency subtidal fluctuations are superposed on the tidal signals at the central station B. Furthermore, at the eastern-most station C, the subtidal components are predominant over the tidal components. Overall, the differences of *c* at the three stations fluctuate similarly to *c* with significant reduction due to the diversion. At Sta. A, the reduction takes place intermittently with tides and most significantly during strong tidal currents by ~50 % relative to the normal case (**Figure 2.11a**). At Sta. B, ~3.5 km from the TSTP, the level of *c* decreases to about a quarter of that at Sta. A, yet the reduction by the diversion reaches by ~50 % (**Figure 2.11b**). In contrast, the reduction of *c* at Sta. C occurs mostly in subtidal low frequencies. The subtidal variability dominates over the tidal variability, and thus the reduction due to the diversion lasts much longer in time (**Figure 2.11c**).

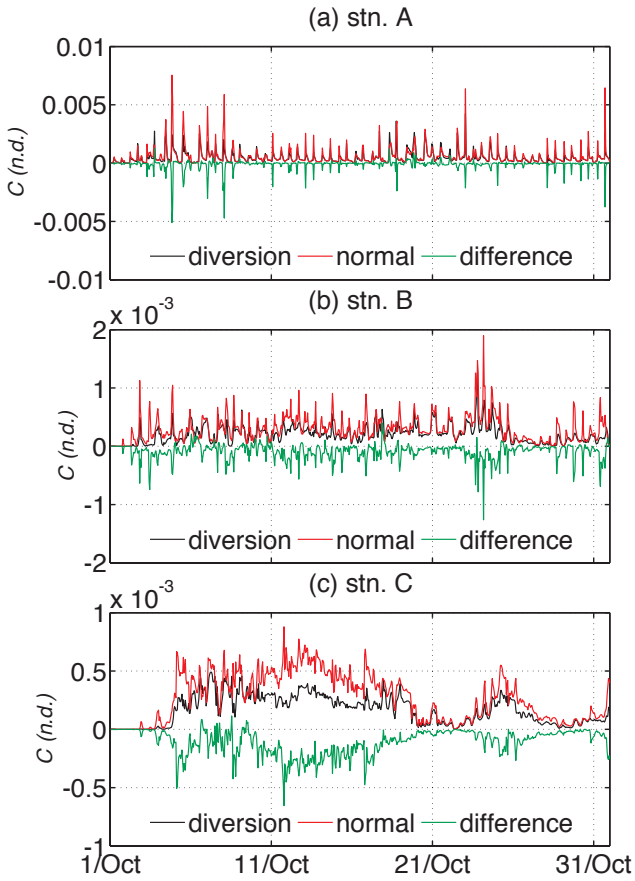

Figure 2.11. Time series plots of surface tracer concentration, *c*, at Stations A, B and C (**Figure 2.1c**). The black, red and green lines indicate the diversion, normal and difference (diversion - normal), respectively.

2.4.4 Effluent budget analysis

To quantify the direct impact of the sewage effluent on the seaweed farm for the two cases, we evaluate the effluent concentration flux crossing arbitrary section with an area A_c:

$$F = \int_{A_c} c u_n \, dA_c, \tag{2.5}$$

where A_c is the cross-sectional area, and u_n is the velocity normal to the section considered. Because c is dimensionless with normalization by the source concentration C_p, F has the unit of m^3s^{-1}. We further introduce the cumulative tracer flux Q (m^3) by integrating F over a given elapsed time period of t since $t = 0$:

$$Q(t) = \int_0^t F \, dt, \tag{2.6}$$

We show time series of the incoming cumulative fluxes Q, denoted by Q_{farm}, across the perimeter of the seaweed farm surrounded by four cross-sections (**Figure 2.1c**) since 0:00 UTC September 21 for the two cases as well as their difference, ΔQ_{farm}, defined as diversion – normal (**Figure 2.12**). Because the flux budget Q_{farm} for both cases is mostly positive, the effluent released from the TSTP gradually accumulates in the farm with time. The diversion yields less Q_{farm} than that for the normal case, leading to the net reduction of the effluent, *i.e.*, $\Delta Q_{farm} < 0$ (**Figure 2.12b**). The time-averaged Q_{farm} during the plotted period is also lower in the diversion case with 2.01×10^4 m^3 than the normal case with 2.83×10^4 m^3 (the time-averaged ΔQ_{farm} is -0.82×10^4 m^3), as summarized in **Table 2.3**. Temporal variability in Q_{farm} and ΔQ_{farm} consists of tidal and subtidal components, where the latter contributes more intensively than the former. Increase and subsequent decrease of Q_{farm} and ΔQ_{farm} occurs periodically at a period of ~14 days consistent with a spring-neap tidal cycle, with the maxima on October 3, 17, and 31. The peak Q_{farm} values are 1.84×10^4 m^3, 3.67×10^4 m^3, and 5.49×10^4 m^3 for the diversion case, while 3.51×10^4 m^3, 5.08×10^4 m^3, and 6.53×10^4 m^3 for the normal case, respectively. (**Fig. 2.12a**). The above results indicate that the diversion works adequately to reduce the sewage influence by ~28 % on the seaweed farm on average. It is worth addressing that the outgoing Q at the perimeter of the L4 domain, Q_{L4}, is dominated by that from the western open boundary toward Harima Sea owing to strong tidal currents formed near the Akashi Strait (**Figure 2.7a**), accounting for more than 75% of the total outgoing Q_{L4} (not shown). The difference in Q_{L4} between the two cases is subtle as for the short distance between the normal and diversion outfalls (500 m) relative to the size of the L4 domain. Doblin and Clayton (1995) reported that a high concentration of sewage effluent has a serious impact on the seaweed growth during its early life circle (*viz*., in fall). Maruyama *et al*. (1985) showed that the growth rate of seaweed, *Porphyra yezoensis*, is exponentially retarded due to the increased addition of sewage water under low sewage concentration

conditions (<5%). This is the case for the present conditions, where the surface concentration in the farm is only 0.1%–0.01% relative to that at the source (**Figure 2.8a**). Therefore, the estimated decrease of the sewage effluent of ~28% by the diversion is anticipated to be responsible for substantial positive impact on the growth of the seaweed.

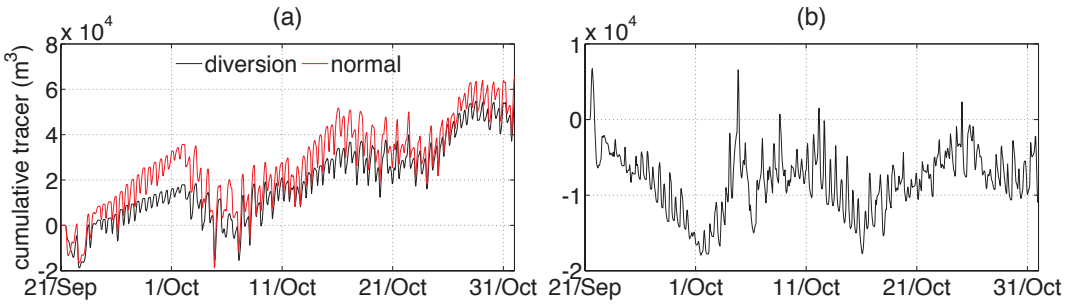

Figure 2.12. (a) Time series plot of temporally cumulative net tracer fluxes stored in the seaweed farm area, Q_{farm} (m^3). The black and red curves denote the diversion and normal cases. (b) The temporal changes of the difference of Q_{farm} (m^3) for the two cases: (diversion - normal).

Table 2.3. Cumulative non-dimensional tracer fluxes in the seaweed farm, Q_{farm} (m^3)

	Until Oct. 3rd	Until Oct. 17	Until Oct. 31	Average
Diversion	1.84×10^4	3.67×10^4	5.49×10^4	2.01×10^4
Normal	3.51×10^4	5.08×10^4	6.53×10^4	2.83×10^4
Difference	-1.67×10^4	-1.41×10^4	-1.04×10^4	-0.82×10^4

Difference: diversion - normal

Figure 2.13 shows time series of instantaneous F and cumulative Q at the four cross-sections surrounding the seaweed farm with the subscripts standing for the western, northern, eastern, and southern cross-sections; *e.g.*, F_w denotes F at the western cross-section. Note that the sum of the four cumulative fluxes is identical to Q_{farm}. Tidal and subtidal fluctuations are manifested in all the four F, yet their contributions differ from section to section. F_w and F_s fluctuates primarily at diurnal or semidiurnal tidal frequencies, while the lower-frequency subtidal contribution appears more prominently in F_n and F_e. Nevertheless, high-frequency tidal variability in the instantaneous fluxes has a minor or even negligible contribution to the net impact of the effluent. For instance, at the western section closest to the outfall, even if negative F_w prevails, the cumulative Q_w is positive and has an apparent increasing trend because the positive F_w lasts longer than the negative F_w (**Figure 2.13a** and **b**). The cumulative Q shows an increase, except for Q_s, where the largest amount of c discharges out of the farm, which is compensated for by the incoming c at the three other sections. Therefore, the direct impact from the TSTP manifests at the western and northern sections showing the highest transport offshore (southward) and eastward, yielding the overall cross- and alongshore gradients of the surface c, as shown in **Figure 2.8a**.

Q_e is provoked with a remarkable time lag of ~14 days behind Q_w, Q_n, and Q_s, in which the effluent appears immediately after the initialization. The farm is generally affected by the nearshore westward residual current (**Figure 2.7a**) that carries no effluent initially. Tidal currents give rise to oscillatory effluent transport back and forth in the alongshore direction within the farm. Hence, the farm is more influenced near the outfall (**Figure 8a**), attributed to the retarded initial arrival of the effluent. Yet the magnitude of Q_e is smallest among the four sections, since Q_e increases with time, the incoming flux dominates over the discharging flux. This result implies that the primary source of Q_e is the recurring effluent discharged out of the farm, likely the one passes through the southern section.

Although the diversion leads to the overall reduction of the effluent accumulation in the farm relative to the case with the normal outfall (**Figure 2.12**), it is not always the case at all the four sections. The diversion results in the increase of Q at the western and southern sections, while the latter is less contributed to the Q budget. Accordingly, the effluent from the diversion outfall provokes more notable alongshore transport in and around the farm, whereas the cross-shore, seaward transport prevails for the normal outfall. The increased Q_w for the diversion is somewhat counter-intuitive to the overall reduced c at the western section (**Figure 2.10**) with u_n unaltered substantially (not shown). Thus, these results indicate that the highly nonlinear, subtidal, and residual variability in c and u_n, and their phase relation are inevitable to accurately assess the flux cu_n quantitatively, which are all included in the present model.

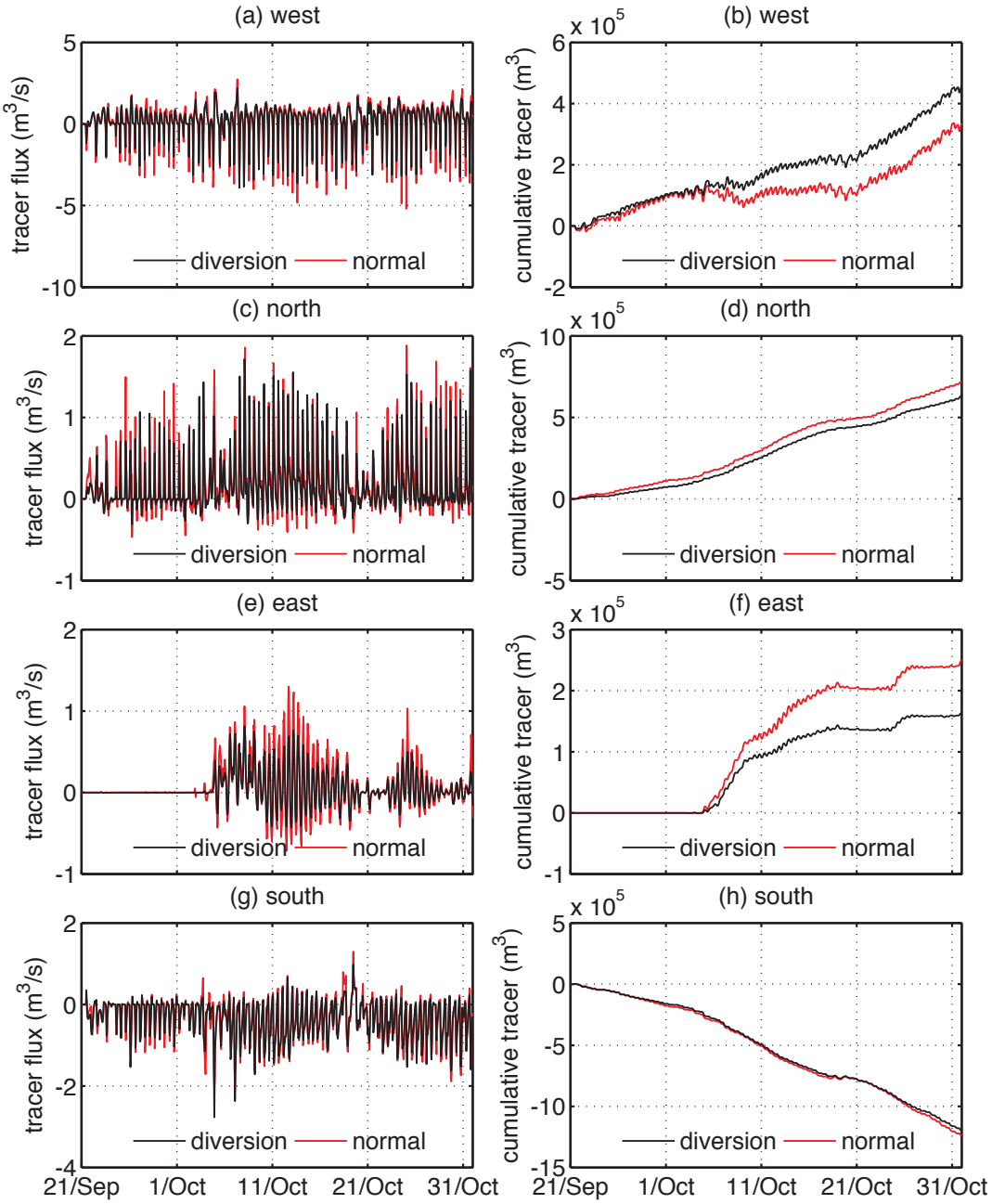

Figure 2.13. Time series plot of instantaneous tracer fluxed F (m^3/s, left panels) and the corresponding cumulative tracer fluxes Q (m^3, right panels) at the four boundaries surrounding the seaweed farm. From top to bottom, the figures show F and Q at the western, northern, eastern and southern transects, respectively. The black and red curves denote the values for the diversion and normal cases.

3. On relaxation of the effects of treated effluent on a seaweed farm

3.1 Methods

3.1.1 Ocean circulation model

We employed a 3D Eulerian passive tracer model with a near-field dilution sub-model (Uchiyama et al., 2014) to compute a 3D dispersal of the buoyant plume representing the effluent derived from the TSTP western diversion outfall (see Sec. 3.1.2). The tracer model was driven by the 3D velocity and eddy diffusivity estimated using the innermost child model of the quadruple-nested downscaling Regional Oceanic Modeling System (ROMS; Shchepetkin and McWilliams, 2005; 2008). The lateral boundary conditions for the outermost ROMS-L1 model were acquired from the assimilative Japan Coastal Ocean Predictability Experiments (JCOPE2) oceanic reanalysis (Miyazawa et al., 2009). The one-way offline nesting technique (e.g., Mason et al., 2010; Buijsman et al., 2012; Romero et al., 2013; Uchiyama et al., 2010; 2017a; 2017b; 2017c; 2018b; Kamidaira et al., 2017; 2018) was utilized to successively convey the parent model results into the child models with grid-size refinements (*i.e.*, JCOPE2 at a lateral grid resolution of ~10 km→ L1 at 2 km → L2 at 600 m → L3 at 100 m→ L4 at 20 m) as shown in **Figure 3.1**. Thus, the innermost ROMS-L4 model domain was discretized horizontally at 20 m lateral grid spacing, and vertically into stretched 32 *s*-layers. The ROMS configurations were the same as those in Uchiyama et al. (2018a). For instance, the L4 model was forced using the surface wind stress data from the Japan Meteorological Agency (JMA) Grid-Point Values–MesoScale Model (GPV-MSM; Isoguchi et al., 2010) and the surface heat/freshwater fluxes from the Comprehensive Ocean-Atmosphere Data Set (COADS; Woodruff et al., 1987). Along the L2 model open boundaries, the barotropic tides were synthesized from ten constituents acquired from the TPXO7.0 global reanalysis (Egbert et al., 1994; Egbert and Erofeeva, 2002) that spontaneously generated the intrinsic barotropic and baroclinic tides that were transmitted through the open boundaries into the L3 and L4 models. Because the seaweed spores are sensitive to both salinity and nitrate, the impacts of freshwater from the local rivers are worth considering. Therefore, freshwater discharge from the major rivers was also taken into account whenever needed. The ROMS-L4 model was run for approximately 50 days to include October 2015 when the seaweed spores were the most sensitive to the effluent. **Table 2.1** summarizes the detailed numerical configurations for the ROMS-L1-L4 models. Further details of the model design can be found in Uchiyama et al. (2018a).

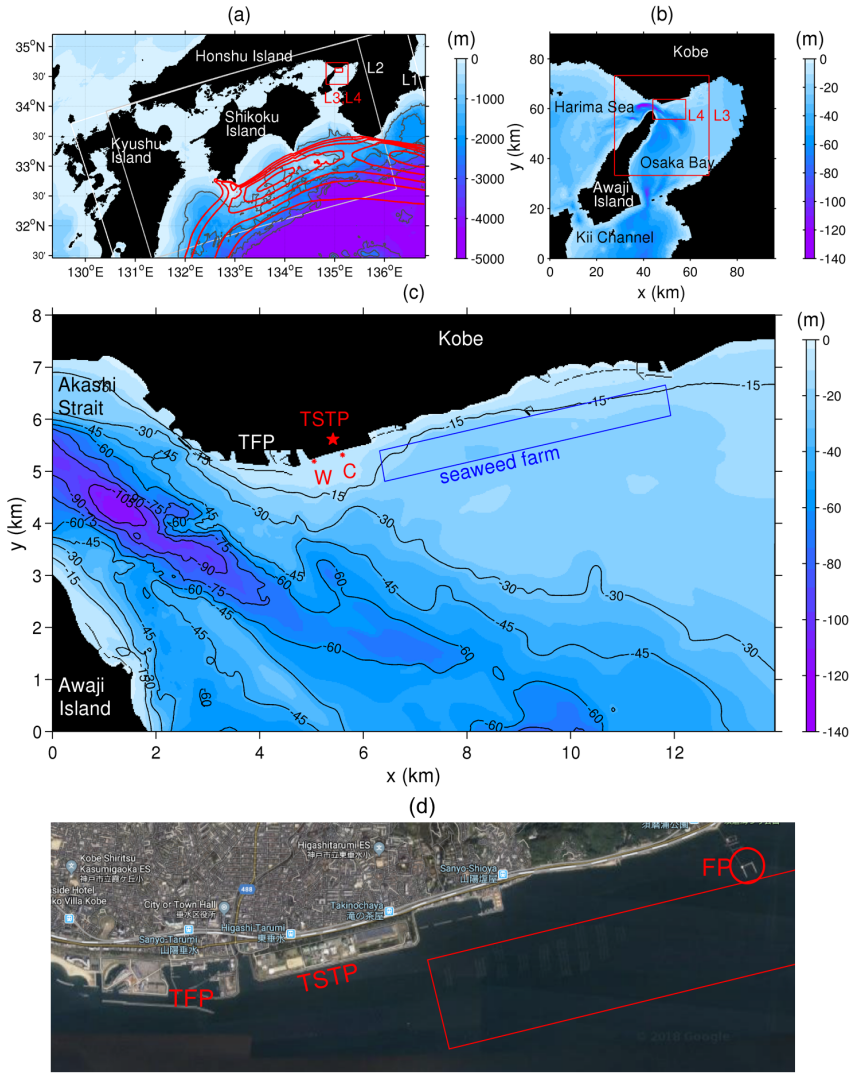

Figure 3.1. Quadruple-nested JCOPE2-ROMS model domains and bathymetry (color: m). (a) The ROMS-L1, L2 (white boxes), L3, and L4 domains (red boxes) embedded in the JCOPE2 domain (outside of the perimeter of the L1). The gray contours are the isobaths with 1,000 m intervals, while the red contours indicate the approximate Kuroshio region with the surface velocity magnitudes greater than 0.5 m s^{-1} at 0.2 m s^{-1} intervals. (b) The enlarged region around Osaka Bay including the ROMS-L3 and L4 domains (red boxes). (c) The entire L4 domain with isobaths at 15 m intervals. The blue box is the approximate extent of the seaweed farm area of interest; TFP is the Tarumi Fishery Port; the red star shows the location of the Tarumi Sewage Treatment Plant (TSTP); the red dots are the two outfalls (W: western diversion outfall, C: central original outfall). (d) Aerial photo around the TSTP from Google map. The seaweed farm (red box), TSTP, and TFP are indicated on the figure. The local fishing pier (FP) construction is shown by the red circle.

Table 3.1. Model configurations

Models	L1	L2
Computational period	3/1/2006-11/31/2015	9/1/2006-11/9/2015
Grid cells	320 × 320 (× 32 layers)	800 × 480 (× 32 layers)
Horizontal grid resolution	2 km	600 m
Baroclinic time step	120 s	30 s
Surface wind stress	JMA-MSM (hourly)	JMA-MSM (hourly)
Surface flux	COAMPS bulk formula	COAMPS bulk formula
Boundary/Initial condition	JCOPE2 (daily)	ROMS-L1 (daily)
T-S nudging	JCOPE2 (10-day averaged)	None
Topography	SRTM30+JEGG500	SRTM30+JEGG500

COAMPS: Coupled Ocean/Atmosphere Mesoscale Prediction System (Hodur, 1997)

STRM30: SRTM30_PLUS (Rodriguez et al., 2005; Rodriguez et al., 2006; Becker et al., 2009)

J-EGG500 (http://www.jodc.go.jp/data_set/jodc/jegg_intro.html)

Table 3.1. Model configurations (continued)

Models	L3	L4
Computational period	9/1/2015-11/9/2015	9/21/2015-11/9/2015
Grid cells	400 × 400 (× 32 layers)	696 × 400 (× 32 layers)
Horizontal grid resolution	100 m	20 m
Baroclinic time step	8.0 s	1.0 s
Surface wind stress	JMA-MSM (hourly)	JMA-MSM (hourly)
Surface flux	COADS (monthly climatology)	COADS (monthly climatology)
Boundary/Initial condition	ROMS-L2 (hourly)	ROMS-L3 (hourly)
T-S nudging	None	None
Topography	CDPC	CDPC

CDPC: Central Disaster Prevention Council, Japan (50m resolution)

3.1.2 Sewage effluent model

The 3D sewage effluent oceanic dispersal in the L4 domain was modeled as a conservation equation of the non-dimensional Eulerian passive tracer concentration c with the near-field dilution sub-model (Uchiyama et al., 2014; 2018a):

$$\frac{\partial c}{\partial t} + \nabla \cdot \mathbf{u}c = \mathcal{D} + \mathcal{P}, \tag{3.1}$$

where the near-field dilution is represented as the non-dimensional source term, $\mathcal{P}$:

$$\mathcal{P}(x, y, z; t) = P_s(t)A(x, y)H(z), \tag{3.2}$$

where $\mathbf{u}$ is the 3D velocity of the ambient flow, $\mathcal{D}$ is the diffusion term, ∇ is the 3D gradient operator, P_s is the tracer flux from the outfall, and A and H are the non-dimensional spatial plume shape functions above the bottom-mounted diffusers. The shape functions A and H were utilized to represent the source region spatial distribution as shown in the following integral relations:

$$\iint A\, dxdy = A_S, \ \int H\, dz = H_S, \tag{3.3}$$

where A_s is the horizontal area, H_s is the vertical size, and $V_s = A_s H_s$ is the sewage plume volume. Hence, $P_s(t) = Q_p(t)/V_s$, where $Q_p(t)$ [$m^3\ s^{-1}$] is the volume flux. The dimensional pollutant concentrations were retrieved using cC_p, where C_p is the input pollutant concentration at the outfall. Note that a similar source term is added to the 3D mass, momentum, salinity, and temperature conservation equations to account for the near-field dilution effects.

The shape functions A and H are described also according to Uchiyama et al. (2014). A Gaussian distribution model,

$$H(z) = \exp\left[-\frac{(z-z_s)^2}{d_s^2}\right], \tag{3.4}$$

was used for the vertical function H, where z_s is the plume center height, and d_s is the vertical scale of the plume. We defined $z_s = 0$ m and $d_s = 7$ m as the buoyant effluent was released from the bottom-mounted diffusers of the TSTP diversion outfall at a mean depth of 7 m. This depth is shallower than the local mixed layer depth, and thus the released buoyant effluent immediately reaches the surface. The outfall was represented by two grid points with a footprint of 20 m × 40 m, where $A = 0.5$, centered 40 m offshore from the TSTP sea wall, approximately corresponding to the actual diversion outfall design.

3.1.3 Standard and two alternative operation scenarios

The sewage effluent was applied to the coastal area near the TSTP as a bottom-released freshwater plume at the volume rate of Q_p with a prescribed concentration of $c = c_s$, yielding a source tracer flux at the outfall of $F_p = c_s Q_p$. The discharged hypothetical passive tracer was set to unity ($c_s = 1$) with the temperature of the ambient seawater, unless otherwise stated. For the standard diversion operation (Case 1: the baseline case), a constant volume rate $Q_p = 1.8 \times 10^5$ m^3 d^{-1} and zero salinity were imposed. The mean seawater surface temperature and salinity near the outfall were 23.0 °C and 34.4 psu. Hence, at 23.0 °C, the resultant mean density was 1023.48 kg m^{-3}, while the freshwater density was 997.55 kg m^{-3}.

The two alternative operations proposed by the KSB were then configured on the basis of the Case 1 experimental set-up. The first alternative was simply a reduced Q_p discharge volume from 1.8×10^5 m^3 d^{-1} to 1.5×10^5 m^3 d^{-1} with the other conditions retained (Case 2: the reduced Q_p case). Hence, the F_p source tracer flux was also lowered at the same reduction rate as the Q_p with $c_s = 1$. In the second scenario, the effluent density was increased by mixing with 0.8×10^5 m^3 d^{-1} of the ambient seawater to suppress the buoyant plume from surfacing during the initial dilution (Case 3: the increased density case). As a consequence, the total Q_p discharge rate, the density of the mixed effluent □', and its salinity S' were modified in Case 3 to $Q_p = 2.6 \times 10^5$ m^3 d^{-1}, □' = 1005.43 kg m^{-3}, and S' = 10.46 psu, respectively. We further modified the source tracer flux $c_s = (1.8 \times 10^5)/(2.6 \times 10^5) \sim 0.69$ such that the total tracer load from the TSTP for Case 3 was equal to Case 1, even with the seawater addition and density alteration. The vertical shape function H was not altered in all three cases as defined in Section 3.1.2. The model configurations for the three cases are summarized in **Table 3.2**.

Table 3.2. Different discharge operations scenarios

	Sewage volume (m^3/d)	Mixing seawater (m^3/d)	Salinity (psu)	Density (kg/m^3)
Case 1: baseline	1.8×10^5	None	0	997.55
Case 2	1.5×10^5	None	0	997.55
Case 3	1.8×10^5	8×10^4	10.46	1005.43

Note: the mean temperature was as that of ambient seawater at 23 ℃. The surface salinity and density of the seawater were 34.4 psu and 1023.48 kg m^{-3}, respectively.

3.2 Results and discussion

3.2.1 Residual currents

In basin-strait systems, tides are known to be the most influential factors to affect currents particularly near straits with intensive fluctuations at relatively small spatiotemporal scales (e.g., Imasato, 1983; Imasato et al., 1994; Li et al., 2015). The present study area is in a location where strong tidal currents are generated in the narrow Akashi Strait that could affect the transport and dispersal of sewage effluents from the TSTP. Strong tidal currents are repeatedly generated at the narrow Akashi Strait. **Figure 3.2a** shows the surface residual currents in Case 1 estimated for the entire experimental period from September 21st to October 31st, 2015. Overall, the strong southeastward residual currents form and intrude into Osaka Bay through the Akashi Strait. These residual currents involve three major circulations. The largest is a clockwise circulation formed as a part of the well-known 'Okinose Circulation' (e.g., Nakatsuji et al., 1994; Mishima et al., 1999) that appears as a semi-circle with the origin at approximately (x, y) = (4 km, 0 km). Consistent with the findings in Imasato (1983), the intermediate counterclockwise circulation (hereafter termed the 'Tarumi Recirculation') develops with the prominent westward alongshore current near the TSTP. The smallest local recirculation is instigated off the northern coast of the Akashi Strait. The two counter-rotating larger circulations converge at around (x, y) = (4 km, 4 km) and develop into the intensive southeastward current. In turn, the strongest northwestward current occurs along the northern coast of Awaji Island and then veers clockwise at two locations in the Akashi Strait to form two clockwise circulations including the Okinose Circulation. As was reported in Uchiyama et al. (2018a), the Tarumi Recirculation is substantially important for promoting the mean westward transport of effluent from the TSTP that is ultimately responsible for reducing effluent accumulations in the seaweed farm using the diversion operation.

It is worth mentioning that the velocity vectors in **Figure 3.2a** are subsampled every 20 grids, resulting in lack of the detailed flow structures that should be observable in the ROMS-L4 model outcome with a lateral grid resolution of 20 m. Two selected enlarged regions shown in **Figure 3.2b-c** demonstrate the influences of man-made marine constructions in the red dotted boxes labeled with z1 and z2 in **Figure 3.2a**, where the velocity vectors were then subsampled every 5 grids. We now see the complex residual current field around the foundation of a fishing pier (indicated as "FP" in **Figure 3.1d**) in **Figure 3.2b**. The pier has significant effects on the local residual currents, where zonal divergence occurs with obvious opposing eastward flows in the downstream region. The southward transport is formed locally near the pier crossing the northern perimeter of the seaweed farm depicted by the red line. On the western area of the TSTP, the Tarumi Fishery Port ("TFP" in **Figure 3.1d**) breakwater provokes a bifurcation of the westward coastal residual current with noticeable velocity weakening, southward veering, and a tiny local clockwise recirculation along the southern side (**Figure 3.2c**).

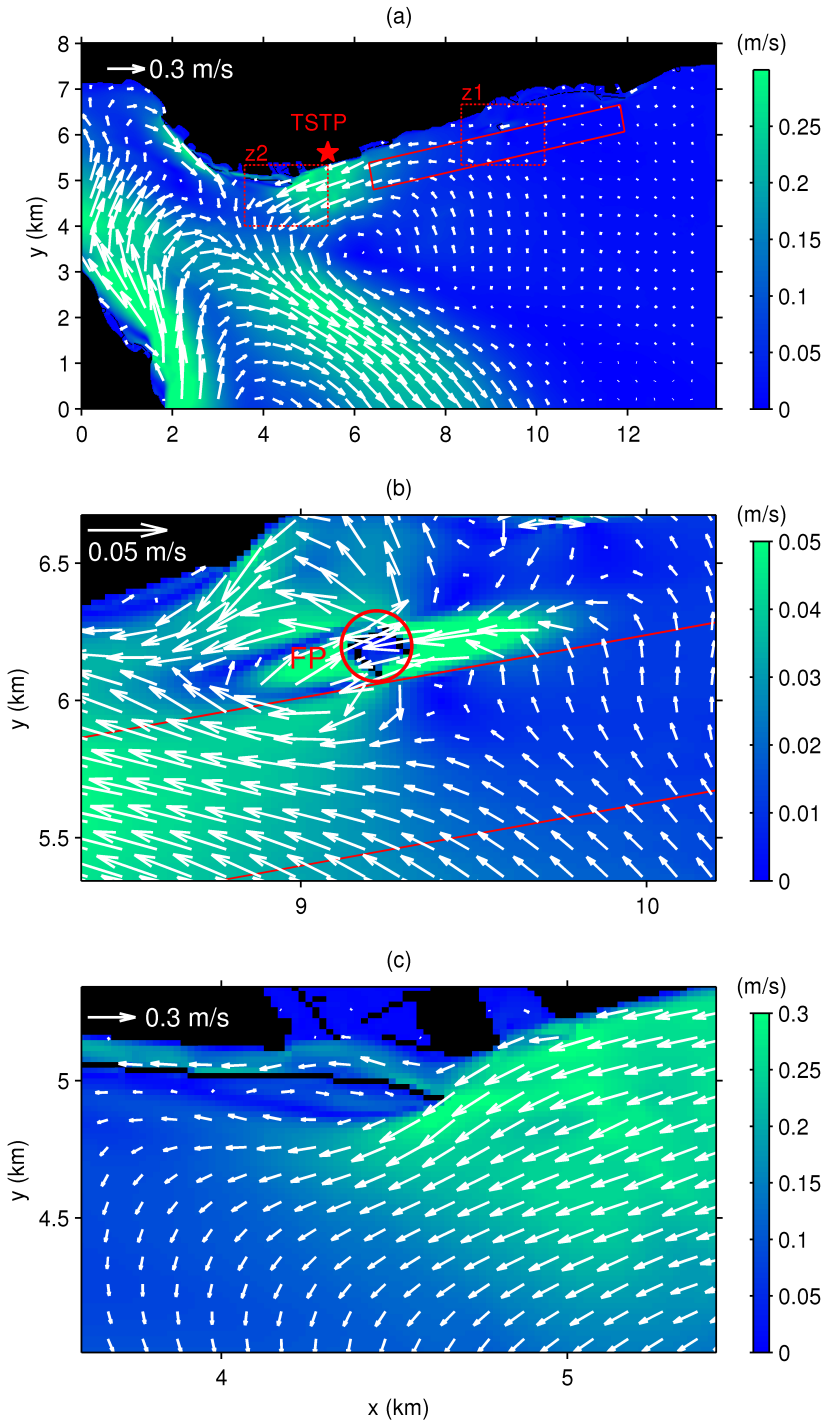

Figure 3.2. (a) Time-averaged surface velocity vectors (white arrows) on their own magnitude (color). (b) Same as (a) but for the enlarged region shown by the red dotted box (z1) in **Figure 3.2a**. The location of the fishing pier (FP) construction is shown by the red circle. (c) Same as (a) but for the enlarged region shown by the red dotted box (z2) in **Figure 3.2a**. The red solid box shows the seaweed farm area.

3.2.2 Time-averaged density and effluent concentration

As the seaweed is cultivated near the surface for adequate photosynthesis conditions (Abowei and Ezekiel, 2013), we primarily investigated the effluent transport in the upper ocean, albeit its substantial 3D behavior crucial to its accumulation in the seaweed farm. **Figure 3.3** shows the time-averaged non-dimensional tracer (effluent) concentration c (color) and the seawater density (contours) at the surface from September 21st to October 31st, 2015. The top panel corresponds to Case 1 (the baseline case with $Q_p = 1.8 \times 10^5$ m^3 d^{-1}), while the other two panels represent the deviations for Case 2 (reduced $Q_p = 1.5 \times 10^5$ m^3 d^{-1}, middle) and Case 3 (increased density, bottom), where the deviations are defined as (Case 2 – Case 1) and (Case 3 – Case 1), respectively. Consistent with the residual current field (**Figure 3.2a**), for the baseline case shown in **Figure 3.3a**, the mean effluent concentration c is mostly distributed in the alongshore direction near the TSTP with a pronounced westward bias and suppressed cross-shore transport. Similar to the c distribution, slight decreases in the surface density occur because of the fresh effluent discharge from the diversion outfall. Another density decrease is observed in the northeastern area of the seaweed farm, and is attributed to both the fresh effluent and to remote influences from major river mouths located in the inner Osaka Bay ~30 km east of the study area (see also Uchiyama et al., 2018a).

The effluent concentration and density surface deviations observed for Case 2 are generally consistent although with opposite signs (**Figure 3.3b**). The surface density □ slightly increases around the TSTP due to the reduced fresh effluent, while c is diminished. Noticeable modifications in □ and c are observed only within ~2 km from shore, whereas they extend to the western area of the seaweed farm. Density deviations could dynamically alter the local flow field due to buoyancy effects that may further affect the tracer transport, in addition to the reduced tracer flux at the outfall. In Section 3.2.3, the tracer budget analysis to quantify the effects of the reduced tracer flux F_p at the outfall on the seaweed farm is presented. By contrast, the adjusted effluent density with the unchanged total tracer flux (Case 3) does not result in obvious changes in □ and c, particularly at the seaweed farm, except for the source area (**Figure 3.3c**). We expected for Case 3 that the suppressed surface c from the density change could cause a decrease in the near-surface c transport to the farm, whereas this may not be the case in the present situation where the outfall is located in a very shallow area at 7 m deep. Section 3.2.3 also quantifies the effects of the adjusted density changes in the effluent accumulation in the farm.

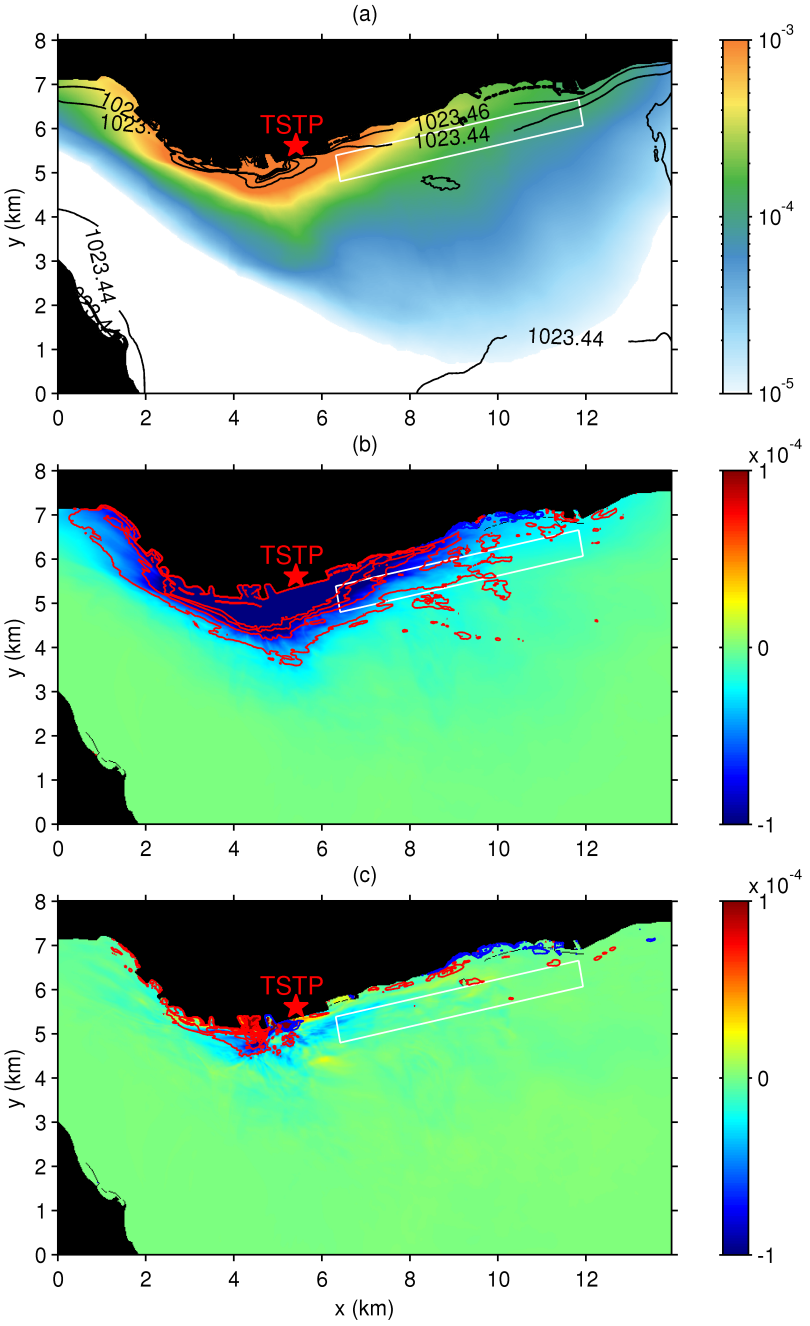

Figure 3.3. (a) Time-averaged passive tracer concentration, *c* (color, non-dimensional) at the surface for the baseline case (Case 1). The black contours denote the sea surface density at 0.02 kg m^{-3} intervals. (b) The differences in *c* (color, non-dimensional) and density (contours) between Case 2 and Case 1 (Case 2 – Case 1). The red and blue contours are positive and negative values (intervals: 0.001 kg m^{-3}). (c) Same as (b), but for Case 3 – Case 1.

3.2.3 Effluent flux budget analysis

A quantitative effluent tracer budget analysis is carried out to evaluate the direct impacts of the TSTP on the seaweed farm for the three cases. Considering a vertical section surrounding the farm with an arbitrary cross-sectional area of A_c, the instantaneous tracer flux F crossing the section is calculated with

$$F(\tau) = \int_{A_c} c u_n \, dA_c, \tag{3.5}$$

where u_n is the velocity perpendicular to the cross-section, and □ is time. Because c is a non-dimensional concentration, F has the unit of $m^3\ s^{-1}$. Then, we integrate F over a given time period to evaluate the cumulative tracer flux Q (m^3) for the duration from □ = 0 to t as follows:

$$Q(t) = \int_0^t F(\tau) \, d\tau, \tag{3.6}$$

where the incoming cumulative tracer fluxes into the farm are defined as positive at each of the four sections surrounding the farm as represented by blue lines in **Figure 3.1c**. Hence, the sum of Q at the four vertical cross-sections identifies the net tracer (effluent) flux Q_{farm} accumulated in the seaweed farm, *i.e.*, $Q_{farm} = Q_w + Q_n + Q_e + Q_s$, where Q_w, Q_n, Q_e, and Q_s are the cumulative fluxes Q (t) through the western, northern, eastern, and southern sections, respectively. To distinguish Q_{farm} for the three cases, we denote the net flux as Q_1, Q_2, and Q_3 for Q_{farm} for Cases 1, 2, and 3.

Figure 3.4a shows the net cumulative tracer temporal variability in the seaweed farm for the three cases. As time progressed from the initial state with no effluent, the released effluent from the TSTP gradually accumulates in the farm, with apparent tidal and subtidal variabilities in all three cases. Q_1 and Q_3 have similar fluctuations, although Q_2 deviates from the others later in the experiments. The result is consistent with the time-averaged surface tracer concentrations shown in **Figure 3.3**, whereas c is significantly reduced in Case 2. Nevertheless, the increased effluent density in Case 3 does not appreciably influence the effluent accumulation in the farm. **Figure 3.4b** shows the Q_{farm} differences of Cases 2 and 3 from Q_1, in which we denote □$Q_{21} = Q_2 - Q_1$ and □$Q_{31} = Q_3 - Q_1$. The differences clearly indicate that the net tracer accumulation is significantly diminished in Case 2 (□$Q_{21} < 0$), while the reduction in Case 3 is subtle (□$Q_{31} \sim 0$). The results are quantitatively summarized in **Table 3.3** for three selected durations from Sept. 21 and their time averages over the experimental period. The averaged net cumulative tracers are determined to be $2.01 \times 10^4\ m^3$, $1.50 \times 10^4\ m^3$, and $1.98 \times 10^4\ m^3$ for Cases 1–3, respectively. The density change in Case 3 is again confirmed to scarcely alter the effluent accumulation. However, the released flux reduction of 16.7% ($1.8 \times 10^5\ m^3 d^{-1}$ → $1.5 \times 10^5\ m^3 d^{-1}$) at the diversion outfall in Case 2 results in a 25.4% reduction ($2.01 \times 10^4\ m^3$ → $1.50 \times 10^4\ m^3$) in the effluent accumulation in the farm relative to Case 1. These results firmly indicate that the complicated currents and associated dispersal near the TSTP have nonlinear influences on total tracers released at the outfall. As shown in

Figure 3.4a, the Q_{farm} (Q_1, Q_2, and Q_3) variability is dominated by low-frequency subtidal fluctuations that yield Q_{farm} peaks on October 3, 17, and 21, thus occurs at a period of ~14 days. This periodic behavior indicates that intrusion of the sewage effluent into the seaweed farm occurs mainly at a spring–neap tidal cycle. Consistent with the mean accumulations, **Table 3.3** shows that the Q_{farm} peaks for these three days are 1.84×10^4 m^3, 3.67×10^4 m^3, and 5.49×10^4 m^3 for Case 1, 1.60×10^4 m^3, 2.78×10^4 m^3, and 4.15×10^4 m^3 for Case 2, and 1.85×10^4 m^3, 3.66×10^4 m^3, and 5.22×10^4 m^3 for Case 3. In summary, the decreased source flux in Case 2 is more efficient than expected for reducing the effluent in the farm, whereas the density changes in Case 3 are not very efficient in the present configuration.

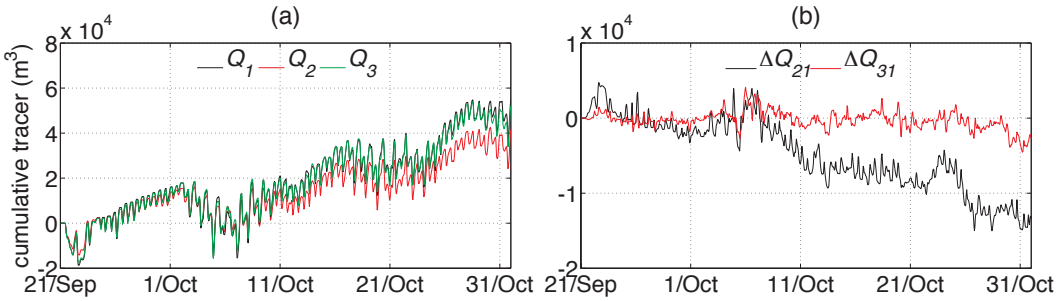

Figure 3.4. (a) Time series of the temporally cumulative net tracer fluxes stored in the seaweed farm area, Q_{farm} (m^3). The black, red and green curves show Q_1, Q_2 and Q_3 for Cases 1, 2, and 3, respectively. Note that Q_1 nearly coincides with Q_3. (b) The temporal changes in the Q_{farm} (m^3) differences for each case. The black curve ΔQ_{21} is for Case 2 – Case 1, while the red curve ΔQ_{31} is for Case 3 – Case 1.

Table 3.3. Cumulative non-dimensional tracer fluxes in the seaweed farm, Q_{farm} (m^3)

	Up to Oct. 3rd	Up to Oct. 17	Up to Oct. 31	Average
Q_1	1.84×10^4	3.67×10^4	5.49×10^4	2.01×10^4
Q_2	1.60×10^4	2.78×10^4	4.15×10^4	1.50×10^4
Q_3	1.85×10^4	3.66×10^4	5.22×10^4	1.98×10^4
ΔQ_{21}	-0.24×10^4	-0.89×10^4	-1.34×10^4	-0.51×10^4
ΔQ_{31}	0.1×10^4	-0.01×10^4	-0.27×10^4	-0.03×10^4

Note: $\Delta Q_{21} = Q_2 - Q_1$, $\Delta Q_{31} = Q_3 - Q_1$.

3.2.4 Effects of the mean and transient flow components on the tracer fluxes

The counterclockwise residual Tarumi Recirculation formed off the TSTP (**Figure 3.2a**) is anticipated to contribute to a 25.4% reduction in the effluent accumulation in the farm due to the 16.7% decrease in the input flux. However, as long as the residual current field is not altered by the reduced fresh effluent flux from the outfall, the nonlinear influence observed in Case 2 may rarely occur. To examine the possible mechanism behind the nonlinearity, we introduce a Reynolds decomposition to the prognostic variables for the mean and transient components, in which $c = \bar{c} + c'$ and $u_n = \overline{u_n} + u_n{}'$. Therefore, the time-averaged tracer flux $\overline{cu_n}$ is decomposed as

$$\overline{cu_n} = \bar{c}\,\overline{u_n} + \overline{c'\,\overline{u_n}} + \overline{\bar{c}u_n'} + \overline{c'u_n'} = \bar{c}\,\overline{u_n} + \overline{c'u_n'}, \tag{3.7}$$

where the overbar denotes an ensemble (time) averaging operator, and the prime represents the transient component that is the deviation from the ensemble mean and explains fluctuations associated mostly with eddies and tides. The first term $\bar{c}\,\overline{u_n}$ on the right hand side represents the linear interaction of the mean tracer concentration $\bar{c}$ and residual currents $\overline{u_n}$, whereas the second term $\overline{c'u_n'}$ denotes the tracer flux associated with the nonlinear interaction of the transient currents u_n' with the instantaneous tracer concentration c'. Note that the high-frequency turbulent components are included in the transient component, although they are subtle as compared to tidal and subtidal eddy components (Uchiyama et al., 2018a).

Figure 3.5 illustrates the cross-sectional distributions of the time-averaged flux $\overline{cu_n}$ ($m^3\ h^{-1}$, top panels), the mean linear component $\bar{c}\,\overline{u_n}$ (middle panels), and the nonlinear transient component $\overline{c'u_n'}$ (bottom panels) along the northern boundary of the seaweed farm from September 21st to October 31st, 2015. For Case 2 (left column) and the deviations from those for Case 1 (Case 2 – Case 1, right column). As u_n is the velocity component normal to the northern section, **Figure 3.5** principally depicts the cross-shore tracer transport, where the positive flux denotes the incoming flux into the farm. The total flux $\overline{cu_n}$ is generally positive, indicating an overall southward intrusion of the TSTP-derived effluent into the farm. In particular, this occurs in the western area ~3 km from the northwestern corner of the farm (**Figure 3.5a**, warm color), even though the westward residual current is formed as a part of the counter-clockwise circulation in this location (**Figure 3.2a**). An observable opposing outgoing flux occurs locally around the middle part of the northern section (cold color) that is most likely caused by the influences from the fishing pier (**Figure 3.2b**). The reduced source tracer flux in Case 2 successfully causes an overall reduction in the incoming flux $\overline{cu_n}$ (**Figure 3.5b**). The decomposed flux components (**Figure 3.5c**, **e**) and their differences from those in Case 1 (**Figure 3.5d**, **f**) demonstrate the striking predominance of the transient component $\overline{c'u_n'}$ over the mean component $\bar{c}\,\overline{u_n}$. The mean component is slightly negative because of the outgoing northward residual currents formed along the northern section (e.g., **Figure 3.2b**). Nevertheless, the nonlinear transient flux plays a dominant role in the overall

incoming flux and its reduction associated with the decreased source flux in Case 2 (**Figure 3.5e**, **f**). The superiority of the transient component over the mean component is also observed in the southern cross-section of the farm, albeit with an outflux dominance in that location (not shown). It should be noted that **Figure 13** in Uchiyama et al. (2018a) showed that a net effluent accumulation occurs in the alongshore direction with persistent incoming effluent fluxes both along the western and eastern sections, while a net reduction occurs in the cross-shore direction due to the prevailing outgoing effluent fluxes from the southern section.

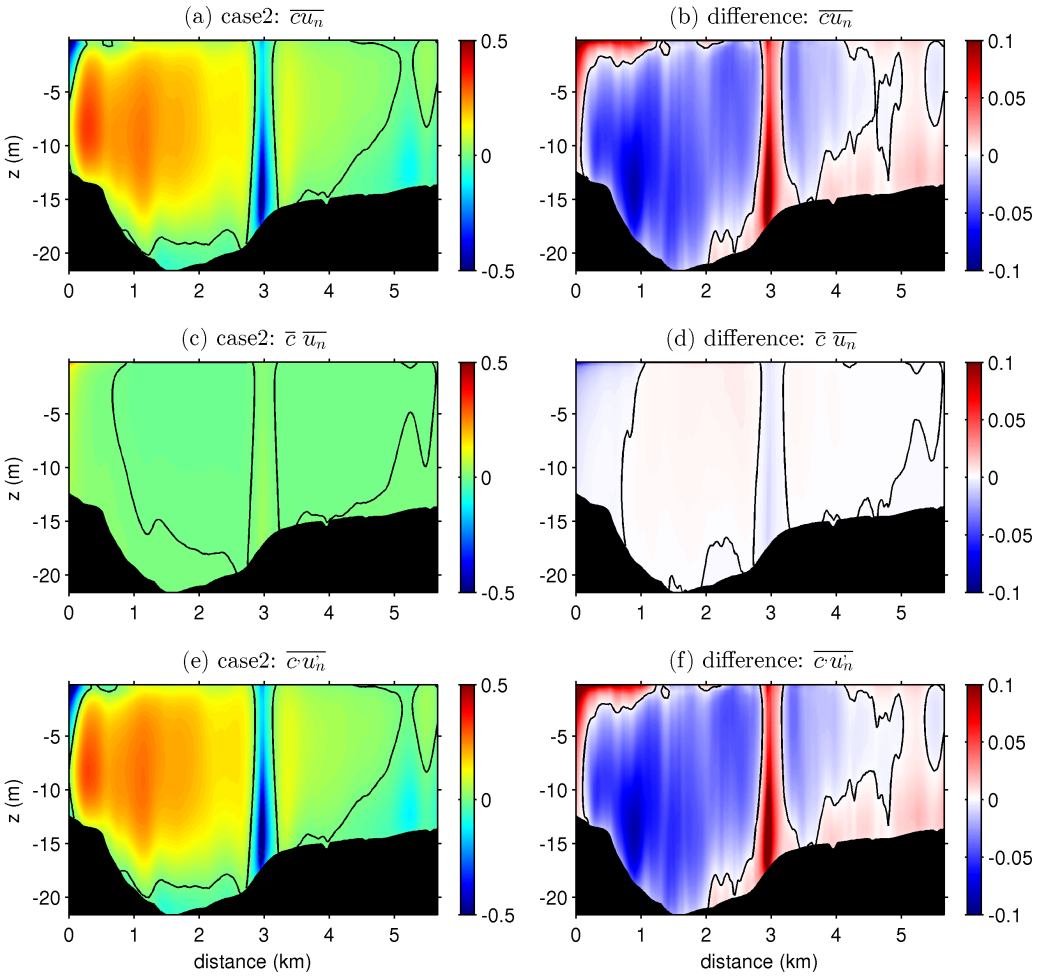

Figure 3.5. Cross-sectional distributions of (a) the time-averaged flux $\overline{cu_n}$ ($m^3\,h^{-1}$), (c) the mean linear component $\bar{c}\,\overline{u_n}$ ($m^3\,h^{-1}$), and (e) the transient flow component $\overline{c'u_n'}$ ($m^3\,h^{-1}$) at the northern boundary of the seaweed farm for Case 2, (b), (d) and (f) show the difference of $\overline{cu_n}$ $\bar{c}\,\overline{u_n}$ and $\overline{c'u_n'}$ between Case 2 and Case 1 (Case 2 – Case 1). The black contours denote 0.

Figure 3.6 is the same as **Figure 3.5**, except that it shows the western cross-section of the seaweed farm. Note that the depicted fluxes are mainly the alongshore tracer transport as u_n becomes the normal component in the western section. The Case 2 time-averaged tracer flux $\overline{cu_n}$ (**Figure 3.6a**) shows that the flux of the discharged effluent is largely positive (flowing into the farm represented by warm colors) and occurs more intensively in the lower layer peaking at around z = –10 m in the northern part of the cross-section closer to the TSTP, while it is rather outgoing near the surface (cold colors). As compared to the baseline case, Case 2 results in an increased tracer influx near the surface and a reduction in the deep layer (**Figure 3.6b**). The contributions from the mean linear components $\bar{c}\,\overline{u_n}$ and the transient nonlinear components $\overline{c'u_n'}$ (**Figure 3.6c**, **e**) are completely different from those along the northern section shown in **Figure 3.5c**, **e**. Both components are similar in magnitude, but with opposite signs. Although $\overline{c'u_n'}$ is generally positive for inducing overall incoming tracer fluxes into the farm, $\bar{c}\,\overline{u_n}$ counteracts to extract the effluent from the farm. The negative $\bar{c}\,\overline{u_n}$ is apparently attributed to the westward residual current in front of the TSTP (**Figure 3.2a**). However, as compared to Case 1, $\bar{c}\,\overline{u_n}$ enhances the effluent accumulation in the farm (**Figure 3.6d**), while $\overline{c'u_n'}$ depresses effluent intrusion into the farm (**Figure 3.6f**). The resultant net effects of the reduced source flux at the outfall (Case 2) are to overall reduce effluent accumulation in the farm (**Figure 3.6b**). By contrast, at the eastern transect, the mean $\bar{c}\,\overline{u_n}$ leads to an increased influx, while the transient $\overline{c'u_n'}$ reduces the accumulation in Case 2 relative to Case 1 (not shown). Nevertheless, the eastern section is located farthest from the outfall and thus the effluent influx along this section on the net tracer budget was subtle.

The present tracer budget analysis provides important insights into the assessment of this type of treatment plant operations. Synchronous observation of the transient currents and effluent concentrations is crucial for proper flux estimations, yet such observations are laborious. A simple multiplication of the residual currents and mean concentrations could yield an incorrect effluent flux, where nonlinear interactions between the transient currents and concentrations generate predominant mean fluxes through their interactions. Moreover, the significance of $\overline{c'u_n'}$ arises differently in the alongshore and cross-shore effluent transports. The residual counterclockwise circulation that transports the effluent away from the farm largely affects the seaweed farm near the TSTP, although the nonlinear transient flux brings more complexity to the mechanism.

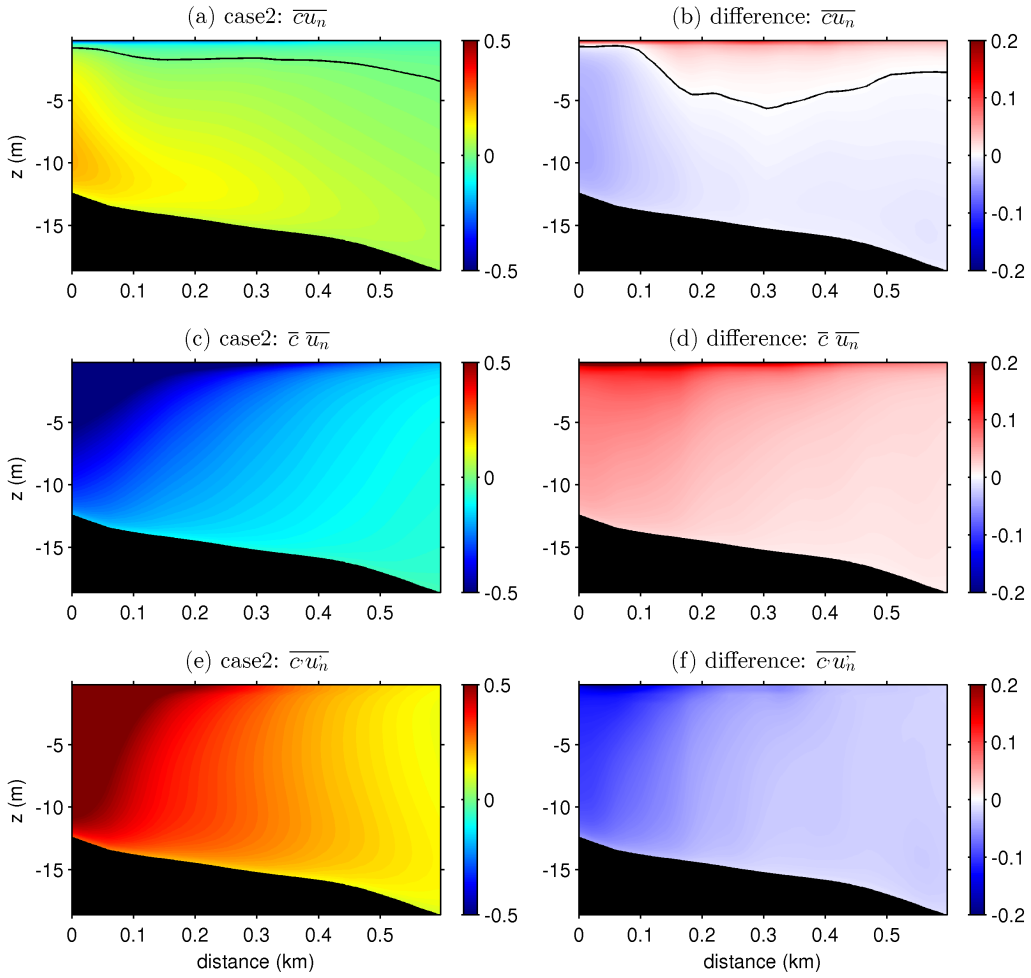

Figure 3.6. Same as **Figure 3.5**, but for the western cross-section of the seaweed farm.

4. Seasonal variability of upper ocean primary production

4.1 Methods

4.1.1 Ocean circulation model

We exploited a downscaling ocean model based on the Regional Oceanic Modeling System (ROMS; Shchepetkin and McWilliams, 2005, 2008) coupled with a nitrogen-based pelagic NPZD biogeochemical model (Section 4.1.2), encompassing both KR and KE regions (Uchiyama et al., 2017) as shown in **Figure 4.1**. The initial and side boundary conditions for the ROMS were provided by the monthly climatology of the assimilative JCOPE2 oceanic reanalysis (Miyazawa et al., 2009). A one-way offline nesting technique was employed to convey the parent JCOPE2 to the child ROMS model with grid resolution refinement (e.g., Mason et al., 2010; Kamidaira et al., 2017; Uchiyama et al., 2018a, 2018b, 2018c; Zhang et al., 2019). Therefore, the horizontal grid spacing was successfully reduced from 1/12° (~10 km, the JCOPE2 reanalysis) to 3 km (the ROMS model), and vertically into stretched 32 s-layers (Shchepetkin and McWilliams, 2005) with grid height refinement near the surface and bottom to solve the boundary layers adequately. We employed the K-Profile Parameterization (KPP) mixed-layer turbulence model described in Large et al. (1994) and Lemarié et al. (2012) to resolve the vertical momentum and tracer mixing. With the 3-km grid resolution, the present model is considered to be a submesoscale eddy-permitting model, in which submesoscale eddies can marginally be represented adequately (Uchiyama et al., 2017). The SRTM30_PLUS product (Rodriguez et al., 2005; Rodriguez et al., 2006; Becker et al., 2009) at a 30 arc second resolution and the 500m-resolution J-EGG500 (http://www.jodc.go.jp/data_set/jodc/jegg_intro.html) complementarily provided the present model bathymetry. The ROMS model was forced by the daily climatology of the GPV-GSM surface wind stress (e.g., Roads, 2004) provided by the Japan Meteorological Agency (JMA). The surface heat and freshwater fluxes were obtained from the monthly climatology of the Comprehensive Ocean-Atmosphere Data Set (COADS; Woodruff et al., 1987). Additionally, a four-dimensional temperature and salinity (TS) nudging (also known as robust diagnostic; e.g., Marchesiello et al., 2003) was used to improve the Kuroshio path reproducibility with a weak nudging inverse time scale of 1/20 per day. **Table 4.1** summarizes the detailed numerical configurations for the ROMS models.

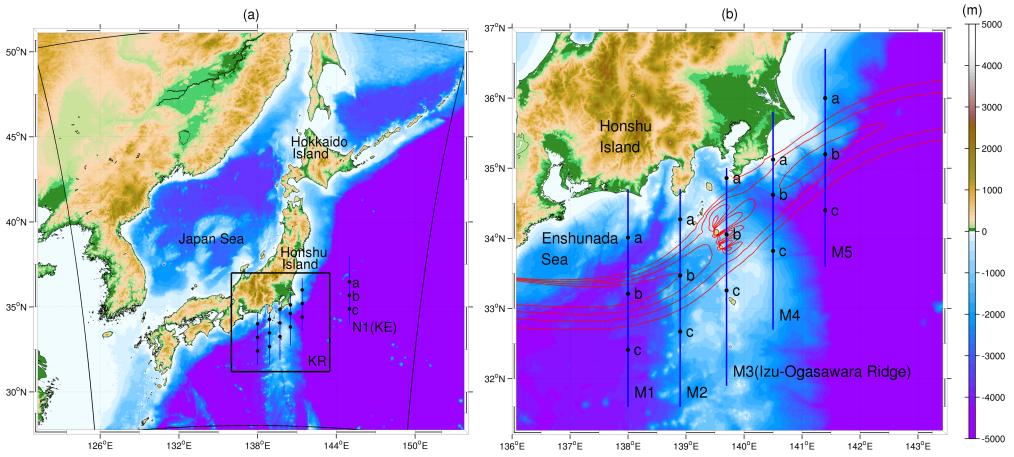

Figure 4.1. (a) The ROMS-NPZD model domain encompassing the Kuroshio Region (KR) and the Kuroshio Extension Region (KE). The thick black box indicates the KR, while the outer square corresponds to the perimeter of the model domain. The blue line annotated with N1 is the selected transect along 145°E, a representative of the KE, with three black dots on N1 show the sampling locations for Hovmöller plots (**Figure 4.4**). (b) The enlarged view of (a) corresponding to the black box in (a). The five blue lines represent the selected transects along 138°E, 138.9°E, 139.7°E, 140.5°E, and 141.4°E in the KR, named M1-M5, that are used for the subsequent analyses. The black dots on M1-M5 again show the locations used for Hovmöller plots in **Figures 4.3, 4.9, 4.10, and 4.11**. Red contours indicate the approximate Kuroshio path with surface velocity magnitudes ≥ 0.5 m/s at intervals of 0.3 m/s. Colors are bathymetry.

Table 4.1. Ocean circulation model configurations

Models	ROMS
Computational period	Climatological 10 years
Grid cells	784 × 864 (× 32 layers)
Horizontal grid resolution	3 km
Baroclinic time step	150 s
Surface wind stress	JMA-GSM (daily climatology)
Surface flux	COADS (monthly climatology)
Boundary/Initial condition	JCOPE2 (monthly climatology)
T-S nudging	JCOPE2 (10-day averaged climatology)
Topography	SRTM30+JEGG500

STRM30: SRTM30_PLUS (Rodriguez et al., 2005; Rodriguez et al., 2006; Becker et al., 2009)
J-EGG500 (http://www.jodc.go.jp/data_set/jodc/jegg_intro.html)

4.1.2 Biogeochemical model

We employed a simple nitrogen-based pelagic NPZD biogeochemical model based on Fasham et al. (1991) with a modification described in Gruber et al. (2006), where we considers five components: nitrate $[NO_3^-]$, ammonium $[NH_4^+]$, phytoplankton $[Phyt]$, zooplankton $[Zoo]$ and detritus $[Det]$. The conservation equations are given as followed:

$$\frac{D}{Dt}[NO_3^-] = -Q_1 \ , \tag{4.1}$$

$$\frac{D}{Dt}[NH_4^+] = -Q_2 + \mu_{[Zoo][NH_4^+]} \cdot [Zoo] + \mu_{[Det][NH_4^+]} \cdot [Det] \ , \tag{4.2}$$

$$\frac{D}{Dt}[Phyt] = -\left(\mu_{[Phyt]} + \mu_{[Phyt][Det]}\right) \cdot [Phyt] - G + Q_1 + Q_2, \tag{4.3}$$

$$\frac{D}{Dt}[Zoo] = -\left(\mu_{[Zoo]} + \mu_{[Zoo][NH_4^+]} + \mu_{[Zoo][Det]}\right) \cdot [Zoo] + \beta \cdot G \ , \tag{4.4}$$

$$\frac{D}{Dt}[Det] = -\left(\mu_{[Det]} + \mu_{[Det][NH_4^+]}\right) \cdot [Det] + (1-\beta) \cdot G + \mu_{[Phyt][Det]} \cdot [Phyt] + \mu_{[zoo][Det]} \cdot [Zoo], \tag{4.5}$$

where D/Dt is the material derivative including 3-D advection, vertical settling of $[Phyt], [Zoo]$ and $[Det]$, and vertical eddy diffusive fluxes computed by the KPP model (Large et al., 1994). Q_1 indicates the rate of nitrate uptake by phytoplankton, Q_2 denotes the rate of ammonium uptake by phytoplankton, and G is the rate of phytoplankton grazing by zooplankton. These three terms are given by:

$$Q_1 = \frac{\alpha_J \cdot [Phyt] \cdot [NO_3^-] \cdot e^{-\emptyset \cdot [NH_4^+]}}{K_{NO_3^-} + [NO_3^-]}, \tag{4.6}$$

$$Q_2 = \frac{\alpha_J \cdot [Phyt] \cdot [NH_4^+]}{K_{NH_4^+} + [NH_4^+]}, \tag{4.7}$$

$$G = \frac{g_{max} \cdot [Phyt] \cdot [Zoo]}{K_{Phyt} + [Phyt]}. \tag{4.8}$$

where α_J is the light limited growth rate with unit of d^{-1} as a function of photosynthetically active radiation (PAR) and the maximum growth rate [Eqs. 4-5 in *Fasham et al*., 1990]. The other model parameters are summarized in **Table 4.2**.

The seasonal climatology of the World Ocean Atlas 2005 (WOA05) (e.g., Garcia et al., 2006) and the monthly climatology of the MODIS/Aqua satellite data (https://oceandata.sci.gsfc.nasa.gov/MODIS-Aqua/) provided the initial and lateral

boundary conditions for nitrate and phytoplankton. In the present study, we follow the configuration described in Gruber et al. (2006) and Uchiyama et al. (2017) to set zooplankton to be proportional to chlorophyll-a (Chl-a) concentration for its initial and boundary conditions. Meanwhile ammonium and detritus are initialized to be zero. More details on the modeling approach of the current ROMS-NPZD model were reported in Uchiyama et al. (2017). The model was run for 10 years in a climatological mode, and the last 10th year data are exploited for the following analyses.

Table 4.2. Biogeochemical model configurations

Parameter	Symbol	Value	Unit
Half-saturation for phytoplankton NO_3^- uptake	$K_{NO_3^-}$	1.5	mmol N m^{-3}
Half-saturation for phytoplankton NH_4^+ uptake	$K_{NH_4^+}$	0.5	mmol N m^{-3}
Phytoplankton ammonium inhibition parameter	$\emptyset$	1.5	$(mmol\ N)^{-1}$
Phytoplankton loss to sink rate	$\mu_{[Phyt]}$	0.01	d^{-1}
Phytoplankton mortality to detritus rate	$\mu_{[Phyt][Det]}$	0.072	d^{-1}
Zooplankton maximum growth rate	g_{max}	0.75	d^{-1}
Zooplankton assimilation efficiency	β	0.75	n.d.
Zooplankton half-saturation for ingestion	K_{Phyt}	1.0	d^{-1}
Zooplankton loss to sink	$\mu_{[Zoo]}$	0.025	d^{-1}
Zooplankton specific excretion rate	$\mu_{[Zoo][NH_4^+]}$	0.1	d^{-1}
Zooplankton mortality to detritus	$\mu_{[Zoo][Det]}$	0.025	d^{-1}
Detrital loss to sink rate	$\mu_{[Det]}$	0.02	d^{-1}
Detrital breakdown to NH_4^+ rate	$\mu_{[Det][NH_4^+]}$	0.03	d^{-1}

4.2 Surface Chlorophyll-a and eddy activity

Reproducibility of the hydrodynamic kernel of the present coupled ROMS-NPZD model has been extensively confirmed to show a good agreement in annually and seasonally averaged senses against satellite altimetry and sea surface temperature (SST) data, in situ cross-sectional density measurements, resultant 3D velocity fields including the Kuroshio, and eddy intensity (Uchiyama et al., 2018b). More importantly, the NPZD model was also validated with the climatological satellite Chl-a data to show overall agreement such as enhanced upper-ocean primary productivity enriched by the nutrient stream accompanied by the Kuroshio (Uchiyama et al., 2017; Nagai et al., 2019). Although this overly simplified nitrogen-based pelagic model is not perfect, Uchiyama et al. (2017) concluded that the present model performs reasonably well to diagnose the biological responses to eddy activities in the upper ocean around the Kuroshio. However, there are several subtle discrepancies between the model and observations, which are generally considered to play minor roles in the present study. For example, the primary production is slightly overestimated in the north of the Kuroshio path in the KE by the model as compared to the satellite observation, probably due to the lack of iron limitation mechanism (e.g., Fiechter et al., 2009; Moore et al., 2013), which is not taking into account in the present model. In addition, the Chl-a concentration near the coastal area is underestimated because the model ignores the land-derived nutrient input. It must be noted that we intentionally exclude the land-derived nutrient source because the primary aim of the present study is to understand oceanic eddy dynamics on vertical nutrient transport to sustain the upper-ocean productivity with avoiding terrestrial influences in the upper ocean.

Figure 4.2 shows the spatial distributions of the seasonally averaged surface Chl-a concentrations from winter (Dec.–Feb.) to fall (Sep.–Nov.). An obvious spring bloom (Mar.–May) occurs extensively on the northern side of the Kuroshio between Hokkaido Island (~144°E, 45°N) and the central Honshu Island (~140°E, 35°N) because of abundant nutrient supply from deeper layer to surface in the early spring (**Figure 4.2b**). By contrast, although the Chl-a concentration on the southern side of the Kuroshio is enhanced slightly, it is still lower than that on the northern side. A possible reason is that the nitrate-depleted subsurface mode water is predominant underneath the south of the Kuroshio (e.g., Nishikawa et al., 2013). The surface Chl-a concentration is the lowest in summer (Jun.–Aug.; **Figure 4.2c**), and then it generally increases in colder seasons from fall to winter (**Figure 4.2d and a**). Meanwhile, the Chl-a concentration is the highest in Japan Sea in winter as compared to other seasons (**Figure 4.2a**), which is inconsistent with the observations (e.g., Yoo and Kim, 2003; Yamada et al., 2004; Park et al., 2014) most likely for the lack of the land-derived nutrient input in the model. Nevertheless, the modeled seasonal variability of the surface productivity on the Pacific side is largely consistent with the MODIS/Aqua satellite data and the previous measurements (Sasai et al., 2007; Nagai et al., 2019). Qualitative evidence of importance of eddies to the seasonal

productivity is demonstrated in the lower panels of **Figure 4.2**, in which randomly sampled snapshots of relative vorticity normalized by the local Coriolis parameter at surface are exhibited for the four seasons in the enlarged area (shown in rectangular boxes in the upper panels) around the KR and KE regions. While intensive mesoscale vortices are significant particularly around the Kuroshio, submesoscale eddies are generated more evidently in colder seasons with relatively smaller spatial scales in the northern area (**Figure 4.2e and f**). On the contrary mesoscale eddies are more predominant in warm seasons (**Figure 4.2g and h**). This area is well known to be occupied by intensive submesoscale coherent structures in winter mainly due to the mixed-layer deepening and surface cooling (e.g., Kamidaira et al., 2018).

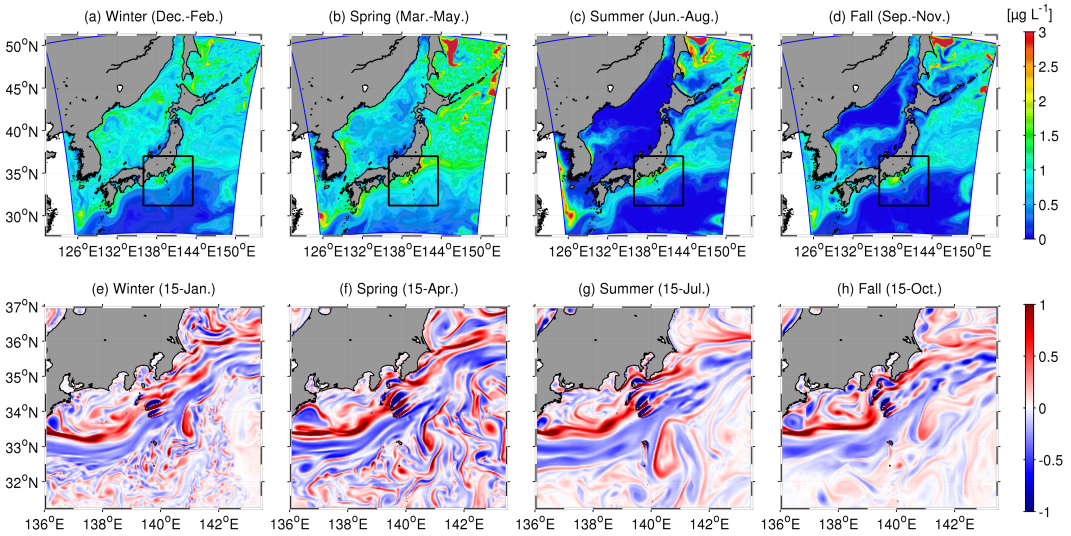

Figure 4.2. Upper panels: Seasonally averaged modeled surface chlorophyll-a (Chl-a) concentrations in four seasons. Note that we define four seasons as winter (December-February), spring (March-May), summer (June-August), and fall (September-November), respectively. Lower panels: Daily snapshots of relative vorticity normalized by the Coriolis parameter at the surface in four seasons.

4.3 Comparison between Kuroshio Region and Kuroshio Extension regions

4.3.1 Vertical structures and eddy-driven nitrate flux

The surface Chl-a in **Figure 4.2** shows noticeable difference of the spatial patterns between in the upstream (i.e., the KR) and in the downstream (i.e., the KE) regions along the Kuroshio. In the KR, shoreward confined high Chl-a is formed in comparison with that in the KE. To understand the mechanisms of such different responses of the primary production in the two regions, we investigate the vertical structures of the Kuroshio path and two locations ±0.8° away from the path. In the present model, we assume that the nitrogen source is distributed as nitrate in the subsurface beneath the mixed layer (Sec. 2). **Figure 4.3** shows Hovmöller diagrams of the nitrate concentration (left column), phytoplankton concentration (middle column) and vertical eddy-induced nitrate flux (right column) in the northern, central, and southern sides of the Kuroshio from the top to the bottom rows along 138°E (M1, **Figure 4.1b**) in the KR. The magenta lines indicate the corresponding mixed layer depth determined by the KPP boundary-layer sub-model. Note that the Kuroshio path is defined by the maxima of the surface current velocity. To examine the impacts of eddies on the vertical nitrate transport, the vertical nitrate flux F_V are evaluated by applying Reynolds decomposion of relevant variables into the mean and eddy components using the following equation:

$$F_V = Nw \approx \underbrace{\bar{N}\bar{w}}_{\text{mean}} + \underbrace{\overline{N'w'}}_{\text{eddy}}, \tag{4.9}$$

where w is the upward vertical velocity; N is nitrate concentration ($[NO_3^-]$); the overbar denotes an ensemble (time) averaging operator; and the prime indicates the fluctuating (eddy) component for the periods shorter than 90 days calculated with a Butterworth frequency filter. The upward transport is defined as positive.

As expected, intra-annual, seasonal variability is evident in the nitrate supply to surface and the mixed layer depth. The mixed layer deepens in colder seasons from December to April, along with enhanced nitrate supply to surface. This pattern is the most significant on the northern side of the path in the KR, where nitrate concentration is the highest near the surface (**Figure 4.3a**). As the upper bound of the subsurface nitrate source (e.g., intermediate concentration in cyan) is lowered in the southward direction from **Figure 4.3a** to **4.3c**, a meridional transition occurs with southward upper-ocean nitrate decrease. Although the upper bound is elevated at the northern location in warmer seasons from May to October, the surface nitrate concentration is as low (**Figure 4.3a**) as those at the central and southern locations where the warmer season upper bound is lowered (**Figure 4.3b, c**). Phytoplankton (viz., Chl-a concentrations) fluctuates quite sensitively in response to the nitrate concentration fluctuations in the mixed layer (**Figure 4.3d-f**). Chl-a is distributed much deeper in colder seasons than warmer seasons because of deep convective vertical mixing indicated by mixed layer deepening that promotes

upward entrainment of the subsurface nutrient-rich water to maintain high productivity.

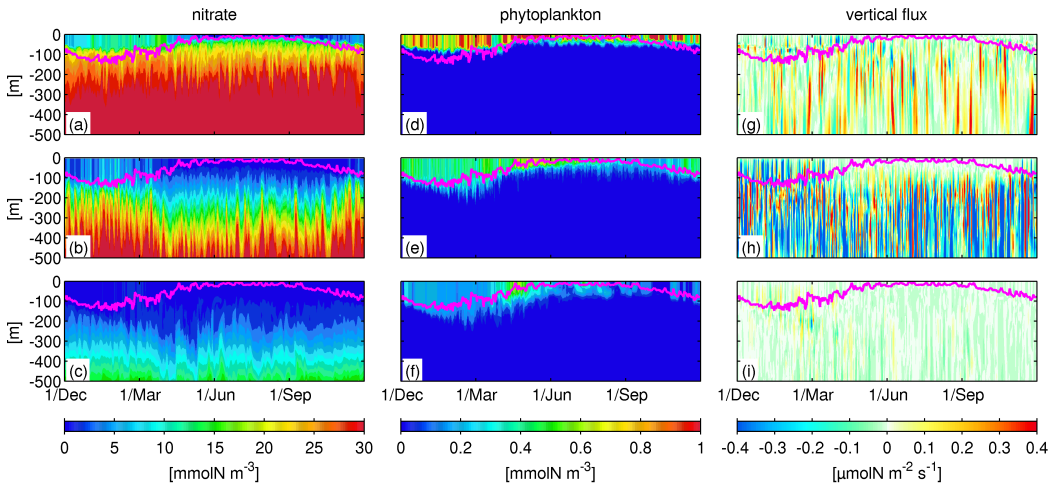

Figure 4.3. Hovmöller diagrams of the nitrate concentrations (left column), phytoplankton concentration (middle column), and vertical eddy-driven nitrate flux (right column) in the northern (top row), central (middle row) and southern (bottom row) locations along 138°E in the Kuroshio Region (KR, M1 as shown in **Figure 4.1**). The magenta lines are the corresponding mixed layer depth determined by the K-Profile Parameterization submodel in ROMS.

Figure 4.4 shows the same plots as **Figure 4.3**, but along 145°E (KE, N1 in **Figure 1a**) to represent the KE region. Similarly to the KR in **Figure 4.3**, the primary production occurs most actively on the northern side of the Kuroshio in particular in colder seasons with a southward meridional phytoplankton downgradient (**Figure 4.4d-f**), where the nitrate upper bound descends evidently (**Figure 4.4a-b**) even at the same distances from the Kuroshio path as compared to those in the KR. The spring blooms occur along the Kuroshio path and its south side from April to May (**Figure 4.3e-f**), while at the northern location Chl-a concentrations in colder seasons occasionally as high as those in spring (**Figure 4.3d**). The vertical eddy-driven nitrate transport is overall positive (upward) in the southern region. However, the downward fluxes appear in the mixed layer in winter along the Kuroshio path and its north side (**Figure 4.3g and h**), suppressing the upper-ocean primary production associated with eddy influences.

Chl-a within and around the mixed layer appears to be higher in the KE with more reddish color from April to June (**Figure 4.4e-f**) than that in the KR (**Figure 4.3e-f**), except for the northern location where the nitrate concentration below the mixed layer is much higher in the KR (**Figure 4.3a**). The spring bloom is also more remarkable in the KE than that in the KR. The eddy-induced flux shows an upwelling tendency in the KE particularly in colder seasons rather than warmer seasons in the northern location (**Figure 4.4g**). As the sign of eddy nitrate flux fluctuates intensively in time, we will look into time-averaged spatial distributions later. These results demonstrate that nutrient fluxes from the nutrient-rich subsurface layer to the nutrient-exhausted surface layer are substantial for maintaining primary production near the surface. It should be noted that a high correlation (a correlation coefficient of ~0.62) between the nitrate concentrations and vertical eddy nitrate fluxes in both regions demonstrates that the nitrate supply to surface layer is strongly influenced by the mesoscale and submesoscale eddies. Such a high correlation is more pronounced in colder season particularly on the north side of the Kuroshio path (**Figures 4.3a** and **4.4a**).

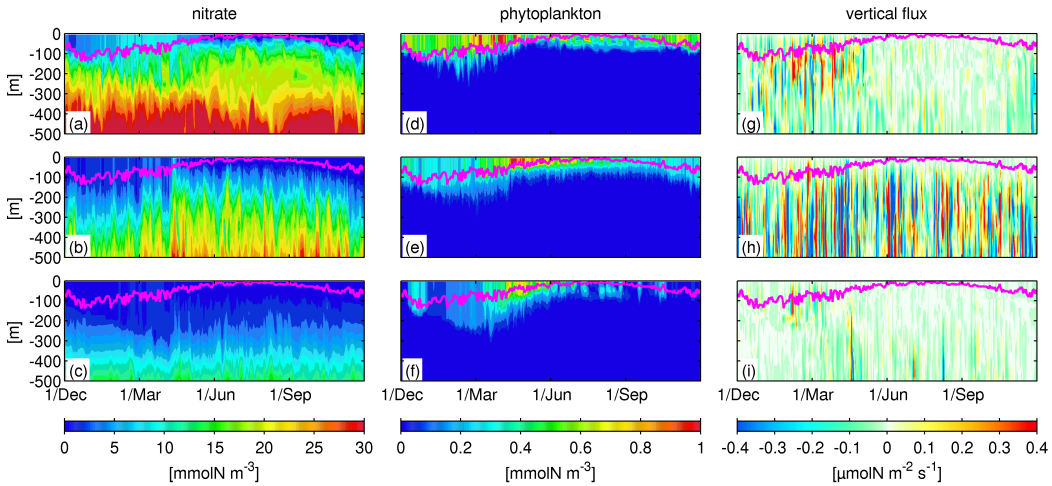

Figure 4.4. Same as **Figure 4.3**, but for 145°E in the Kuroshio Extension (KE, N1 as shown in **Figure 4.1**).

The other biological components (zooplankton, ammonium and detritus) are briefly described with supplemental figures (**Figures S4.1** and **S4.2**). Increase of zooplankton concentration on the north side of the Kuroshio is delayed for a month or two (**Figures S4.1a**, **and S4.2a**), while zooplankton concentration is fairly low along the Kuroshio path and its south side (**Figures S4.1b-c and S4.2b-c**). During the spring bloom, the nitrate is mainly consumed by phytoplankton, which is grazed by zooplankton subsequently. The nitrogen is mostly stored in phytoplankton and zooplankton compartments in the KR and KE. Therefore, the nitrate concentration decreases significantly, showing an obvious negative correlation between plankton and nitrate concentrations. The phytoplankton and zooplankton death further enriches detritus sinking down to ~100 m from the base of the mixed layer (**Figures S4.1d-f and S4.2d-f**). Hence the detritus concentration is commonly distributed relatively deeper in colder seasons than warmer seasons due again to the vertical mixing enhanced in colder seasons. The detritus decomposition and zooplankton death concurrently contribute to the improvement of ammonium. Hence, inorganic nitrogen deduced from detritus is the major source of ammonium in the deeper region below the mixed layer, especially on the north side. Meanwhile, uptake of both nitrate and ammonium is due to phytoplankton, leading to depletion of ammonium in the mixed layer, in particular along the Kuroshio path and on the southern side. The ammonium and detritus concentrations are higher in the KE than the KR. The largest difference in the two regions is the subsurface ammonium on the north side, which is distributed down to 300 m depth in the KE while it exists down to ~100 m below the mixed layer base (**Figure S4.2g**). In addition, high frequency fluctuations associated with eddy-driven nutrient transport are significant in all these compartments, showing substantial eddy influences on the biogeochemistry over the depth of several hundred meters from the surface.

4.3.2 Averaged horizontal structures of vertical eddy-induced nitrate flux

In the upper-ocean, the transient (eddy) component of the vertical nitrate flux dominates over the mean flux as we mentioned earlier. Therefore, we compute the vertically integrated eddy-induced nitrate flux F_v (Eq. 4.9) from the surface down to 300 m depth to examine its seasonal patterns of the horizontal distribution. The upper panels of **Figure 4.5** show the spatial distribution of vertically integrated and seasonally averaged F_v for winter and summer, while the lower panels are their enlarged views of the KR shown by the blue boxes in the upper panel. Apparently, the mean eddy-induced nitrate flux is generally large in magnitude around the Kuroshio path with several sign changes occurring as the Kuroshio flows northeastward in both seasons. The downward (bluish colors) and upward (reddish colors) fluxes alternately occur along the Kuroshio path with overall downward (upward) dominance in the KR (KE). Coastline topographies are also responsible for magnifying the eddy flux to promote complexity of the spatial distribution. Particularly the Enshunada Sea located in the north of the Kuroshio in 136°E-140°E is characterized by an obvious downward eddy flux in winter (**Figure 4.5a**, **c**), but by an overall positive (upward) flux in summer (**Figure 4.5b, d**).

Seasonal differences of vertical eddy-driven nitrate flux are also manifested. The magnitude and extent of influences are largely increased (decreased) in winter (summer) when the vertical mixing is stronger (weaker). Focusing on the differences in the KR and KE regions, we notice that the gross trend of the eddy nitrate flux is negative (downward) in the KR particularly in Enshunada Sea in winter that competes with the coastal upwelling nitrate transport from the nutrient-rich subsurface water. It should be mentioned that the spatially averaged eddy flux in the KR is dominated by downward flux except for summer because of intensive subsurface downward flux underneath the Kuroshio axis as illustrated by the prominent negative flux in **Figure 4.5** (see also Uchiyama et al., 2017). In contrast, the eddy nitrate flux is broadly positive (upward) in the KE (**Figure 4.5a**), more evidently in winter, while it is negligibly small in the north of the Kuroshio in summer (**Figure 4.5b**). The sign change occurs noticeably around the Izu-Ogasawara Ridge, where the negative downward eddy flux in the upstream region (<139°E) turns out to be positive over the ridge (139°E–140°E), and then reverts back to negative in the downstream (140°E–142°E) before reaching the KE particularly in winter.

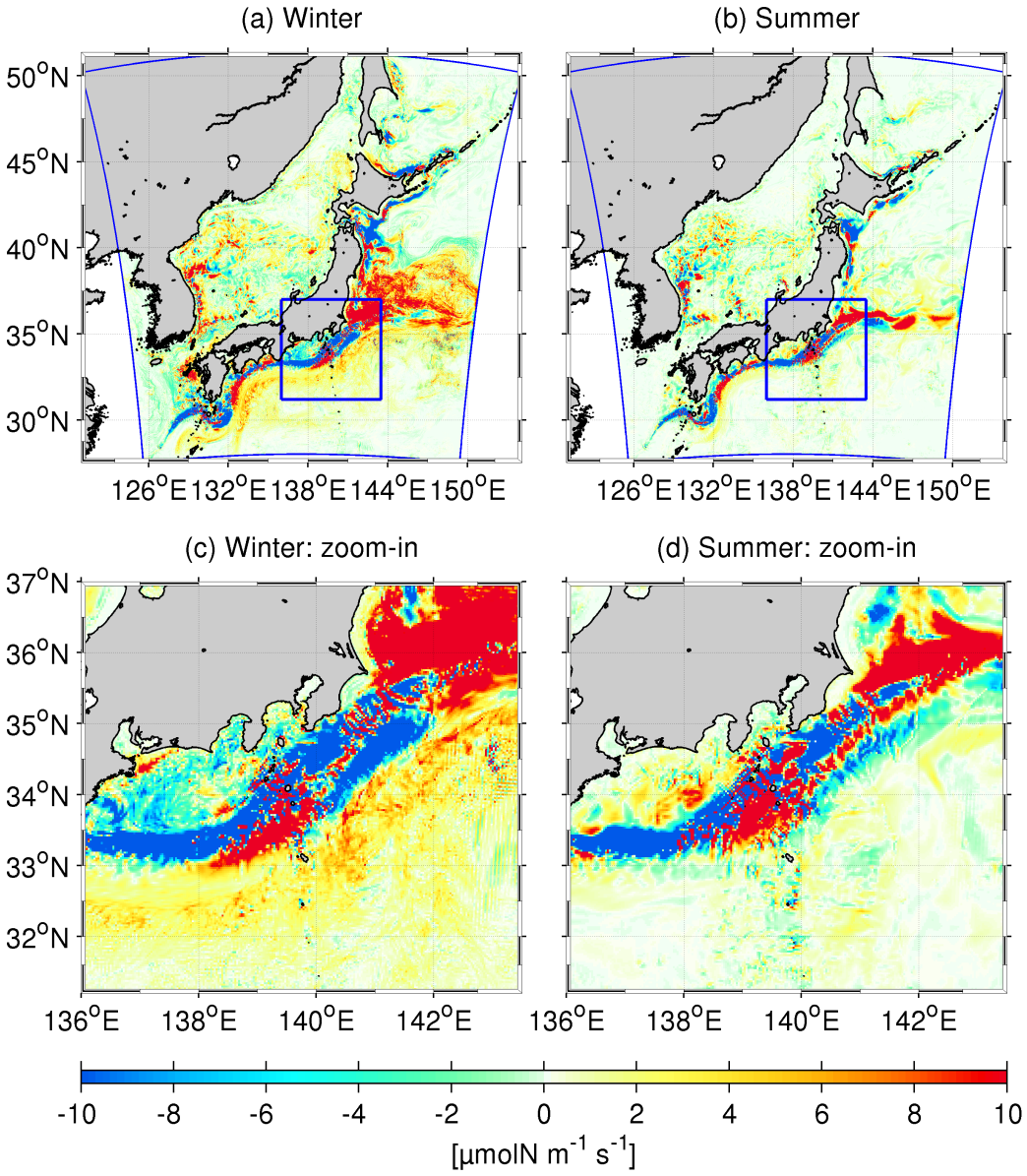

Figure 4.5. Upper panels: Spatial distribution of vertically integrated and seasonal averaged eddy-induced nitrate flux down to 300 m depth in winter and summer. Lower panels: Enlarged plots of those shown in the upper panels for the Kuroshio Region (KR) shown by the blue boxes in the upper panels.

4.3.3 Eddy generation mechanism

To investigate a generation mechanism of eddies, which play a central role in exciting eddy nitrate fluxes, we assess the energy conversion terms relevant to eddy kinetic energy (EKE). We focus on K_mK_e, the conversion of mean kinetic energy to eddy kinetic energy due to the shear instability, and P_eK_e, the conversion of eddy potential energy to eddy kinetic energy due to the baroclinic instability, as defined by the following equations.

$$\mathrm{K_mK_e} = -\left(\overline{\mathrm{u'u'}}\,\frac{\partial \bar{\mathrm{u}}}{\partial \mathrm{x}} + \overline{\mathrm{u'v'}}\,\frac{\partial \bar{\mathrm{u}}}{\partial \mathrm{y}} + \overline{\mathrm{u'w'}}\,\frac{\partial \bar{\mathrm{u}}}{\partial \mathrm{z}} + \overline{\mathrm{v'u'}}\,\frac{\partial \bar{\mathrm{v}}}{\partial \mathrm{x}} + \overline{\mathrm{v'v'}}\,\frac{\partial \bar{\mathrm{v}}}{\partial \mathrm{y}} + \overline{\mathrm{v'w'}}\,\frac{\partial \bar{\mathrm{v}}}{\partial \mathrm{z}}\right), \quad (4.10)$$

$$\mathrm{P_eK_e} = -\frac{\mathrm{g}}{\rho_0}\overline{\rho'\mathrm{w'}}, \quad (4.11)$$

where (x, y, z) is the horizontal and vertical coordinates; u and v are eastward and northward horizontal velocities; ρ is the density of sea water; $\rho_0 = 1027.5$ kgm^{-3} is the reference density; and g is the gravitational acceleration. As K_mK_e and P_eK_e are dominant source terms in the EKE conservation equation, EKE is increased (decreased) to let the mean flow be unstable (stable) when K_mK_e and P_eK_e are positive (negative).

Figure 4.6 is the same set of plots as **Figure 4.5**, but shows the horizontal distributions of vertically integrated P_eK_e down to 300 m depth in two seasons. Positive P_eK_e is provoked broadly along the Kuroshio path in winter (**Figure 4.6a**, **c**). This result is consistent with the previous studies (e.g., Sasaki et al., 2014; Uchiyama et al., 2017; Kamidaira et al., 2018), which suggested that surface cooling and associated mixed layer deepening give rise to baroclinic instability, resulting in generation of vigorous mesoscale and submesoscale eddies much more extensively in colder seasons. The enhanced vertical eddy-driven nitrate flux in winter shown in **Figure 4.5a**, **c** is generally collocated with the areas where the large positive P_eK_e is distributed. In contrast, P_eK_e decreases to narrow to the Kuroshio path and to be largely negative in summer (**Figure 4.6b**, **d**), resulting in the reduction of eddy intensity and thus the vertical eddy nitrate flux is reduced (**Figure 4.5b**, **d**). In the KR and KE regions, negative P_eK_e appears near the Izu-Ogasawara Ridge in both seasons. This ridge has a unique topographic feature consisting of many islands and submerged seamounts with depths shallower than 1000 m. Therefore, the ridge is considered to interact with the Kuroshio that influences the subsurface water down to 1000 m depth in the KR, sometime called island mass effects. Further analyses on the ridge influences will be provided in the subsequent section. It must be noted that the horizontal distribution of K_mK_e is more or less similar to the winter P_eK_e distribution with almost no clear seasonal variability, and is not shown here accordingly.

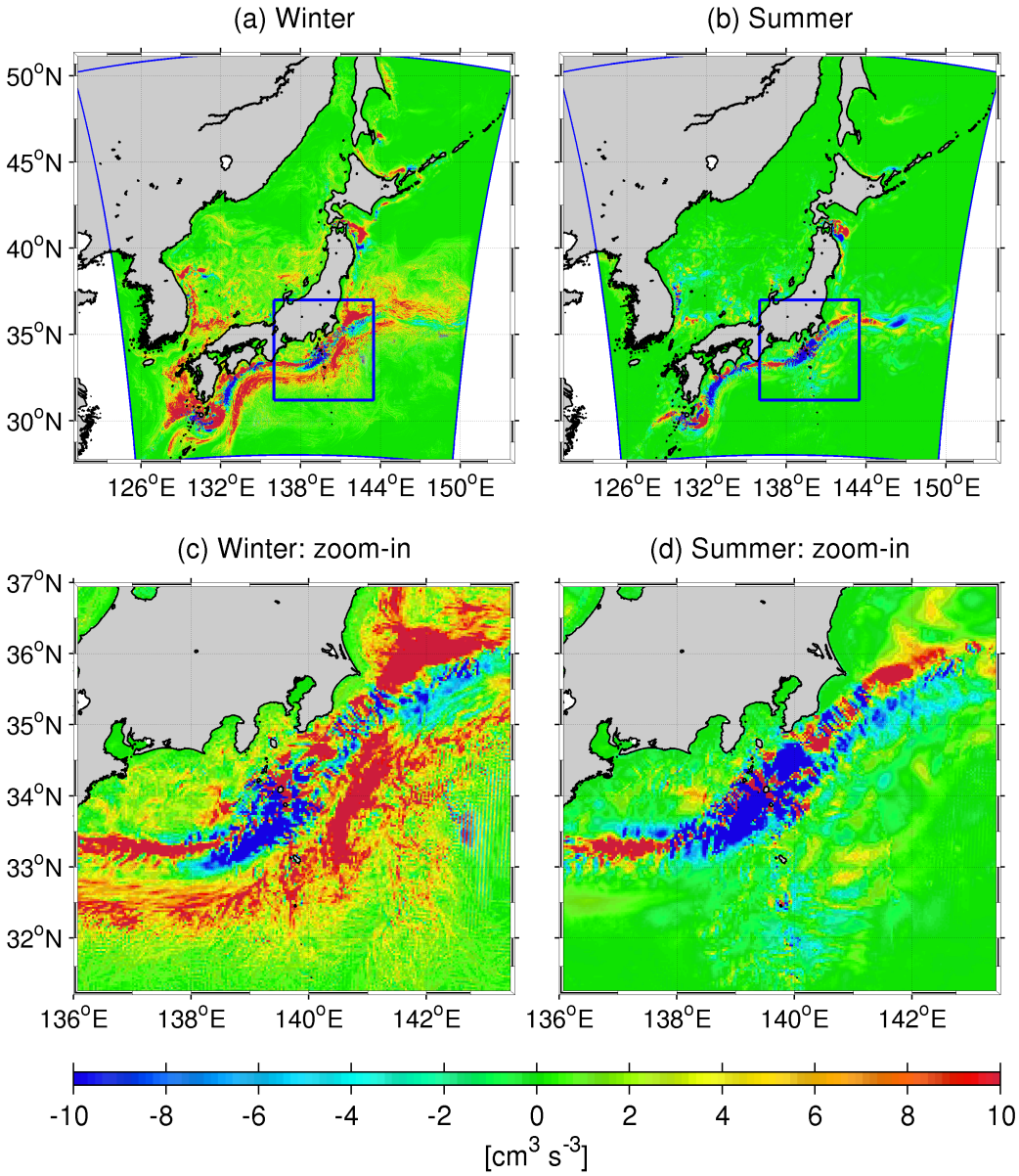

Figure 4.6. Same as **Figure 4.5**, but for the baroclinic conversion rate, P_eK_e.

To highlight the differences between the two EKE source terms in the KR and KE regions, the cross-sectional plots of the seasonally averaged K_mK_e (upper panels) and P_eK_e (lower panels) in winter along 138°E (KR; M1 in **Figure 4.1**) and 145°E (KE; N1 in **Figure 4.1**) are shown in **Figure 4.7**. The associated mixed layer depth is depicted by magenta lines. The black dotted contours are eastward velocity normal to the cross-sections, representing the Kuroshio main body. In the KR, eddies are generated by a combination of the positive K_mK_e and P_eK_e around the Kuroshio path in the upper ocean, while P_eK_e prevails over K_mK_e within the mixed layer to stretch down to ~32.1°N on the southern side of the path, as well as up to the coastline at ~34.6°N to the north to a lesser degree (**Figure 4.7a**, **b**). Therefore, shear instability (viz., positive K_mK_e) due to the energetic Kuroshio mainly promotes mesoscale eddies near the path that leads to negative downward eddy-driven nitrate flux in the KR, i.e., the downstream region of the ridge, in winter (**Figure 4.5a**, **c**). Baroclinic instability (viz., positive P_eK_e) in winter also is of great importance to the broadly distributed high EKE off the path, resulting in the downward F_v near the coast to the north and the upward F_v to the south in the mixed layer (**Figure 4.5c**).

On the other hand, in the KE region, the positive K_mK_e and P_eK_e (**Figure 4.7c**, **d**) jointly give rise to upward eddy nitrate flux (**Figure 4.5a**) in the upper ocean in winter along the N1 transect, maintaining the near surface primary productivity. Similarly to the KR, shear instability occurs merely near the Kuroshio, whereas baroclinic instability extensively takes place for the long meridional stretch more evidently on the north side of the path to promote the increased upward eddy flux even away from the path. This meridional asymmetry of P_eK_e distributions is a key to the more active primary production occurred broadly in the KE around the Kuroshio path and its northern region in winter (**Figure 4.5a**) even though the upper bound of the subsurface nitrate source is located deeper in the KE (**Figure 4.4**) than in the KR (**Figure 4.3**).

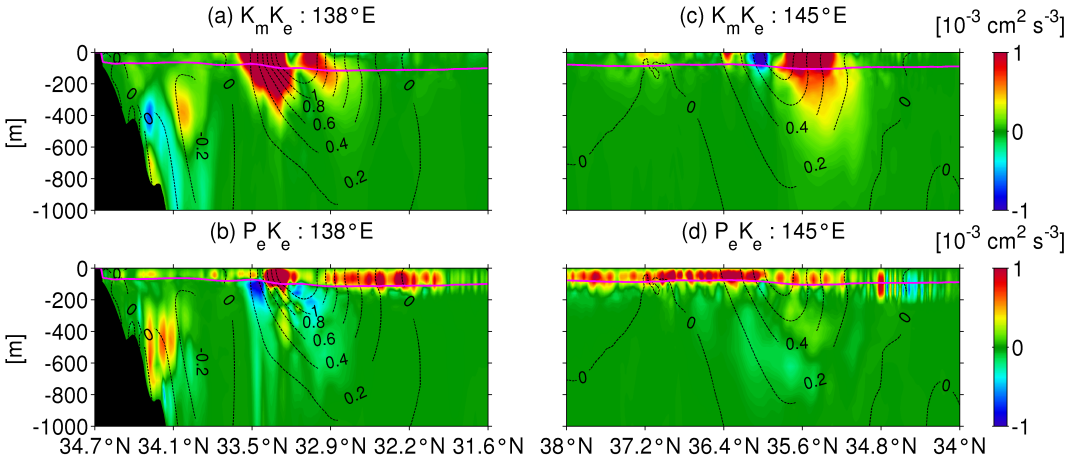

Figure 4.7. Cross-sectional plots of the seasonally averaged barotropic conversion rate, K_mK_e (top row), and baroclinic conversion rate, P_eK_e (bottom row), along 138°E (M1) in the KR (left column) and 145°E (N1) in the KE (right column) in winter. The magenta lines denote the mixed-layer depth computed by KPP model. The black dotted contours show eastward velocity perpendicular to the transects, denoting approximate positions of the Kuroshio.

Figure 4.8 shows the same plots as **Figure 4.7**, but in summer. As compared to winter, the surface mixed layer becomes thinner in summer, clearly reducing baroclinic instability as P_eK_e is merely significant near the Kuroshio path in both of the KR and KE regions. The summer K_mK_e is similarly distributed to that in winter, without almost no obvious seasonal variability as mentioned earlier in this subsection for the horizontal distribution of K_mK_e. In the KR, positive P_eK_e (**Figure 4.8b**) promotes the eddy-driven downward nitrate flux (**Figure 4.5b**) through baroclinic instability only near the Kuroshio path in summer, although positive P_eK_e in the mixed layer in winter (**Figure 4.7b**) is attributed to much wider appearance of non-trivial eddy fluxes F_v (**Figure 4.5b**). Likewise, in the KE, P_eK_e is considerably diminished to be negligible, while positive K_mK_e arisen near the path solely plays a role in maintaining modest eddy nitrate flux over there.

In summary, baroclinic instability is the most important factor for seasonal variability in eddy generation. It vitally provokes the downward and upward eddy-induced nitrate flux in the upper ocean in the KR and KE in winter, while its influence becomes much weaker in both regions in summer.

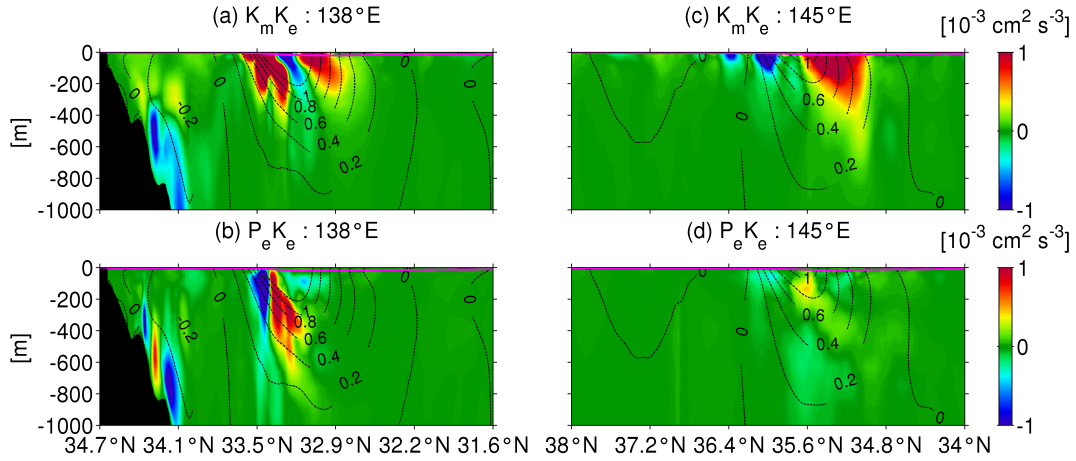

Figure 4.8. Same as **Figure 4.7**, but in summer.

4.3.4 Importance of eddy-driven nitrate flux in the upper ocean

Some previous studies have argued the importance of the vertical diffusive nitrate flux and thus the evaluation of the magnitude of *in situ* vertical eddy diffusivity has been of great interest in the study area. For example, Kaneko et al (2013) reported the intensive vertical diffusive nitrate flux on the north side of the Kuroshio path, which is also true in our winter result. Observational evidence of strong vertical mixing due to unique topography, such as straits and ridges, has also been discussed (e.g. Tsutsumi et al., 2017; Nagai et al., 2017), which further promotes the vertical diffusive nitrate flux (Tanaka et al., 2019). Therefore, we compared relative contributions of the three prevailing vertical nitrate fluxes, n.b., $\overline{N'w'}$, mean advective flux $\bar{N}\bar{w}$, and diffusive flux $-K_v\partial_z\bar{N}$, where K_v is the KPP-derived vertical eddy diffusivity, to the vertical nitrate transport in the upper ocean.

Table 4.3 summarizes $\bar{N}\bar{w}$, $-K_v\partial_z\bar{N}$ and $\overline{N'w'}$, vertically integrated from surface to 300 m depth with seasonal and spatial averaging operations over 20 km ×20 km square domains centered at the sampling stations along the M1 and N1 transects (see **Figure 4.1b**). Overall, the mean advective flux is minor in the upper ocean as compared to the eddy and diffusive fluxes, whereas it plays a more substantial role in deeper region, where the nitrate concentration is high, than the other two fluxes (not shown). Meanwhile, the eddy nitrate flux, $\overline{N'w'}$, is comparable to or even predominant over the diffusive flux, particularly along the Kuroshio path (M1b and N1b) both in winter and summer. More importantly, the diffusive flux is always positive (viz., upward) because the nitrate is mostly stored in the subsurface reservoir to yield $\partial_z\bar{N} < 0$. Thus the positive (negative) eddy flux can be viewed to promote (suppress) the upward diffusive nitrate supply to the upper ocean. This result solidly demonstrates that eddy-induced nitrate flux plays a quite important role in the vertical nitrate transport, which is consistent with previous studies in the KR and KE regions (e.g., Kimura et al., 1997; Kimura et al., 2000; Kasai et al., 2002). Therefore, we pay most of our attention to the influences of mesoscale and submesoscale eddies on the nitrate supply to the upper-ocean in the present study.

Table 4.3. Mean vertical nitrate fluxes, $\overline{N}\overline{w}$, $-K_v\partial_z\overline{N}$ and $\overline{N'w'}$, integrated vertically down to 300 m depth near M1a-c in KR and N1a-c in KE (see **Figure 4.1b** for the locations). The unit is μmol N m^{-1} s^{-1} and upward fluxes are defined as positive. See also text for detail.

		Winter			Summer		
		Mean	Eddy	Diffusive	Mean	Eddy	Diffusive
KR	M1a	4.22	-2.53	60.14	-8.41	4.49	3.12
	M1b	2.06	-55.74	67.50	-2.32	-35.76	1.51
	M1c	-0.35	3.18	8.57	0.11	0.26	0.51
KE	N1a	8.98	11.56	36.22	-2.73	0.82	2.25
	N1b	2.60	7.68	14.19	4.76	-2.74	1.15
	N1c	-0.61	2.62	10.93	0.10	0.14	0.26

4.4 Effects of the oceanic ridge in the Kuroshio Region: island mass effects

4.4.1 Change in biogeochemistry around the oceanic ridge

The Kuroshio flows over an oceanic ridge (i.e., Izu-Ogasawara Ridge; **Figure 1b**) that is located at the south coast of Japan in the KR, meridionally stretching along 139–140°E. This unique topography is considered to have remarkable influences on the Kuroshio and eddies, further affecting the associate biogeochemical responses. To examine changes in the biogeochemistry due to the ridge, we set four cross-sections along 138.9°E, 139.7°E, 140.5°E, and 141.4°E in both upstream and downstream of the ridge (M2-5, **Figure 4.1b**).

Figure 4.9 illustrates Hovmöller diagrams of nitrate concentrations on the time-averaged Kuroshio main axis from west to east and the two meridionally remote stations ±0.8° away from the axis. The sampled stations represented by black dots in **Figure 4.1b** are selected on the M2-5 transects, respectively. Sets of the vertically aligned three panels, e.g., **Figure 4.9a-c** (for M2), are similar plots to **Figure 4.3a-c** (for M1). Note that the depths at north stations along M3 and M4 are ~300 m, and thus the data below that depth are null. In addition, the northern station along M4 is so close to the shore with a depth of ~100 m that it is substituted by a slightly offshore station at +0.4° (not +0.8°) away from the Kuroshio path. **Figures 4.10** and **4.11** are the same sets of the plots as **Figure 4.9**, but for phytoplankton concentrations (**Figure 4.10**) and upward positive vertical eddy nitrate fluxes F_v (**Figure 4.11**).

General structure and variability are similar to those along M1 discussed in Section 4.3.1. For instance, the mixed layer deepens in colder seasons to promote the nitrate supply to the surface layer from the subsurface at all the stations expect for the northern station along M5 (**Figure 4.9M5a**), where the nitrate varies intermittently with a longer fluctuation period presumably according to reduced topographic constraint to be a more freely fluctuating Kuroshio jet. Chl-a concentrations are also highest in the northern stations with prominent spring bloom in Apr.–Jun. (**Figure 4.10M5a**), consistent with the increased nitrate distributions with a lag of a few months. A strong eddy nitrate flux occurs in the mixed layer in the colder season (Dec.–Apr.), followed by enhanced flux mainly below the mixed layer but extended to the surface layer in the subsequent spring (Apr.–Jun.). Therefore, the increased vertical mixing due to surface cooling in winter promotes the upper-ocean eddy nitrate fluxes to bring the subsurface nitrate to the surface layer, which preconditions the subsequent Chl-a bloom under the optimal radiation condition in spring. During the spring bloom, the near-surface nitrate is consumed by phytoplankton to be depleted.

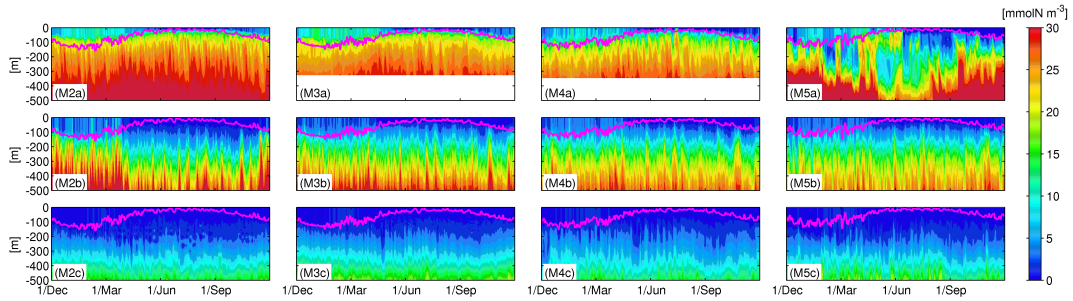

Figure 4.9. Hovmöller diagrams of the nitrate concentrations in the northern (top row), central (middle row) and southern (bottom row) locations represented by black dots **Figure 4.1b** along M2-5 in the KR. The magenta lines denote the corresponding mixed layer depth.

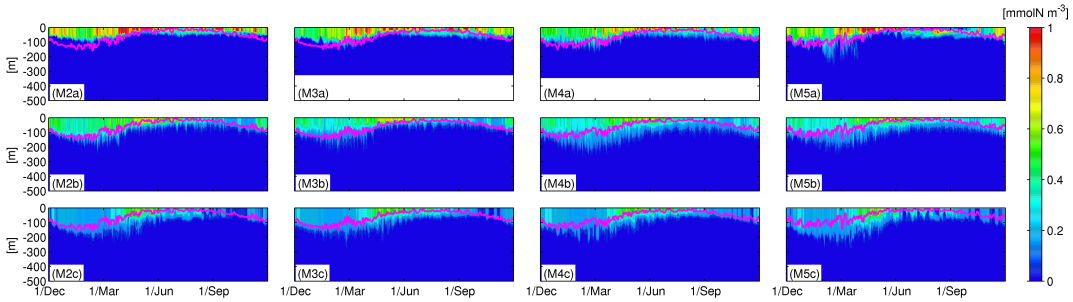

Figure 4.10. Same as **Figure 4.9**, but for the phytoplankton concentrations.

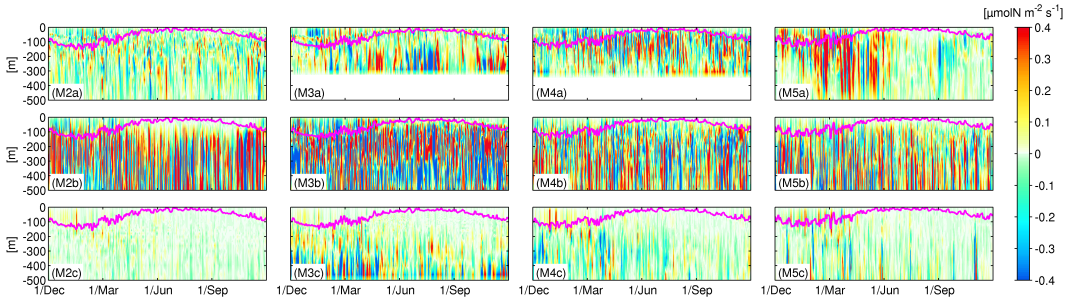

Figure 4.11. Same as **Figure 4.9**, but for the vertical eddy-driven nitrate fluxes.

The ridge area (M3) is found to act to alter the nitrate distribution noticeably, where the near-surface nitrate is moderately higher in the downstream than that in the upstream region, especially at the northern stations (**Figure 4.9M2a-M5a**). Phytoplankton distributes shallower in the upstream region, while it can go down below the mixed layer with the depth of ~200m in the downstream region. By contrast, at the stations on the Kuroshio (**Figure 4.9M2b-M5b**), near-surface nitrate is higher in the upstream region while the subsurface nitrate is lower, leading to steeper vertical nitrate gradients in the upstream region than the downstream. Such an increase of the vertically stretched nitrate gradation in the downstream region is also visible at the southern stations (**Figure 4.9M2c**-**M5c**). The upper-ocean Chl-a is distributed consistently with the vertically elongated nitrate, leading to increased thickness of the high Chl-a water towards the downstream region at the central and southern stations. Active primary production appears in spring along the eastern-most transect (**Figure 4.10M5a-M5c**), although the nitrate concentration is relatively lower there (**Figure 4.9M5a-M5c**), again perhaps due to a nature of the Kuroshio jet that could promote abrupt vertical and horizontal nitrate transport to enhance the production of phytoplankton. The eddy-driven nitrate flux is the strongest along the main axis (**Figure 4.11M2b**-**M5b**) with considerably vertically elongated structures demonstrating predominance of quasi-geostrophic mesoscale eddies, especially around the oceanic ridge (**Figure 4.11M3b**). In turn, enhanced eddy fluxes in the mixed layer in colder seasons indicate emergence of susbmesoscale eddies, which can marginally be resolved in the present ROMS model with a lateral grid spacing of 3 km (see **Figure 4.2**). Hence influences of mesoscale eddies are the most apparent on the Kuroshio path, near the ridge, and the downstream region on the north side of the path, where the vertical Chl-a gradient is less obvious. For example, in winter and spring, the vertical eddy flux is larger at the northern station in the downstream (**Figure 4.11M5a**) than that in the upstream (e.g., **Figure 4.11M2a**) according to both of mesoscale and submesoscale eddies that sustain the local upwelling of the nitrate, resulting in surface-concentrated high nitrate (**Figure 4.9M5a**) and subsequent active spring bloom over there (**Figure 4.10M5a**).

4.4.2 Change in dynamics around the oceanic ridge

To investigate a possible mechanism responsible for spatial changes in the vertical nitrate transport in the KR, we examine the cross-sectional distributions of the seasonally averaged values of several variables in winter (Dec.–Feb.) along the three transects (M1, M2, and M5, **Figure 4.1b**) in **Figure 4.12** (More detailed spatial structures are shown in **Figure S4.3**). The displayed variables are EKE ($= \frac{1}{2}(\overline{u'^2} + \overline{v'^2})$, colors) and eastward horizontal velocity normal to the transects (white contours) in the upper panel, while nitrate concentrations (colors) and potential density □□ (black contours) are shown in the lower panels. The magenta lines are the seasonally averaged mixed-layer depth estimated by the KPP model. The Kuroshio main body is inclined to extend southward down to ~800 m depth. It is shaped by topographic influences of the ridge near M3 in **Figure 4.12c**. EKE peaks near the surface and slightly northward of the maximum velocity of the Kuroshio in conjunction with the maximum horizontal velocity shear with magnified complexity exhibited by two EKE peaks around the ridge at ~34.4ºN and ~33.7ºN (**Figure 4.12c**). Likewise, nitrate concentration and potential density are also inclined southward with elevated values near the coast to provoke northward upwelling of subsurface nitrate and potential energy from the base of the Kuroshio main body to the coast. Mixed layer depth is consistently shallower on the shore side than the offshore. Near surface nitrate is higher in the upstream region, whereas elevated nitrate does not reach the coast along M5 (**Figure 4.12f**). The concentrated EKE peak along M1 spreads meridionally in the upstream, while it is decreased and distributed not only near the surface but also at depth in the downstream along M5. A simple, but plausible description of dynamical effects of the ridge on the Kuroshio and associated eddy activity is a squashing by islands and submerged seamounts as illustrated by **Figure 4.12c and d**, which spontaneously accelerates and occasionally bifurcates the Kuroshio, amplifies the lateral shear, and promotes mesoscale eddies around the topographies even at depth. Such enhanced mesoscale eddies shed by the ridge make vertical and horizontal mixing be more energetic to induce vertically stretched intensive eddy flux as shown in **Figure 4.11M3c**. After passing over the ridge, the squashed Kuroshio is relaxed to expand laterally in the downstream, resulting in deceleration of the Kuroshio main body and reduced eddying fluctuations spreading over in wider and deeper areas.

It is worth mentioning that the seasonal variability in these cross-sectional structures is found to be insignificant, except for a minor meridional shift of the Kuroshio path up to ~0.4º and a shallower mixed layer particularly in summer, as supplemented in **Figure S4.4**. As we have seen in **Figures 4.2** and **4.11**, the deepened mixed layer is accompanied by energetic submesoscale activities occurred mostly within the mixed layer in colder seasons, which are attributed to additional near-surface eddy nitrate fluxes that promote upward nutrient supply through enhanced vertical mixing. These submesoscale eddies are basically provoked by baroclinic and mixed layer instabilities caused by

surface cooling that subtracts Ertel potential vorticity to be negative and preconditions symmetric instability in the upper ocean (Thomas and Lee, 2005; Thomas and Taylor, 2010; Kamidaira et al., 2018; Nagai et al., 2019), unrelated to the ridge topographies.

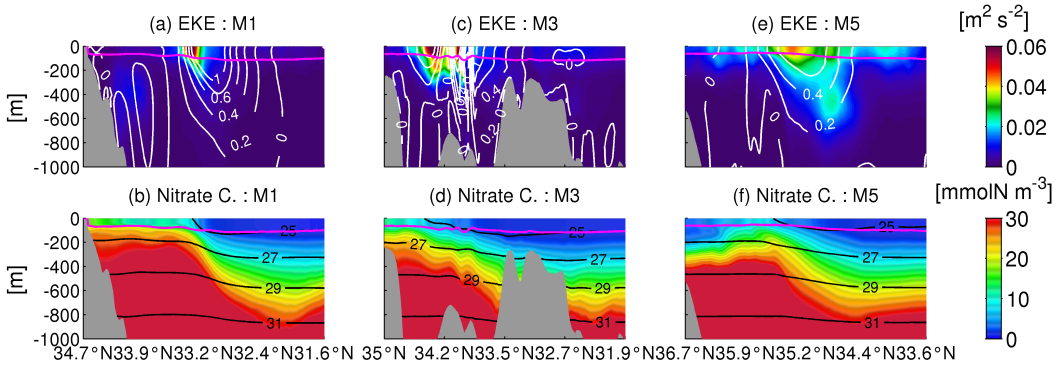

Figure 4.12. Cross-sectional plots of the seasonally averaged EKE (upper) and nitrate concentrations (lower) along the transects M1, M3, and M5 in winter (colors). Contours are eastern velocity [m/s] normal to the transects (upper) and potential density σ_θ [kg/m^3] (lower). The magenta lines are the seasonally averaged mixed-layer depths.

4.4.3 Eddy generation by the oceanic ridge

So far we have understood that spontaneous generation of mesoscale eddies by the Kuroshio shear and submesoscale eddies by surface cooling are the two substantial elements that affect eddy nitrate fluxes responsible for sustaining the primary production in the KR and KE regions. An additional key mechanism is the topographically generated mesoscale variability due to the ridge. Therefore, we next examine impacts of the local topography on the eddy generation by decomposing the barotropic conversion rate K_mK_e into horizontal and vertical components, as well as the baroclinic conversion rate P_eK_e along the five transects (M1–M5) in winter as shown in **Figure 4.13** (More details are shown in **Figure S4.5**). Consistent with the mean variables in **Figure 4.12**, an apparent spatial asymmetry in the conversion rates is observed between the upstream and downstream regions with respect to the ridge (M3; **Figure 4.13d-f**) as a pivot. In the upstream region, the positive horizontal K_mK_e and P_eK_e due to horizontal shear instability and baroclinic instability that concurrently induce eddy-driven nitrate flux near the Kuroshio. Positive P_eK_e is provoked in the upper ocean due to submesoscale eddies, in particular near and on the south side of the path, with significant amplification in the downstream region, where the near-surfacec P_eK_e is intensified broadly to extend on the north side of the Kuroshio. The vertical K_mK_e is largely centered on the path and near the topography, but is mostly negative or weak (notice the different scales), indicating that the horizontal shear instability dominates over the vertical shear instability. All the three conversion rates are significantly energized along M3 (139.7^{o}E) located around the ridge. When the Kuroshio passes over the ridge, it is squashed to enhance the horizontal velocity shear and subsequent eddy shedding mostly at mesoscale, except for the upper ocean where baroclinic submesoscale instability takes over shear instability, as anticipated in the preceding subsection. Moreover, an interaction between the ridge topography and the Kuroshio front at depth triggers pronounced baroclinic instability below the mixed layer along M3 (**Figure 4.13f**), leading to continuous subsurface destabilizing effects in the downstream (**Figure 4.13i**) with increased subsurface EKE (**Figure 4.12e**). Therefore, the deeper ocean is influenced by the combination of the horizontal shear instability and baroclinic instability, provoking the significant mesoscale eddy-driven nitrate transport in the downstream (**Figure 4.11M4b** and **M5b**), in particular on the northern side of the path (**Figure 4.11M4a** and **M5a**).

We should mention about the conversion rate distributions in warmer seasons (not shown). Similar to the mean structures discussed in Section 4.4.2, the surface mixed layer becomes thinner to result in considerable weakening of the near-surface submesoscale baroclinic instability. Besides the modest northward shift of the Kuroshio path that ends up with the northward shift of the subsurface peak location of P_eK_e along M2, the overall patterns of the three conversion rates are more or less the same as those for winter shown in **Figure 4.13.** However, the subsurface horizontal K_mK_e and P_eK_e are less significant or even negative (for P_eK_e, *i.e.*, stabilizing effects) in the downstream region particularly

along M5 in warmer seasons. Thus the eddy fluxes are weakened as shown in **Figure 4.11M5a-c**. Consequently, warmer seasons are characterized by the modest northward shift of the Kuroshio by ~0.4º in the present climatological model results that subtly affects changes of the conversion rates, whereas the interaction between the Kuroshio and the ridge topography is crucial to alter eddy intensity in the downstream region. In turn, the warmed upper ocean and increased incoming surface heat and radiation fluxes greatly suppress the near-surface submesoscale fluctuations, which turns out to be the reduced vertical mixing, eddy nitrate fluxes, and thus primary production in the upper ocean in warmer seasons.

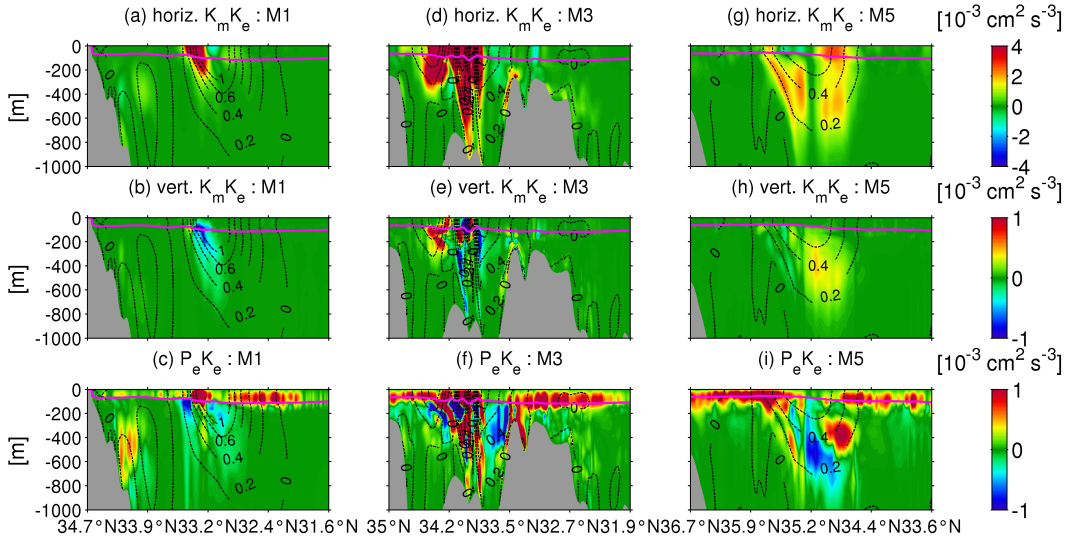

Figure 4.13. Cross-sectional plots of the seasonally averaged EKE source terms. Horizontal component of barotropic conversion rate K_mK_e (top row), vertical vertical component of K_mK_e (middle row), and baroclinic conversion rate, P_eK_e (bottom row), along the transects M1, M3, and M5 in winter. The magenta lines show the mixed-layer depth computed by the KPP model. The black dotted contours show eastward velocity normal to the transects, representing approximate positions of the Kuroshio.

4.5 Supplemental Figures

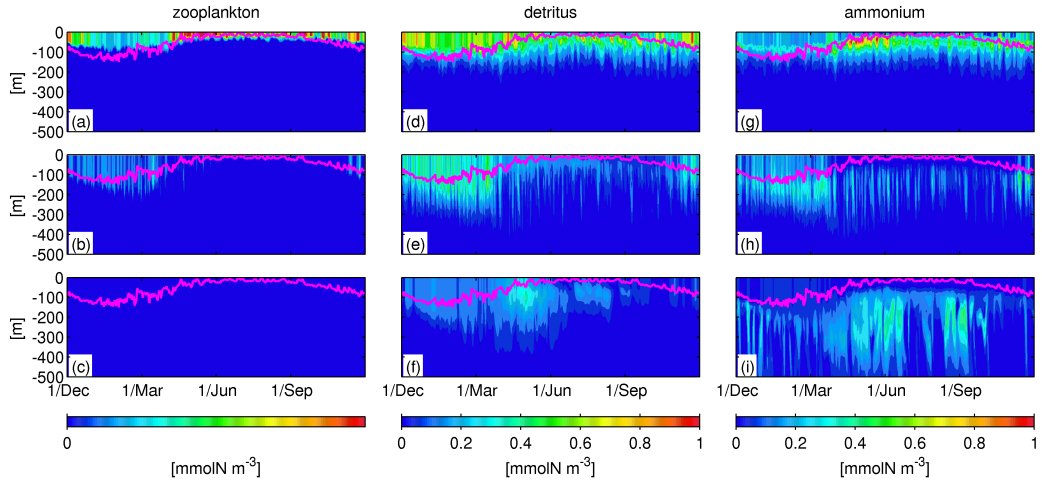

Figure S4.1. Hovmöller diagrams of the zooplankton concentrations (left column), detritus concentration (middle column), and ammonium concentrations (right column) in the northern (top row), central (middle row) and southern (bottom row) locations along 138°E in the Kuroshio Region (KR, M1 as shown in **Figure 4.1**). The magenta lines are the corresponding mixed layer depth determined by the K-Profile Parameterization submodel in ROMS.

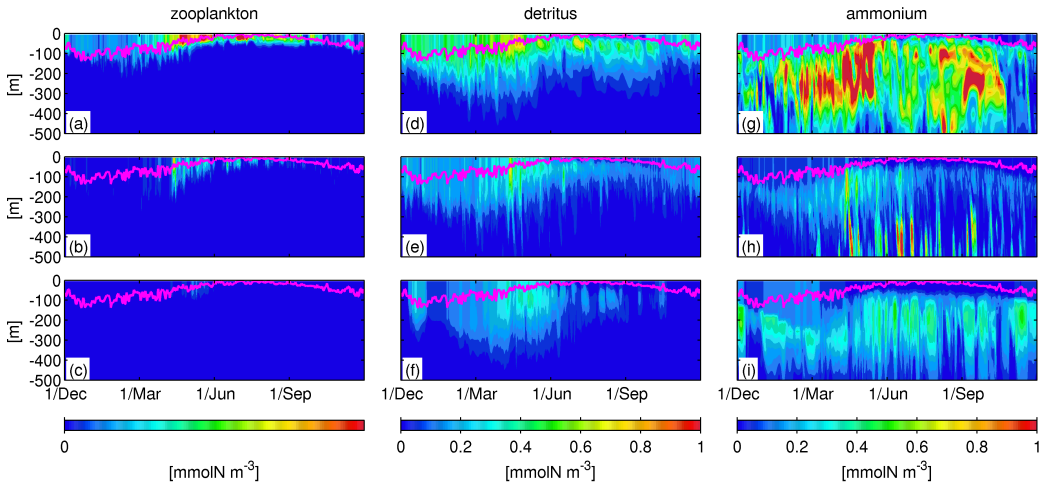

Figure S4.2. Same as **Figure S4.1**, but for 145°E in the Kuroshio Extension (KE, N1 as shown in **Figure 4.1**).

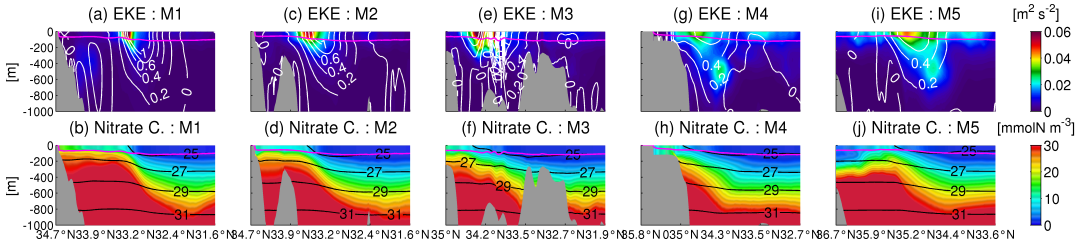

Figure S4.3. Cross-sectional plots of the seasonally averaged EKE (upper) and nitrate concentrations (lower) along the five transects M1-5 in winter (colors). Contours are eastern velocity [m/s] normal to the transects (upper) and potential density σ_θ [kg/m^3] (lower). The magenta lines are the seasonally averaged mixed-layer depths.

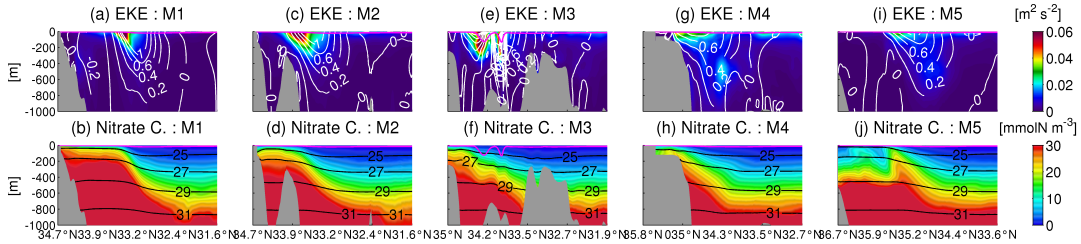

Figure S4.4. Same as **figure S4.3**, but in summer.

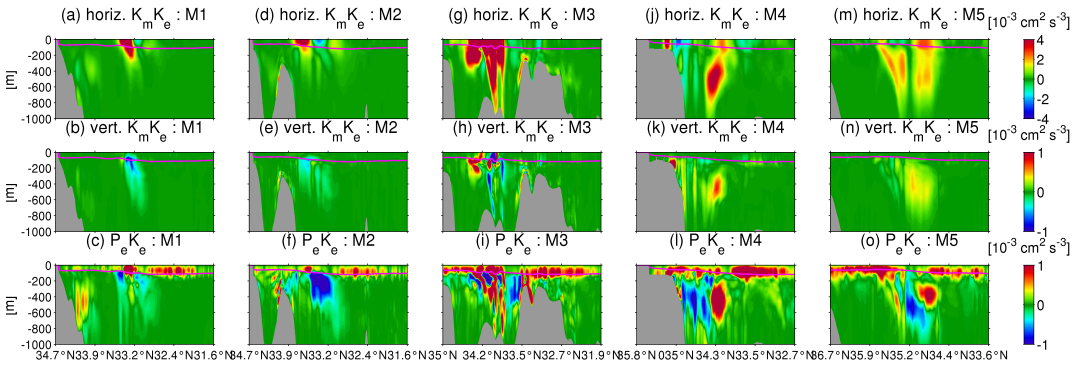

Figure S4.5. Cross-sectional plots of the seasonally averaged EKE source terms. Horizontal component of barotropic conversion rate K_mK_e (top row), vertical vertical component of K_mK_e (middle row), and baroclinic conversion rate, P_eK_e (bottom row), along the five transects M1-5 in winter. The magenta lines show the mixed-layer depth computed by the KPP model. The black dotted contours show eastward velocity normal to the transects, representing approximate positions of the Kuroshio.

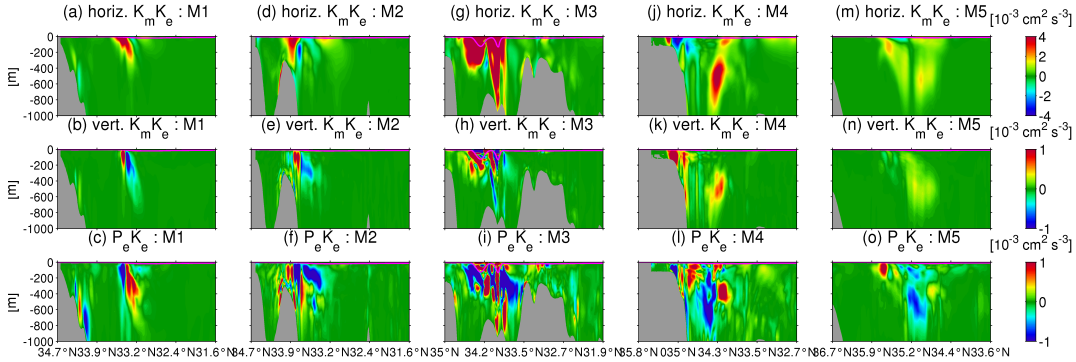

Figure S4.6. Same as **Figure S4.5**, but in summer.

5. Inter-annual variability of surface primary production induced by the Kuroshio meanders

5.1 Methods

5.1.1 Ocean circulation model

The numerical configurations used in this section basically follow the Section 4.1.1, except that a synoptic set-up was used in the newer model. In this section, we mainly concentrate on the inter-annual variability of the primary production at upper ocean driven by the large Kuroshio meandering. The study area is shown in **Figure 5.1**. The simulation is conducted for 8 years from 2008 to 2015 to account for spatiotemporal variability of the Kuroshio path. **Table 5.1** summarizes the detailed numerical configurations for the synoptic ROMS models. The results of last 4 years are utilized for the current analysis.

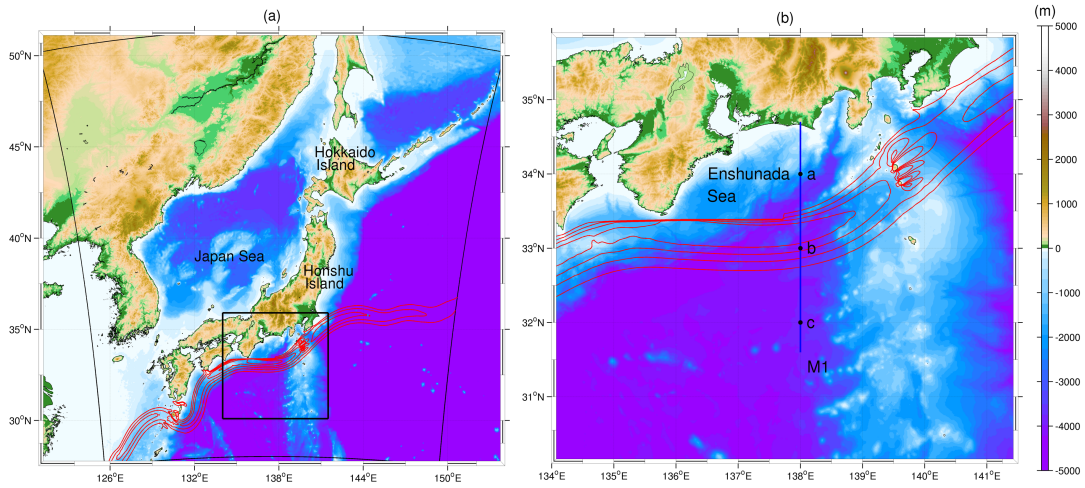

Figure 5.1. (a) The ROMS-NPZD model domain. (b) Blow-up region shown by the thick box in (a). The blue line annotated with M1 is the selected transect along 138°E with three black dots on M1 show the sampling locations for Hovmöller plots (**Figure 8, 9 and 10**). Red contours indicate the approximate Kuroshio path with surface velocity magnitudes ≥ 0.5 m/s at intervals of 0.3 m/s. Colors are bathymetry.

Table 5.1. Ocean circulation model configurations

Models	ROMS
Computational period	Jan. 1, 2008-Dec. 31, 2015
Grid cells	784 × 864 (× 32 layers)
Horizontal grid resolution	3 km
Baroclinic time step	150 s
Surface wind stress	JMA-GSM (daily climatology)
Surface flux	COADS (monthly climatology)
Boundary/Initial condition	JCOPE2 (monthly climatology)
T-S nudging	JCOPE2 (10-day averaged climatology)
Topography	SRTM30+JEGG500

STRM30: SRTM30_PLUS (Rodriguez et al., 2005; Rodriguez et al., 2006; Becker et al., 2009)
J-EGG500 (http://www.jodc.go.jp/data_set/jodc/jegg_intro.html)

5.1.2 Biogeochemical model

We employed a simple nitrogen-based pelagic NPZD biogeochemical model based on Fasham et al. (1991) with a modification described in Gruber et al. (2006), where we considers five components: nitrate $[NO_3^-]$, ammonium $[NH_4^+]$, phytoplankton $[Phyt]$, zooplankton $[Zoo]$ and detritus $[Det]$. The details of conservation equations and other model parameters follow Section 4.1.2 as summarized in **Table 5.2**. The seasonal climatology of the World Ocean Atlas 2005 (WOA05) (e.g., Garcia et al., 2006) and the monthly MODIS/Aqua satellite data provided the initial and lateral boundary conditions for nitrate and phytoplankton. The most essential difference between the current synoptic model and the above climatological model is that the synoptic MODIS/Aqua satellite data was used. Meanwhile, we also follow the configuration described in Gruber et al. (2006) and Uchiyama et al. (2017) to set zooplankton to be proportional to chlorophyll-a (Chl-a) concentration for its initial and boundary conditions. The model was run for 8 years from 2008 to 2015, and the last 4 years' data are utilized for the following analyses.

Table 5.2. Biogeochemical model configurations

Parameter	Symbol	Value	Unit
Half-saturation for phytoplankton NO_3^- uptake	$K_{NO_3^-}$	1.5	mmol N m^{-3}
Half-saturation for phytoplankton NH_4^+ uptake	$K_{NH_4^+}$	0.5	mmol N m^{-3}
Phytoplankton ammonium inhibition parameter	$\emptyset$	1.5	(mmol N)$^{-1}$
Phytoplankton loss to sink rate	$\mu_{[Phyt]}$	0.01	d^{-1}
Phytoplankton mortality to detritus rate	$\mu_{[Phyt][Det]}$	0.072	d^{-1}
Zooplankton maximum growth rate	g_{max}	0.75	d^{-1}
Zooplankton assimilation efficiency	β	0.75	n.d.
Zooplankton half-saturation for ingestion	K_{Phyt}	1.0	d^{-1}
Zooplankton loss to sink	$\mu_{[Zoo]}$	0.025	d^{-1}
Zooplankton specific excretion rate	$\mu_{[Zoo][NH_4^+]}$	0.1	d^{-1}
Zooplankton mortality to detritus	$\mu_{[Zoo][Det]}$	0.025	d^{-1}
Detrital loss to sink rate	$\mu_{[Det]}$	0.02	d^{-1}
Detrital breakdown to NH_4^+ rate	$\mu_{[Det][NH_4^+]}$	0.03	d^{-1}

5.2 Validation

5.2.1 Sea surface velocity and temperature

In the present study, the AVISO satellite data with a resolution of 1/4° (e.g., Traon et al., 1998) and Global Daily Sea Surface Temperature (MGDSST, at 1/4° resolution, Sakurai et al., 2005) with merged satellite and in situ data, and the parent JCOPE2 oceanic reanalysis are employed for the validation of ROMS model results. The time-averaged results are calculated from 2012 to 2015 in each data set. **Figure 5.2** indicates the comparison of the surface velocity between ROMS model result, the parent JCOPE2 reanalysis and the AVISO-SSH satellite data. The Kuroshio main body in ROMS model is almost same with that of the JCOPE2 and the AVISO data. The surface velocity estimated by ROMS is slightly faster than that of the JCOPE2 because a geostrophic acceleration occurs when the model is downscaled from JCOPE2 (~10 km) to ROMS (3 km). Also note that the reproducibility of present synoptic ROMS model is better than the climatological simulation described in Section 4, although the current numerical configuration follows Section 4.

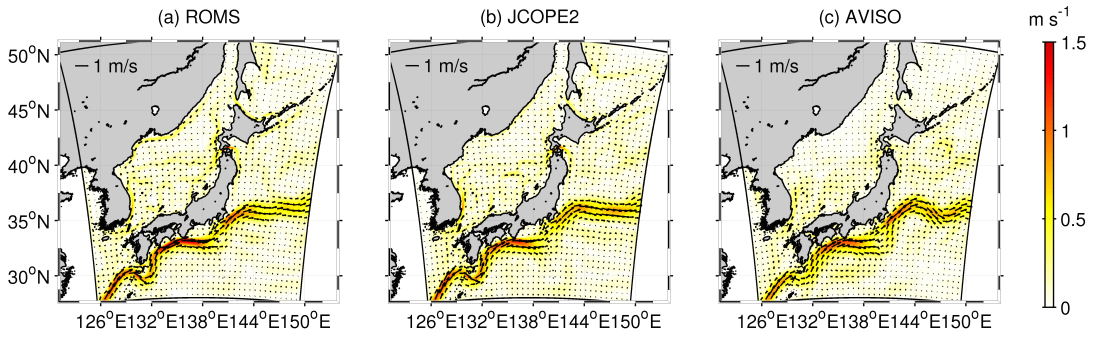

Figure 5.2. Time-averaged surface velocity vectors and their magnitude in color from (a) the ROMS model results, (b) the parent JCOPE2 reanalysis and (c) AVISO satellite data.

In addition, **Figure 5.3** shows the sea surface temperature (SST) of ROMS, JCOPE2 and MGDSST data sets, demonstrating that the SST computed by ROMS shows a good agreement with the MGDSST and JCOPE2 reanalysis, especially around the area along the Kuroshio fronts. A tiny weakness in ROMS is found in the northern area of the domain, whereas a warm bias has existed in its parent JCOPE2.

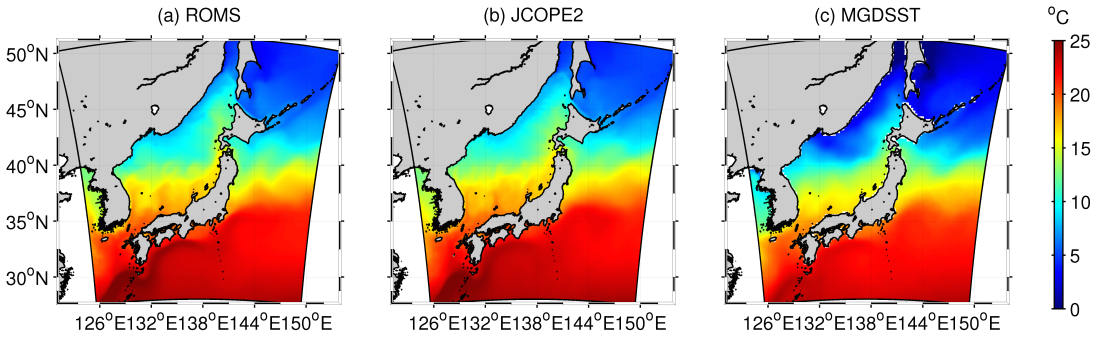

Figure 5.3. Time-averaged sea surface temperature (SST) in color from (a) the ROMS model results, (b) the parent JCOPE2 reanalysis and (c) MGDSST data.

5.2.2 Sea surface chlorophyll-a

The time-averaged surface Chl-a concentration from ROMS-NPZD model and the MODIS/Aqua satellite data investigated in **Figure 5.4**. The ROMS-NPZD model results show a modest well agreement as compared to the MODIS/Aqua data, particularly showing a segmentation in the primary production on the both sides of the Kuroshio with higher Chl-a concentration in the northern area of the axis. Coastal improvement of Chl-a concentration is generally reflected, which is enough for our present study. However, there are a few subtle bias between the model and observations. For example, the primary production is overestimated in the northeastern part of the domain by the model. The possible reason might be due to the lack of iron limitation mechanism (e.g., Fiechter et al., 2009; Moore et al., 2013) as we have mentioned in Section 4. Additionally, the Chl-a concentration near the coastal area is underestimated because the land-derived nutrient input is not taken account. Again noted that we ignored the land-derived nutrient source in the present study because our primary aim is to understand oceanic eddy dynamics on vertical nutrient transport to maintain the primary productivity near the surface layer. Therefore, we consider the simplified geophysics-biogeochemistry relationship employed here to be useful to diagnose biological responses to eddying flow fields in the upper ocean around the Kuroshio.

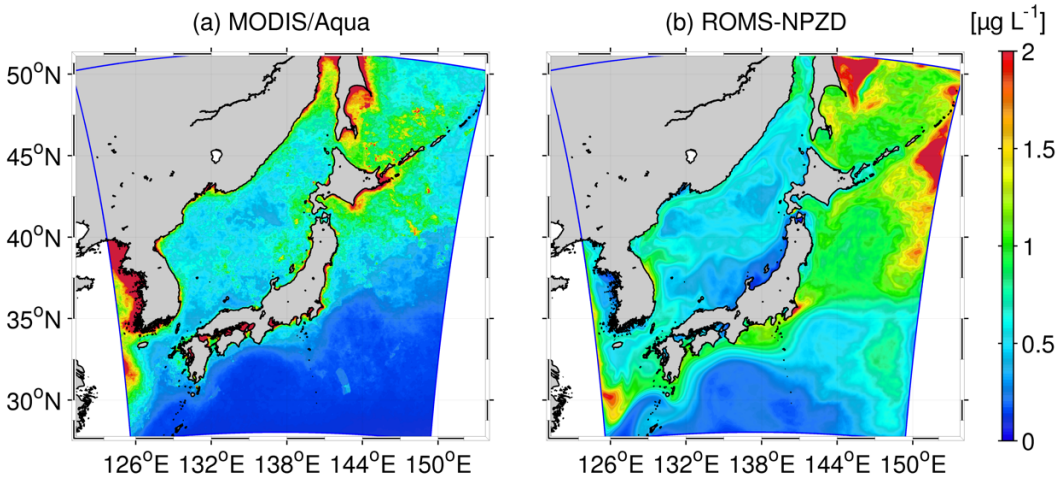

Figure 5.4. Time-averaged surface chlorophyll-a (Chl-a) concentrations in color from (a) MODIS/Aqua satellite data and (b) the ROMS-NPZD model.

5.3 Temporal variability of the Kuroshio and associated biological responses

The approximate position of the Kuroshio axis along 138°E is depicted in **Figure 5.5**, which is defined by the maxima of the surface current velocity in the present study. The averaged Kuroshio axis is aound 33°N during the analysis period. Therefore, three obvious southward meanders are detected: 1) the first meander occurs from November of 2012 to February of 2013, including a winter; 2) the second one appears from July of 2013 to April of 2014, lasting about three seasons; 3) the third one is a relative smaller meander and occurs from July of 2015 to November of 2015, including around two seasons.

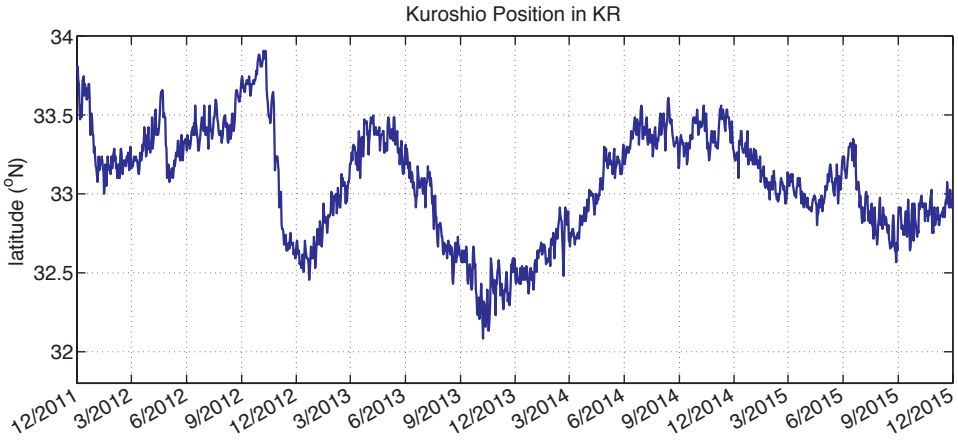

Figure 5.5. The approximate position of the Kuroshio path at the transect along 138°E as shown in **Figure 5.1b**. The Kuroshio axis is defined by the maxima of the surface current velocity.

It is expected that the primary production is affected horizontally and vertically when the Kuroshio meander happens. To understand the mechanisms of such different responses of the primary production due to the Kuroshio oscillation, we investigate the vertical structures of central location relative to the Kuroshio axis (located at 33°N) and two locations ± 1.0° away from the axis. In the present model, the nitrogen source is considered as nitrate to be distributed in the deep region under the mixed layer. **Figure 5.6** shows Hovmöller diagrams of the nitrate concentration in the northern, central, and southern sides of the Kuroshio from the top to the bottom rows along 138°E (M1, **Figure 5.1b**) in the KR. The magenta lines indicate the corresponding mixed layer depth determined by the KPP boundary-layer sub-model. **Figure 5.7** shows the same plots as **Figure 5.6**, but for phytoplankton concentration.

Firstly, variability of the nitrate supply to surface and the mixed layer depth generally fluctuate at seasonal frequencies. The mixed layer deepening appears in cold seasons from December to April in each year. And then elevated nitrate supply to the surface shows a significant spatial difference. The enhancement of nitrate to the surface is most obvious at the northern station (**Figure 5.6a**), while it is very low at the southern station (**Figure 5.6c**), because nitrate distribution shows a general difference between both sides of the Kuroshio with a higher concentration to the north. The temporal pattern is pretty complicate at the central station (**Figure 5.6b**) because its relative position often changes to the Kuroshio axis (**Figure 5.5**). Winter is included, when the first two large Kuroshio meanders appear from November of 2012 to February of 2013, and from July of 2013 to April of 2014. Therefore, the enhancements of nitrate supply to the surface occur from December of 2012 to February of 2013, and from December of 2013 to March of 2014 at the central station (**Figure 5.6b**). On the other hand, warm seasons are briefly covered by the second meander occurring in August of 2013. The subsurface nitrate elevation is also apparent in warm seasons during meandering, as compared with the case without meandering.

Phytoplankton is distributed much deeper in cold seasons rather than warm seasons and is sensitive to the nitrate concentration fluctuation (**Figure 5.7**). The primary production occurs more actively at the northern station (**Figure 5.7a**). Phytoplankton fluctuates quite sensitively in response to the southward Kuroshio meanders in the mixed layer at the central station. There is significant increase of primary production at the central station, when the strong oscillations happen in 2013 and 2014 (**Figure 5.7b**). In addition, more active primary production appears at deeper region in warm seasons during the meandering, although the mixed layer is very shallow. These results clearly demonstrate that nutrient fluxes from the nutrient-rich subsurface layer to the nutrient-depleted surface layer are substantial for maintaining primary production near the surface.

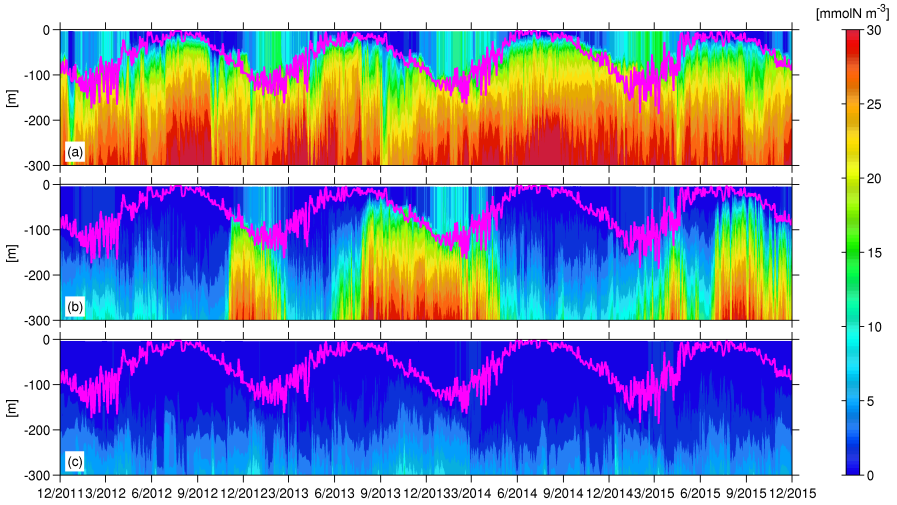

Figure 5.6. Hovmöller diagrams of the nitrate concentrations in the northern (top row), central (middle row) and southern (bottom row) locations represented by black dots **Figure 5.1b**. The magenta lines denote the corresponding mixed layer depth.

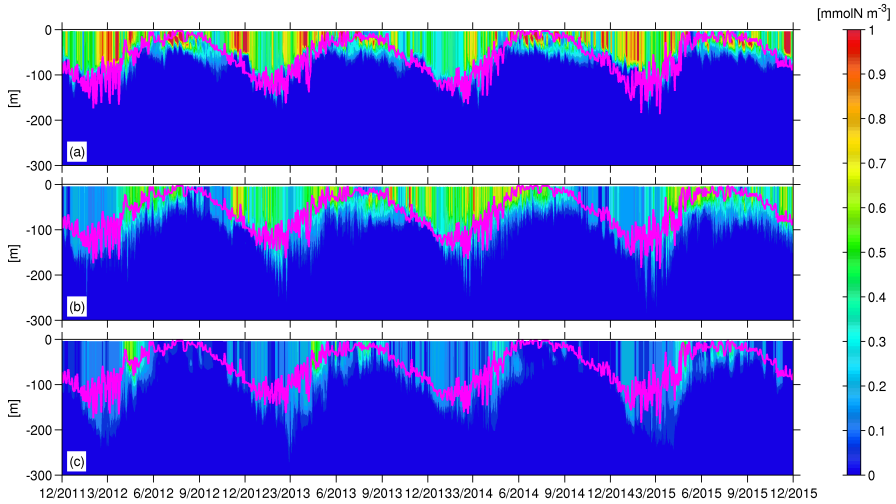

Figure 5.7. Same as **Figure 5.6**, but for the phytoplankton concentrations.

5.4 Impacts of the Kuroshio meander

5.4.1 Horizontal structures at upper-ocean layer

In the present study, we concentrate on the effects of the transient Kuroshio path on the upper-ocean physical environment and associated biogeochemical responses, when the large meanders occur in the KR. Therefore, we select several periods with and without the large meanders in summer for the following analysis. **Figure 5.8** shows the two-week averaged plots of sea surface velocity (top), surface nitrate concentration (middle) and surface Chl-a concentration (bottom) in the zoom-in region (**Figure 5.1b**) in summer. The left column is selected for the case without a large meander computed between August 1st, 2012 and August 14th, 2012, while the right column is chosen for the case with a large meander calculated between August 1st, 2013 and August 14th, 2013. As compared to the situation without the Kusohio meander (**Figure 5.8b**), the nitrate concentration is significantly higher in the nearshore area with meandering, while it is lower in the offshore area (**Figure 5.8c**). When the Kuroshio takes a relative straight path (without a large meander), the high Chl-a concentration in north side of the Kursohio axis varies with the front (**Figure 5.8e**). And partial maxima and minima of Chl-a concentration occurs in the north side. The surface Chl-a concentration becomes lower in the basin area as compared with that without a meander, when the meander occurs. By contrast, a higher Chl-a concentration appears near the coast (**Figure 5.8f**). Such a distribution pattern is modestly consistent with the nitrate concentration. In addition, it should be noted that the mixed layer becomes thinner in summer. Therefore, phytoplankton might mainly distribute under mixed layer, resulting in phytoplankton reduction at the surface layer.

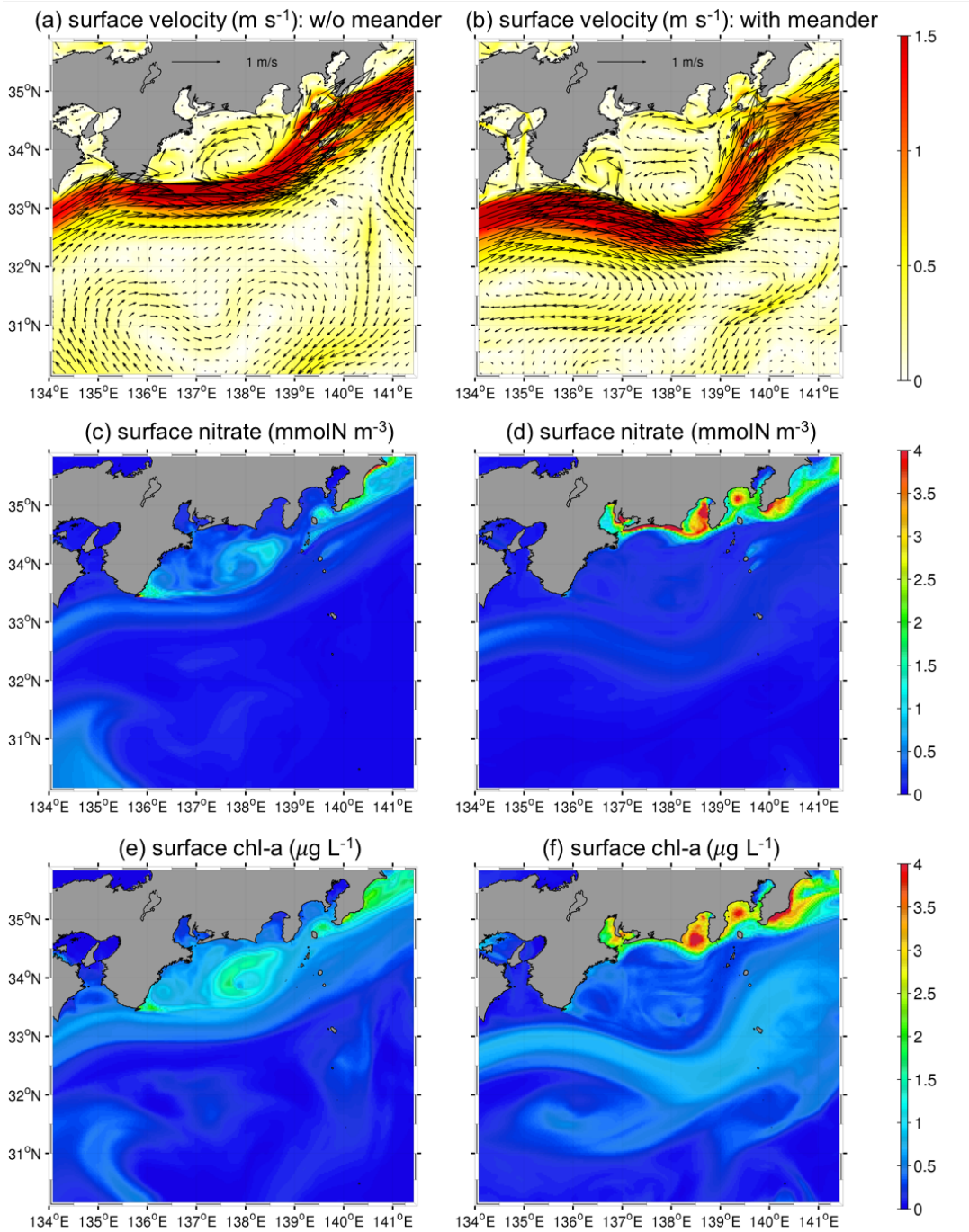

Figure 5.8. Time averaged (two-weekly) values of the sea surface velocity vectors (arrows) with their magnitude (color) on the top, sea surface nitrate concentration on the middle, and sea surface Chl-a concentration on the bottom rows as shown in the enlarged area as shown in **Figure 5.1b**. The data is calculated between August 1st, 2012 and August 14th, 2012 without the Kuroshio meander on left column, and between August 1st, 2013 and August 14th, 2013 with the Kuroshio meander on the right column for comparison in summer.

Figure 5.9 shows the time-averaged relative vorticity normalized by the Coriolis parameter (color), and the sea surface velocity vectors (arrows) on the upper row, and depth of isopycnal layer of 1023 kg m^{-3} on the lower row. A positive vorticity weakening occurs in the basin area during the Kuroshio meandering. Meanwhile, the negative voticity around ~138°E and 34°N also reduces accompanied with enlarging distribution region. In contrast, a relative energetic positive voticity is promoted in the nearshore area (**Figure 5.9b**). From the depth of isopycnal height, it is clear that the isopycnal layer is shallower in the part near the coast, while it is deeper in the offshore region (**Figure 5.9d**), when the Kuroshio meander happens. It is generally consistent with the relative vorticity distribution. This also indicates that the partial maxima of Chl-a concentration occurring in the basin area are because of cyclone-induced upwelling, resulting increase of the isopycnal layer. At the same time, isopycnal height elevation (**Figure 5.9d**) promotes stronger coastal nitrate upwelling in the nearshore area, playing an essential role in maintaining the active primary production during the southward Kuroshio oscillation (**Figure 5.8f**).

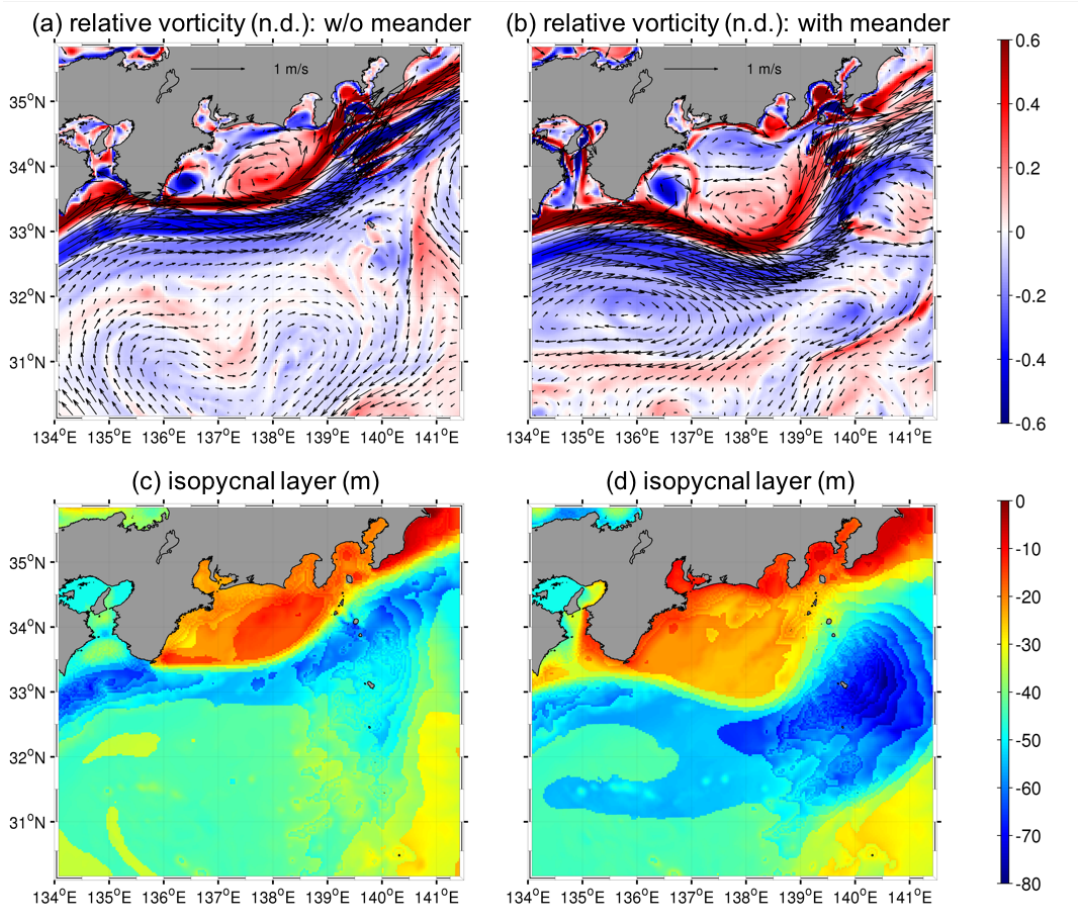

Figure 5.9. Upper panels: Time-averaged relative vorticity normalized by the Coriolis parameter at the surface (color), and the sea surface velocity vectors (arrows). Lower panels: Depth of isopycnal layer of 1023 kg m^{-3}.

Next, we introduce a Reynolds decomposition to the prognostic variables for the mean and transient components. The vertical nitrate flux F_V are decomposed into the mean and transient components using the following equation:

$$F_V = Nw \approx \underbrace{\bar{N}\bar{w}}_{\text{mean}} + \underbrace{\overline{N'w'}}_{\text{transient}}, \quad (5.1)$$

where w is the upward vertical velocity; N is nitrate concentration ($[NO_3^-]$); the overbar denotes an ensemble (time) averaging operator; and the prime indicates the fluctuating (transient) component for the periods shorter than 14 days calculated with a Butterworth frequency filter. Note that we use 14 days as cutoff period because of the duration of the Kuroshio meander. To assess the importance of different components of vertical nitrate flux, we compared relative contributions of the three vertical nitrate fluxes, mean advective nitrate flux $\bar{N}\bar{w}$, transient nitrate flux, $\overline{N'w'}$, and diffusive nitrate flux $-K_v\partial_z\bar{N}$, where K_v is the KPP-derived vertical eddy diffusivity, to the vertical nitrate transport in the upper ocean.

Figure 5.10 illustrates the upper-ocean spatial distributions of the vertical mean advective nitrate flux, $\bar{N}\bar{w}$, on the top, transient flux, $\overline{N'w'}$, on the middle, and diffusive flux $-K_v\partial_z\bar{N}$ on the bottom panels. The results without and with the Kuroshio meander are shown on left and right columns, respectively. Three flux components are generally stronger without meandering (**Figure 5.10a, c and e**) as compared with those with meandering (**Figure 5.10b, d and f**). Obviously, the vertical mean advective and transient fluxes are commonly large in magnitude, but showing opposite signs somewhere, indicating that they compete each other in contributing to stonger primary production. However, both of them are generally positive in the basin region around ~138°E and 33.4°N, which is also consistent with the horizontal distribution of primary productivity (**Figure 5.8e**). Additionally, the diffusive flux is also non-trivial for maintaining the upper-ocean primary production (**Figure 5.10e**). In contrast, when the Kuroshio meander appears, the mean advective and transient components decreases apparently, particularly in the offshore area (**Figure 5.10b and d**). However, in the nearshore region, the mean advective flux is stronger than that withou meaner. Apart from that, diffusive flux becomes much more dominant as compared with two other components (**Figure 5.10f)**, even though it is still weaker than the case without meandering.

In summary, as compare to the situation without the Kuroshio meander, the primary production becomes weaker in basin part because of weakening of three flux components, while it is more active in the coastal region due to stronger mean advective nitrate flux.

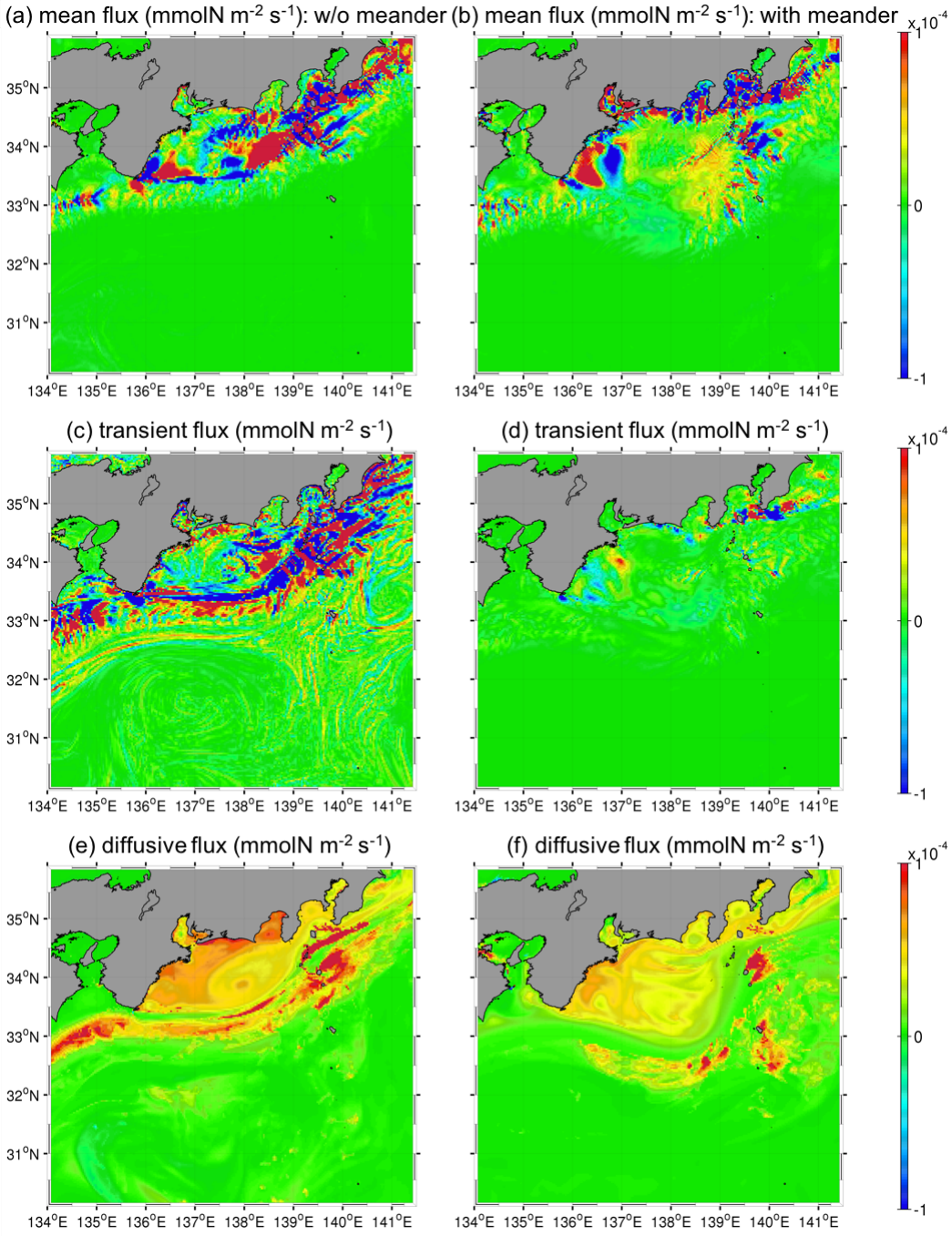

Figure 5.10. Upper-ocean spatial distributions of the vertical mean advective nitrate flux, $\overline{N}\overline{w}$, on the top, transient nitrate flux, $\overline{N'w'}$, on the middle, and diffusive flux $-K_v\partial_z\overline{N}$ on the bottom rows. They indicate the results without the Kuroshio meander on left column, and results with the Kuroshio meander on the right column.

5.4.2 Vertical structures around subsurface

As we mentioned that nutrient fluxes from the nutrient-rich subsurface layer to the nutrient-depleted surface layer are substantial for maintaining primary production near the surface, we choose a transect along 138°E to analyze the vertical structures. **Figure 5.11** shows the cross-sectional plots of the time averaged phytoplankton (upper) and nitrate (lower) concentrations along 138°E as shown in **Figure 5.1** in color. White contours are eastern velocity normal to the transects, denoting the approximate Kuroshio position (upper). Two magenta lines corresponds to the isopycnal height of 1023 and 1026 kg m^{-3}, respectively (lower). The phytoplankton distributes more broadly but with lower concentration, when the Kuroshio path oscillates southward (**Figure 5.11b**). An obvious phytoplankton reduction also occurs in a very shallow layer (around upper 10m depth), because the phytoplankton is stored under mixed layer, leading to insufficient mixing. On the other hand, the nitrate concentration also reduces significantly at subsurface layer (~100 m depth) during the Kuroshio meandering. In addition, when the Kuroshio meander appears, the isopycnal height deepens modestly (**Figure 5.11d**), efficiently trapping the nitrate. This is considered as the reason why the vertical nitrate fluxes are weak, further resulting in reduction of the surface phytoplankton concentration during the meandering.

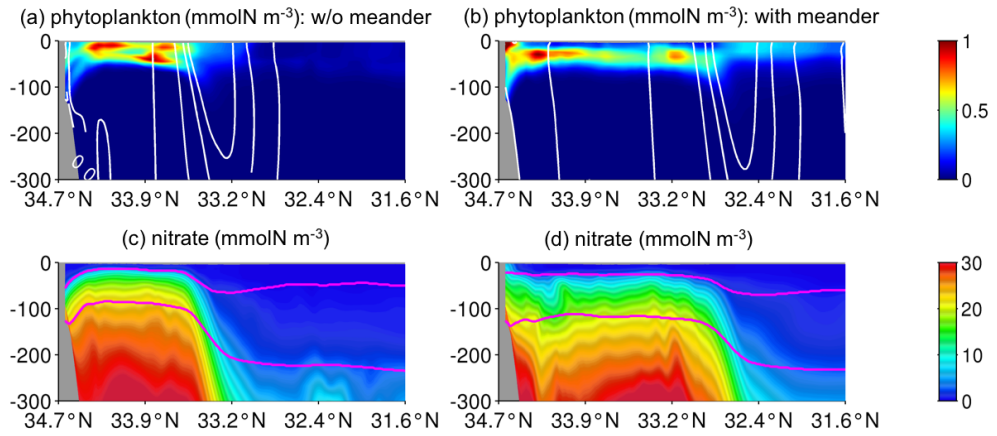

Figure 5.11. Cross-sectional plots of the time averaged phytoplankton (upper) and nitrate (lower) concentrations along the transect as shown in **Figure 5.1** in color. White contours are eastern velocity normal to the transects, denoting the approximate Kuroshio position (upper). Two magenta lines corresponds to the isopycnal height of 1023 and 1026 kg m^{-3}, respectively (lower).

Next, we discuss the contribution of different flux components. The mixed layer is pretty thin, leading to the diffusive nitrate flux can be ignored in deep region (not shown). Therefore, we focus on the mean and transient components in the following analysis. **Figure 5.12** shows the cross-sectional plots of the vertical mean advective nitrate flux, $\overline{N}\overline{w}$, on the upper panels, and vertical transient nitrate flux, $\overline{N'w'}$, on the lower panels. Firstly, the mean components dominate over the transient components in two cases without and with the Kuroshio meander. In addition, as compared to the case without meander, the mean advective nitrate flux becomes much weaker (**Figure 5.12b**), especially at the subsurface (~100 m depth), again indicating that mean flux reduction is one key influencer of the less active primary production during the southward Kusohio oscillation.

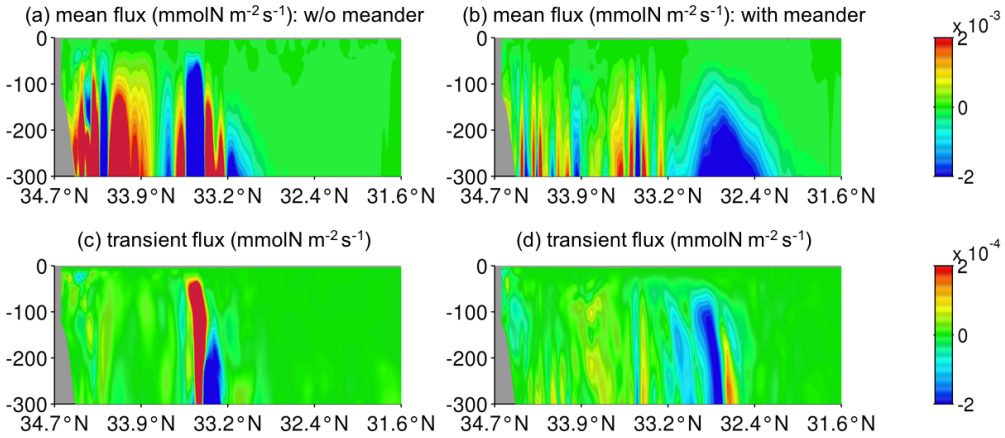

Figure 5.12. Cross-sectional plots of the vertical mean advective nitrate flux, $\overline{N}\overline{w}$, on the upper panels, and vertical transient nitrate flux, $\overline{N'w'}$, on the lower panels.

6. Conclusions

In the present study, we totally developed three simulations to analyze anthropogenic and natural biological impacts on the marine ecosystem, further predicting the potential influences on human being's life. We selected Osaka Bay as an example to focus on the anthropogenic impacts in a semi-enclosed estuarine area with strong tidal currents. In such a "basin-strait" system, land-derived nutrient is important source for marine ecosystem. However, Osaka Bay, situated in the Seto Inland Sea, is strongly affected by the through-flow due to the eastward drifting Kuroshio. Therefore, we enlarged the research area to encompass the Kuroshio Region (KR) and Kuroshio Extension (KE) regions to assess the natural influences of vertical nutrient supply from nutrient-rich subsurface to nutrient-exhausted surface due to mesoscale and submesoscale eddies.

In Section 2, we developed a quadruple-nested, high-resolution model based on Regional Oceanic Modeling System (ROMS) with a horizontal of 20 m to confirm the improvement of the western diversion outfall on the local environment in Osaka Bay. A Eulerian near-field effluent dilution model was employed to reproduce 3-D advection-dispersion processes of the under-resolved, bottom-released buoyant effluent plume at the TSTP. The land-derived nutrients are generally from different source, including riverine runoff, wastewater from treatment plant, and so on. So the sewage effluent is the only tracer source in the present numerical configuration. The time-averaged surface currents are primarily driven by the clockwise Okinose Circulation formed off the TSTP, which substantially determines the large-scale, residual dynamics including the nearshore counterclockwise recirculation manifested near the TSTP. The currents fluctuate prominently at semidiurnal and diurnal tidal frequencies, with a notable influence of low-frequency subtidal variability. The TSTP and western portion of the seaweed farm located closer to the tidal strait are largely affected by tidal currents. In contrast, subtidal residual currents induced by surface wind stresses and constrained by the Okinose Circulation have prevailing effects in the eastern portion of the farm. The effluent measured by non-dimensional Eulerian passive tracer concentration generally follows these circulation patterns. The effluent transport is mostly controlled by subtidal residual currents, in particular by the offshore-directed current of the nearshore counterclockwise recirculation that subsequently merges with the Okinose Circulation to promote southeastward offshore effluent transport. A twin numerical experiment for cases with normal and western diversion outfalls enabled us to quantitatively evaluate the effect of the diversion. However, the dynamical effects due to the diversion were found to be subtle for the relatively small freshwater discharge of 1.80×10 m^3 d^{-1}. An overall reduction of the effluent affecting the farm was discovered, although the distance between the two outfalls is only 500 m in the alongshore direction. The effluent flux budget analysis

revealed that the cumulative nondimensional effluent of the seaweed farm is reduced by ~0.81 × 10^4 m^3 on average compared with that of the normal outfall (~2.83 × 10^4 m^3), exhibiting a ~28% reduction of the effluent from the TSTP by the diversion, which could lead to favorable influences on the growth of seaweeds. The growth rate of seaweed (e.g., Porphyra yezoensis) decreases exponentially as sewage water concentration increases under low sewage concentration conditions lower than 5% (Maruyama et al., 1985). This is the case for the present conditions, where the surface concentration in the farm is only 0.1%-0.01% relative to that at the source. Therefore, we consider that the current alternative operations have modest improvement on the seaweed production. The farm located in the east of the TSTP encounters incoming effluent fluxes from the western, northern, and eastern cross sections, whereas outgoing flux is invoked at the southern section. The eastern positive flux lags behind the initialization, indicating the dominance of a recurring tracer that has flowed out of the farm or comes from the south.

Even though the western diversion outfall decreases the effects of the sewage effluent on the seaweed farm, the local fishermen are still demanding that the government should further diminish the influence of the treatment plant. In Section 3, we conducted two more alternative scenarios to assess the impacts of wastewater effluents by reducing the sewage discharge rate and changing the wastewater density. In two additional cases, the sewage was also released from the western diversion outfall. We discovered that 16.7% of the wastewater discharge rate decreased from the standard diversion operation resulted in an overall 25.4% reduction in the sewage effluent accumulating on average in the seaweed farm. In turn, the addition of ambient seawater to the freshwater effluent to adjust the source density did not substantially alter the effluent accumulation and associated hydrodynamics at the farm because of the shallow bottom-mounted outfall (~7 m depth). A Reynolds decomposition demonstrated that the transient flux played a dominant role over the mean component in the effluent accumulation in the farm, more evidently in the cross-shore transport than the alongshore transport. When the source effluent flux was reduced, the transient component remarkably depressed the southward influx at the northern boundary of the seaweed farm. In contrast, in the along-shore direction, the mean and transient components competed with each other, leading to comparable effluent outfluxes and influxes, respectively.

As we mentioned above, Osaka Bay, located in the Seto Inland Sea, is strongly affected by the through-flow due to the drifting Kuroshio. Therefore, it is worthy enlarging the study area covering Kuroshio Region (KR) and Kuroshio Extension (KE) regions to analyze the seasonal biogeochemical process. In Section 4, we investigated seasonal variability of eddy fluxes that sustain the upper ocean primary productions and the driving mechanisms behind them in the KR and KE regions. To this end, we conducted a submesoscale eddy-permitting ocean modeling based on ROMS coupled with a nitrogen-based NPZD (Nutrient, Phytoplankton, Zooplankton, and Detritus) biogeochemical model, including the KR and KE regions off the Pacific coast of Japan.

Note that the present coupled model is a simplified nitrogen-based version where we only consider five components. For example, iron limitation is important to suppress the primary production (e.g., Fiechter et al., 2009; Moore et al., 2013). Another important influencer on the primary productivity is dissolved oxygen. Such problems limiting the simulated reproducibility should be taken into account in the future work. The model was run for 10 years in a climatological configuration and the last 10th year was utilized in the analyses. The surface chlorophyll-a (Chl-a) distributions show that the segmentations in the primary productivity occur on both sides of the Kuroshio with a higher Chl-a concentration on the northern area. An obvious spring bloom occurs more actively on the northern side of the KE and on the main path of the Kuroshio. Enhanced vertical mixing in winter and subsequent improvement of the light condition in spring results in active primary productions around the Kuroshio both in the KR and KE. The overall upward entrainment from the nutrient-rich subsurface to the nutrient-exhausted surface is substantial for maintaining the near-surface primary productivity. However, a downward eddy nitrate fluxes are found in winter in the upstream (Enshu-nada Sea region) and the downstream regions relative to the ridge in the KR. The eddy generation analysis indicates that, in winter, the topographic eddy shedding, positive barotropic conversation rate (K_mK_e), and baroclinic conversion rate (P_eK_e) jointly promote eddy-driven downward nitrate fluxes through shear instability and baroclinic instability most vigorously in the mixed layer along the Kuroshio path and its northern side in the KR, which eventually suppresses biological production. Meanwhile, positive P_eK_e leads to relatively weak upward nitrate flux that maintains the primary production on the southern side. In the KE, upward eddy flux due to the combination of positive K_mK_e and P_eK_e enhances the primary production in the upper ocean. Influences of submesoscale eddy-driven, near-surface baroclinic instability extend broadly in the meridional direction with a southward bias in the upstream while a northward bias in the downstream region, attributed to the spatially heterogeneous Chl-a distributions. By contrast, in summer, the mixed layer depth becomes very shallow and thus makes the upper ocean P_eK_e almost vanish in both KR and KE. Positive K_mK_e and P_eK_e arise mostly at depth beneath the mixed layer, which considerably interact with the ridge topography in the KR to increase in the upstream while decrease in the downstream regions. In the KE, as P_eK_e is prominently reduced in summer, eddy nitrate flux is decreased significantly in particular on the north of the Kuroshio. Therefore, baroclinic instability is the key influencer on seasonal variability in eddy generation near the surface, where vertical eddy mixing is inevitably important to promote the subsurface nutrient supply to the upper ocean. In addition, impacts of the oceanic ridge (Izu-Ogasawara Ridge) are examined in the KR. One essential difference between two regions is that the spatial variability of the vertical eddy nitrate flux fluctuates more frequently in KR rather than KE. The spatial variability of the eddy-driven nitrate flux and the underlying eddy generation mechanism are significantly altered by the ridge topography. Turbulence associated with the Kuroshio trends to be less

energetic in the upstream, while the ridge generates intensive eddy mixing more broadly and deeply in the downstream mainly due to the interaction between the Kuroshio front and ridge topography that results in mesoscale eddy-generating baroclinic instability. Although the near-surface nitrate concentration is lower in the downstream, the upward eddy-driven nitrate flux is stronger there to maintain active primary production due to the shear instability and baroclinic instability in winter. With the quantitative comparison among the three major EKE source terms, we found that P_eK_e and the horizontal K_mK_e dominate over the vertical K_mK_e on eddy generation in the KR. The horizontal K_mK_e increases in the Kuroshio path and the region near the ridge, while P_eK_e is intensive and highly variable in time in the mixed layer.

We mainly focus on the seasonal variability of the eddy fluxes and the driving mechanism behind them in the KR and KE regions based on a climatological configuration in Section 4. It was able to provide a relative simple and stable physical surrounding for the biogeochemical process. However, when the Kuroshio meander appears, the associated biogeochemical responses should be also taken into account. In Section 5, we developed a synoptic, retrospective downscaling ocean modeling based on ROMS coupled with an NPZD biogeochemical model, encompassing the same domain with the above climatological model. The simulation was conducted for 8 years from 2008 to 2015 to account for spatiotemporal variability of the Kuroshio path, and the results of last 4 years from December of 2011 to November of 2015 were utilized for the analysis. There are three obvious meanders during our analysis period. When the meander happens in summer, more significant nitrate depletion occurs in the surface layer, resulting in relative weak primary productivity but larger distribution. The Kuroshio meander leads to weakening of nutrient upwelling near surface. In the offshore region, mean and transient nitrate flux decreases during the meandering, while diffusive flux plays important role in maintaining nutrient upwelling near surface. By contrast, in the coastal part, mean component is essential for the active primary production. Isopycnal height deepening during meander suppresses the nutrient upwelling at subsurface layer.

Overall, we confirmed the reduction of the nutrient impacts on the marine ecosystem at the TSTP, when the western diversion outfall was used instead of the central normal outfall. The western diversion outfall successfully decreased the wastewater effluent accumulating in the seaweed farm by ~0.81×10^4 m^3 on average compared with that of the normal outfall (~2.83×10^4 m^3), accounting for ~28% reduction during our computational period when the seaweed spores are seeded onto collectors to be hatched. Furthermore, we conducted two more cases to test potential optimization programs. We discovered that 16.7% of the sewage released volume rate efficiently led to an overall 25.4% reduction of the cumulative passive effluent of the seaweed farm. In turn, the adjusted effluent density with the unchanged total effluent flux did not result in obvious changes in the effluent accumulation and associated hydrodynamics, particularly at the seaweed farm. We have understood the impacts of sewage transport driven by tidal

currents in an estuary, and these researches about anthropogenic impacts provide efficient plan to increase the aquaculture production. Then we discussed another essential nutrient source existing in nature, which is the nitrate supply from nutrient-rich subsurface to nutrient-depleted surface layer. It is important for the primary production in the coastal and marginal seas to influence global climate change. We investigated seasonal variability of eddy fluxes that sustain the upper ocean primary productions and the driving mechanisms behind them in the KR and KE regions. To understand such spatiotemporal variability of the biological processes is important to make long-term economic development planning. In winter, the positive barotropic conversation rate (K_mK_e) and baroclinic conversion rate (P_eK_e) jointly promote eddy-driven downward nitrate fluxes through shear instability and baroclinic instability along the Kuroshio path and its northern side in the KR, competing the biological production. The upward eddy flux due to the combination of positive K_mK_e and P_eK_e enhances the primary production in the KE. By contrast, in summer, positive K_mK_e and P_eK_e arise mostly at depth beneath the mixed layer along the Kuroshio in the KR. In the KE, as P_eK_e is prominently reduced in summer, eddy nitrate flux is decreased significantly. Therefore, baroclinic instability is the key influencer on seasonal variability in eddy generation near the surface, affecting the associated vertical nutrient transport to the upper ocean. In addition, impacts of the oceanic ridge (Izu-Ogasawara Ridge) are examined in the KR. Turbulence associated with the Kuroshio trends to be less energetic in the upstream, while the ridge generates intensive eddy mixing more broadly and deeply in the downstream. The Kuroshio meander weakens nutrient upwelling near surface, competing the upper ocean primary production.

Acknowledgment

First of all, I would like to appreciate professor Yusuke Uchiyama for providing me kind and helpful comments that make my research of great accomplishment and my academic career invaluable and unforgettable.

Great acknowledgment is also make to my colleagues, Naru Takaura, Natsuki Tokunaga, Hongxin Wang, Kosei Matsushita, Motoki Ubara, Kimika Takeyasu, and Kohei Kawano for their help in Uchiyama laboratory. Best wishes for their future success and lab's further prosperity.

References

Abowei, J.F.N., and Ezekiel, E. N., The potentials and utilization of seaweeds. *Sci. Agri*. **4:2**, 58-66 (2013).

Ardyna, M., Babin, M., Gosselin, M., Devred, E., Bélanger, S., Matsuoka1, A., and Tremblay, J., Parameterization of vertical chlorophyll *a* in the Arctic Ocean: impact of the subsurface chlorophyll maximum on regional, seasonal and annual primary production estimates, *Biogeosciences Discuss.*, **10**, 1345–1399 (2013). doi:10.5194/bgd-10-1345-2013.

Ballantyne, A. P., Alden, C. B., Miller, J. B., Tans, P. P., and White, J. W. C., Increase in observed net carbon dioxide uptake by land and oceans during the past 50 years, Nature, 488, 70-73 (2012). doi:10.1038/nature11299.

Bauer, J. E., Cai, W., Raymond, P. A., Bianchi, T. S., Hopkinson, C. S., and Regnier, P. A. G., The changing carbon cycle of the coastal ocean, Nature, 504, 61-70 (2013). doi:10.1038/nature12857.

Becker, J. J., Sandwell, D.T., Smith, W. H. F., Braud, J. Binder, B., Depner, J., Fabre, D., Factor, J., Ingalls, S., Kim, S-H., Ladner, R., Marks, K., Nelson, S., Pharaoh, A., Trimmer, R., Von Rosenberg, J., Wallace, G., Weatherall, P., Global bathymetry and elevation data at 30 Arc Seconds Resolution: SRTM30_PLUS. *Mar. Geodes*. **32:4**, 355-371 (2009).

Bricker, J. D., Okabe I., and Nakayama, A., Behavior of a small pulsed river plume in a strong tidal cross-flow in the Akashi Strait. *Environ. Fluid Mech*. **6**, 203-225 (2006).

Bricker, J. D., and Nakayama, A., Estimation of far-field horizontal and vertical turbulent diffusion coefficients from the concentration field of a wastewater plume near the Akashi Strait. *Environ. Fluid Mech.* **7**, 1-22 (2007).

Buijsman, M., Uchiyama Y., McWilliams J. C., Hill-Lindsay C. R., Modeling semiduirnal internal tides in the Sourthern California Bight. *J. Phys. Oceanogr.*, **42**, 62–77 (2012). doi: 10.1175/2011JPO4597.1.

Chang, P. H., Guo, X., Takeoka, H., A numerical study of the seasonal circulation in the Seto Inland Sea, Japan. *J. Oceanogr.* **65**, 721-736 (2009).

Chelton, D. B., Gaube, P., Schlax, M. G., Early, J. J., Samelson, R. M., The Influence of nonlinear mesoscale eddies on near-surface oceanic chlorophyll, *Science*, **334** (6054), 328-332 (2011). doi:10.1126/science.1208897

Clayton, S., Nagai, T., and Follows, M. J., Fine scale phytoplankton community structure across the Kuroshio Front, *J. Plankton Res.*, **36**, 1017-1030 (2014). doi:10.1093/plankt/fbu020.

Demidov, A. B., Sheberstov, S. V., Gagarin, V. I., and Khlebopashev, P. V., Seasonal variation of the satellite-derived phytoplankton primary production in the Kara Sea, *Oceanology*, **57**, 91–104 (2017). doi:10.1134/S0001437017010027

Doblin, M. A., and Clayton, M. N., Effect of secondarily-treated sewage effluent on the early life-history stage of two species of brown macroalgae: *Hormosira banksii* and *Durvillaea potatorum*. *Mar. Biolog.* **122**, 689-698 (1995).

Du, C., Liu, Z., Dai, M., Kao, S., Cao, Z., Zhang, Y., Huang, T., Wang, L., and Li, Y., Impact of the Kuroshio intrusion on the nutrient inventory in the upper northern South China Sea: insights from an isopycnal mixing model, *Biogeosciences*, **10**, 6419–6432 (2013). doi:10.5194/bg-10-6419-2013.

Ebuchi, N., and Hanawa, K., Trajectory of mesoscale eddies in the Kuroshio recirculation region, *J. Oceanogr.*, **57**, 471-480 (2001). doi:10.1023/A:1021293822277.

Egbert, G. D., Bennett, A. F., Foreman, M. G.G., TOPEX/POSEIDON tides estimated using a global inverse model. *J. Geophys. Res*. **99**, 24821-24852 (1994).

Egbert, G. D., and Erofeeva, S. Y., Efficient inverse modeling of barotropic ocean tides. J. Atomspher. *Ocean. Technol.* **19**, 183-204 (2002).

Falkowski, P. G., Ziemmann, D., Kolber, Z., and Bienfang, P. K., Role of eddy pumping in enhancing primary production in the ocean, *Nature*, **352**, 55-58 (1991).

Falkowski, P. G., Barber, R. T., and Smetacek, V., Biogeochemical controls and feedbacks on ocean primary production, *Science*, **281** (5374), 200-207 (1998). doi: 10.1126/science.281.5374.200.

Fasham, M. J. R., Ducklow H. W., and McKelvie S. M., A nitrogen-based model of plankton dynamics in the oceanic mixed layer, *J. Mar. Res.*, **48**, 591-639 (1990). doi:10.1357/002224090784984678.

Fiechter, J., Moore, A. M., Edwards, C. A., Bruland, K. W., Lorenzo, E. D., Lewis, C. V.W., Powell, T. M., Curchitser, E. N., and Hedstrom, K., Modeling iron limitation of primary production in the coastal Gulf of Alaska, *Deep-Sea Res. II*, **56**, 2503–2519 (2009). doi:10.1016/j.dsr2.2009.02.010.

Fujiwara, T., and Nakata, H., Flow characteristics governing the distribution of water and bottom quality in a semi-enclosed sea. *Mar. Pollut. Bull.* **23**, 675-678 (1991).

Fujiwara, T., Nakata, H., and Nakatsuji, K., Tidal-jet and votex-pair driving of the residual circulation in a tidal estuary. *Cont. Shelf Res*. **14**, 1025-1038 (1994).

Garcia, H. E., Locarnini, R. A., Boyer, T. P., and Antonov J. I., 2006. *World Ocean Atlas 2005, Volume 4: Nutrients (phosphate, nitrate, and silicate)*, (Ed.), Levitus, S., NOAA Atlas NESDIS 64, U.S. Government Printing Office, Washington, D.C., 396 pp.

Gaube, P., Chelton D. B., Strutton P. G., and Behrenfeld, M. J., Satellite observations of chlorophyll, phytoplankton biomass, and Ekman pumping in nonlinear mesoscale eddies, *J. Geophys. Res. Oceans*, **118**, 6349–6370 (2013). doi:10.1002/2013JC009027.

Gruber, N., Frenzel, H., Doney, S. C., Marchesiello, P., McWilliams, J. C., Moisan, J. R., Oram, J. J., Plattner, G.-K., and Stolzenbach, K. D., Eddy-resolving simulation of plankton ecosystem dynamics in the California Current System, *Deep-Sea Res.*,

539, 1483-1516 (2006). doi:10.1016/j.dsr.2006.06.005.

Guo, X., Futamura, A., and Takeoka, H., Residual currents in semi-enclosed bay of the Seto Inland Sea, Japan. *J. Geophys. Res*. **109**, C12008 (2004). doi:10.1029/2003JC002203.

Hodur, R. M., The naval research laboratory's Coupled Ocean/Atmosphere Mesoscale Prediction System (COAMPS). *Monthly Weath. Rev.* **125**, 1414-1430 (1997).

Honda, S., Nakayama, A., Bricker, J. D., Field survey of advection and diffusion off Tarumi Coast using GPS drifters equipped with conductivity and temperature sensors. *Proc. Coastal Eng. JSCE*. **54**, 346-350 (2007), doi:10.2208/proce1989.54.346 (in Japanese with English abstract)

Imai, I., Yamaguchi M., Hori Y., Eutrophication and occurrences of harmful algal blooms in the Seto Inland Sea, Japan. *Plankt. Benth. Res*. **1:2**, 71-84 (2006).

Imasato, N., A numerical experiment on water and salt exchange through the Akashi and Naruto Straits. *J. Phys. Oceanogr*. **13**, 1526-1533 (1983).

Imasato, N., Fujo, S., Zhang Q., Awaji, T., Akitomo K., Three-dimensional numerical experiments on tidal exchange through a narrow strait in a homogeneous and a stratified sea. *J. Oceanogr*. **50**, 119-139 (1994).

Isobe, A., and Imawaki, S., Annual variation of the Kuroshio transport in a two-layer numerical model with a ridge, *J. Phys. Oceanogr.*, 32, 994-1009 (2002). doi:10.1175/1520-0485(2002)032<0994:AVOTKT>2.0.CO;2.

Isoguchi, O., Shimada, M., Kawamura, H., Characteristics of ocean surface winds in the lee of an isolated island observed by synthetic aperture radar. *Monthly Weath. Rev.* **139**, 1744-1761 (2010).

Kamidaira, Y., Uchiyama Y., Mitarai, S., Eddy-induced transport of the Kuroshio warm water around the Ryukyu Islands in the East China Sea. *Cont. Shelf Res.*, **143**, 206–218 (2017). doi:10.1016/j.csr.2016.07.004.

Kamidaira, Y., Uchiyama, Y., Kawamura, H., Kobayashi, T., and Furuno, A., Submesoscale mixing on initial dilution of radionuclides released from the Fukushima Daiichi Nuclear Power Plant, *J. Geophys. Res. Oceans*, **123**, 2808–2828 (2018). doi:10.1002/2017JC013359.

Kaneko, H., Yasuda, I., Komatsu, K., and Itoh, S., Observations of vertical turbulent nitrate flux across the Kuroshio. *Geophys. Res. Lett.*, **40**, 3123-3127 (2013). doi:10.1029/2012gl052419.

Kasai, A., Kimura, S., Nakata, H., and Okazaki, Y., Entrainment of coastal water into a frontal eddy of the Kuroshio and its biological significance, *J. Mar. Syst.*, **37**, 185-198 (2002). doi:10.1016/S0924-7963(02)00201-4.

Kawabe, M., Spectral properties of sea level and time scale of Kuroshio path variations. *J. Oceanogr. Society Japan* **43**, 111-123 (1987).

Kawabe, M., Variations of current path, velocity, and volume transport of the Kuroshio in relation with the large meander. *J. Phys. Oceanogr.* **25**, 3103-3117 (1995).

Kawai, H., 1972: Hydrography of the Kuroshio Extension. p. 235–354. In Kuroshio—Its Physical Aspects, ed. University of Tokyo Press.

Kimura, S., Kasai, A., Nakata, H., Sugimoto, T., Simpson, J. H., and Cheok, J. V. S., Biological productivity of meso-scale eddies caused by frontal disturbances in the Kuroshio, *ICES J. Mar. Sci.*, **54**, 179-192 (1997). doi:10.1006/jmsc.1996.0209.

Kimura, S., Nakata H., and Okazaki, Y., Biological production in meso-scale eddies caused by frontal disturbances of the Kuroshio Extension, *ICES J. Mar. Sci.*, **57**, 133-142 (2000). doi:10.1006/jmsc.1999.0564.

Kobayashi, S., Hashimoto, E., Hagao, M., and Tokasugi Y., Variations in turbulent energy dissipation and water column stratification at the entrance of a tidally energetic strait. *J. Oceanogr.* **65**, 657-664 (2009).

Kodama, T., Shimizu, Y., Ichikawa, T., Hiroe, Y., Kusaka, A., Morita, H., Shimizu, M., and Hidaka, K., Seasonal and spatial contrast in the surface layer nutrient content around the Kuroshio along 138°E, observed between 2002 and 2013, *J. Oceanogr.*, **70**, 489–503 (2014). doi:10.1007/s10872-014-0245-5.

Kosako, T., Uchiyama, Y., Mitarai S., A multi-year analysis on circulation and associated larval transport in the Seto Inland Sea, Japan. *J. Japan Soc. Civil Eng. Ser. B2*, **72:2**, 1273-1278 (2016). doi:10.2208/kaigan.72.I_1273 (in Japanese with English abstract)

Kouketsu, S., Kaneko, H., Okunishi, T., Sasaoka, K., Itoh, S., Inoue, R., Ueno, H., Mesoscale eddy effects on temporal variability of surface chlorophyll a in the Kuroshio Extension, *J. Oceanogr.*, **72**, 439–451 (2014). doi:10.1007/s10872-015-0286-4.

Kurosawa, K., Uchiyama, Y., and Miyoshi, Y., On improvement of an estuarine reanalysis-forecast model for the Seto Inland Sea based on 3D variational assimilation. *J. Japan Soc. Civil Eng. Ser. B2*, **73:2**, 1,663-1,668 (2017). (in Japanese with English abstract)

Large, W. G., McWilliams, J. C., and Doney, S. C., Oceanic vertical mixing: A review and model with a nonlocal boundary layer parameterization, *Rev. Geophys.*, **32**, 363-403 (1994). doi:10.1029/94RG01872.

Lazzari, P., Solidoro, C., Ibello, V., Salon, S., Teruzzi, A., Béranger, K., Colella, S., and Crise, A., Seasonal and inter-annual variability of plankton chlorophyll and primary production in the Mediterranean Sea: a modelling approach. *Biogeosciences*, **9**, 217-233 (2012). doi:10.5194/bg-9-217-2012.

Lee, E. A., and Kim, S. Y., Regional variability and turbulent characteristics of the satellite-sensed submesoscale surface chlorophyll concentrations, *J. Geophys. Res. Oceans*, **123**, 4250–4279 (2018). doi:10.1029/2017JC013732.

Lemarié, F., Kurian, J., Shchepetkin, A. F., Molemaker, M. J., Colas, F., McWilliams, J. C., Are there inescapable issues prohibiting the use of terrain-following coordinates in climate models?, *Ocean Modell.*, **42**, 57–79 (2012). doi:

10.1016/j.ocemod.2011.11.007.

Li, Y., Wolanski, E., and Zhang, H., What processes control the net currents through shallow straits? A review with application to the Bohai Strait, China. *Estuar. Coast. Shelf Sci.* **158**, 1-11 (2015).

Liu, X., and Levine, N. M., Enhancement of phytoplankton chlorophyll by submesoscale frontal dynamics in the North Pacific Subtropical Gyre, *Geophys. Res. Lett.*, **43**, 1651–1659 (2015). doi:10.1002/ 2015GL066996.

Lomas, M. W., Moran, S. B., Casey, J. R., Bell, D. W., Tiahlo, M., Whitefield, J., Kelly, R. P., Mathis, J. T., and Cokelet, E. D., Spatial and seasonal variability of primary production on the Eastern Bering Sea shelf, *Deep-Sea Res. II*, **65-70**, 126–140 (2012). doi:10.1016/j.dsr2.2012.02.010.

Marchesiello, P., McWilliams, J. C., and Shchepetkin, A., Equilibrium Structure and Dynamics of the California Current System, *J. Phys. Oceanogr.*, **33**, 753-783 (2003). doi:10.1175/1520-0485(2003)33<753:ESADOT>2.0.CO;2.

Maruyama, T., Miura A., and Yoshida, T., The effects of effluent of municipal wastewater on the growth of *Porphyra yezoensis* in the case of static culture. *Bull. Jpn. Soc. Scientif. Fish*. **51:2**, 315-320 (1985). (in Japanese with English abstract)

Mason, E., Molemake, J., Shchepetkin, A. F., Colas, F., McWilliams, J. C., Sangrà, P., Procedures for offline grid nesting in regional ocean models. *Ocean Modell*. **35**, 1-15 (2010).

Miller, T. W., Omori, K., Hamaoka, H., Shibata, J., and Hidejiro, O., Tracing anthropogenic inputs to production in the Seto Inland Sea, Japan – A stable isotope approach. *Mar. Pollut. Bull*. **60**, 1803-1809 (2010).

Mishima, Y., Hoshika, A., and Tanimoto, T., Deposition rates of terrestrial and marine organic carbon in the Osaka Bay, Seto Inland Sea, Japan, determined using carbon and nitrogen stable isotope rations in the sediment. *J. Oceanogr*. **55**, 1–11 (1999).

Miyazawa, Y., Zhang, R., Guo, X., Tamura, H., Ambe, D., Lee, J., Okuno, A., Yoshinari, H., Setou, T., and Komatsu, K., Water Mass Variability in the Western North Pacific Detected in 15-Year Eddy Resolving Ocean Reanalysis. *J. Oceanogr*. **65**, 737-756 (2009).

Moore, C. W., Mills, M. M., Arrigo, K. R., Berman-Frank, I., Bopp, L., Boyd, P. W., Galbraith, E. D., Geider, R. J., Guieu, C., Jaccard, S. L., Jickells, T. D., La Roche, J., Lenton, T. M., Mahowald, N. M., Marañón, E., Marinov, I., Moore, J. K., Nakatsuka, T., Oschlies, A., Saito, M. A., Thingstad, T. F., Tsuda, A., and Ulloa, O., Processes and patterns of oceanic nutrient limitation, *Nature Geoscience*, **6**, 701-710 (2013). doi:10.1038/NGEO1765.

Nagai, T., Tandon, A., Yamazaki, H., Doubell, M. J., and Gallager, S., Direct observations of microscale turbulence and thermohaline structure in the Kuroshio Front, *J. Geophys. Res.*, **117**, C08013 (2012). doi:10.1029/2011JC007228.

Nagai, T., Gruber, N., Frenzel, H., Lachkar, Z, McWilliams, J. C., and Plattner, G.,

Dominant role of eddies and filaments in the offshore transport of carbon and nutrients in the California Current System, *J. Geophys. Res. Oceans*, **120**, 5318–5341 (2015). doi:10.1002/2015JC010889.

Nagai, T., Hasegawa, D., Tanaka, T., Nakamura, H., Tsutsumi, E., Inoue, R., and Ymashiro, T., First Evidence of Coherent Bands of Strong Turbulent Layers Associated with High-Wavenumber Internal- Wave Shear in the Upstream Kuroshio, *Sci. Rep.*, 7, 14555 (2017). doi:10.1038/s41598-017-15167-1.

Nagai, T., Clayton, S., and Uchiyama, Y.: 2019. Multiscale routes to supply nutrients through the Kuroshio nutrient stream, In: Kuroshio Current: Physical, Biogeochemical and Ecosystem Dynamics, Geophysical Monograph Series, Eds: Nagai, T., Saito, H., Suzuki, K. and Takahashi, M., John Wiley & Sons, NY, ISBN:1119428343.

Nakata, H., Kimura, S., Okazaki, Y., and Kasai, A., Implications of meso-scale eddies caused by frontal disturbances of the Kuroshio current for anchovy recruitment, *ICES J. Mar. Sci.*, **57**, 143-152 (2000). doi:10.1006/jmsc.1999.0565.

Nakatsuji, K., Fujiwara, T., and Kurita, H., An estuarine system in semi-enclosed Osaka Bay in Japan, Eds: K. R. Dyer and R. J. Orth, In: *Changes in fluxes in estuaries: implications from science to management*, ECSA22/EFR Symposium, Olsen & Olsen, Fredensborg, Denmark, 79–84 (1994).

Nellemann, C., Corcoran, E., Duarte, C. M., Valdés, L., De Young, C., Fonseca, L., and Grimsditch, G., (Eds.): 2009. *Blue Carbon. A Rapid Response Assessment*, United Nations Environment Programme, GRID-Arendal, Birkeland Trykkeri AS, Norway, 78 pp.

Nakayama, A. and Nizamani, Z., Simulation of near field mixing process in marine disposal of treated sewer water, *ARPN Journal of Engineering and Applied Sciences*, **11:4**, 2205–2210 (2016), ISSN 1819-6608.

Nishibe, Y., Takahashi, K., Shiozaki, T., Kakehi, S., Saito, H., and Furuya, K., Size-fractionated primary production in the Kuroshio Extension and adjacent regions in spring, *J. Oceanogr.*, **71**, 27–40 (2015). doi:10.1007/s10872-014-0258-0.

Nishikawa, H., Yasuda, I., Komatsu, K., Sasaki, H., Sasai, Y., Setou, T., and Shimizu, M., Winter mixed layer depth and spring bloom along the Kuroshio front: implications for the Japanese sardine stock, *Mar. Ecol. Prog. Ser.*, **487**: 217–229 (2013). doi: 10.3354/meps10201.

Niwa, K., and Aguga, Y., Idertification of currently cultivated Porphyra species by PCR-RFLP analysis. *Fish. Sci*. **72**, 143-148 (2006).

Park, K., Kang, C, Kim, K., and Park, J., Role of sea ice on satellite-observed chlorophyll-a concentration variations during spring bloom in the East/Japan sea, *Deep-Sea Res.*, **47**, 34-44 (2014). doi:10.1016/j.dsr.2013.09.002.

Qiu, B., The Kuroshio Extension System: its large-scale variability and role in the midlatitude ocean-atmosphere interaction, *J. Oceanogr.*, 58, 57-75 (2002).

Roads, J., Experimental Weekly to Seasonal U.S. Forecasts with the Regional Spectral Model, *Bull. Amer. Meteor. Soc.*, **85**, 1887L1902 (2004).

Rodriguez, E., Morris, J. E., Belz, J. E., Chapin, E. C., Martin, J. M., Daffer, W., and Hensley, S., 2005. An assessment of the SRTM topographic products. *Technical Report*, Jet Propulsion Laboratory, Pasadena, CA.

Rodriguez, E., Morris, C. S., Belz, J. E., A global assessment of the SRTM performance. *Photogramm. Eng. Rem. Sens*. **72:3**, 249-260 (2006). doi: 10.14358/PERS.72.3.249.

Romero, L., Uchiyama, Y., Ohlmann, C., McWilliams, J. C., and Siegel, D. A., Simulation od particle-pair dispersion in the Southern California coastal zone. *J. Phys. Oceanogr.*, **43**, 1862–1879 (2013). doi: 10.1175/JPO-D-13-011.1.

Sasai, Y., Sasaoka, K., Sasaki, H., and Ishida, A., Seasonal and intra-seasonal variability of chlorophyll-a in the North Pacific: model and satellite data, *J. Earth Sim.*, **8**, 3-11 (2007). doi: 10.32131/jes.8.3.

Sasai, Y., Richards, K. J., Ishida, A., and Sasaki, H., Effects of cyclonic mesoscale eddies on the marine ecosystem in the Kuroshio Extension region using an eddy-resolving coupled physical-biological model, *Ocean Dyn.*, **60**, 693-704 (2010). doi:10.1007/s10236-010-0264-8.

Sasaki, H., Klein, P., Qiu, B., and Sasai, Y., Impact of oceanic-scale interactions on the seasonal modulation of ocean dynamics by the atmosphere, *Nature Commun.*, 5:5636 (2014). doi:10.1038/ncomms6636.

Schimel, D. S., House, J. I., Hibbard, K. A., Bousquet, P., Ciais, P., Peylin, P., Braswell, B. H., Apps, M. J., Baker, D., Bondeau, A., Canadell, J., Churkina, G., Cramer, W., Denning, A. S., Field, C. B., Friedlingstein, P., Goodale, C., Heimann, M., Houghton, R. A., Melillo, J. M., Moore III, B., Murdiyarso, D., Noble, I., Pacala, S. W., Prentice, I. C., Raupach, M. R., Rayner, P. J., Scholes, R. J., Steffen, W. L., and Wirth, C., Recent patterns and mechanisms of carbon exchange by terrestrial ecosystems, *Nature*, **414**, 169-172 (2001). doi: 10.1038/35102500.

Shchepetkin, A. F., and McWilliams, J. C., The regional ocean modeling system (ROMS): a split-explicit, free-surface, topography-following-coordinate oceanic model. *Ocean Modell.* **9**, 347-404 (2005).

Shchepetkin, A. F., and McWilliams, J. C., Computational kernel algorithms for fine-scale, multiprocess, longtime oceanic simulations, In: Temam, R., Tribbia, J. (Eds.), *Handbook of Numerical analysis: Computational Methods for the Ocean and the Atmosphere*. Elsevier, Amsterdam, 119-181 (2008).

Sujimoto, S., and Hanawa, K., Relationship between the path of the Kuroshio in the south of Japan and the path of the Kuroshio Extension in the east, *J. Oceanogr.*, 68, 219-225 (2012). doi:10.1007/s10872-011-0089-1.

Tada, H., Uchiyama, Y., and Masunaga, E., Impacts of two super typhoons on the Kuroshio and marginal seas off the Pacific coast of Japan, *Deep-Sea Res. Part I.*

132, 80–93 (2017), doi: 10.1016/j.dsr.2017.12.007

Takeoka, H., Akiyama, H., and Kikuchi, T., The Kyucho in the Bungo Channel, Japan-Periodic intrusion of oceanic warm water. *J. Oceanogr*. **49**, 369-382 (1993).

Takeoka, H., Progress in Seto Inland Sea research. *J. Oceanogr*. **58**, 93-107 (2002).

Tanaka, T., Hasegawa, D., Yasuda, I., Tsuji, H., Fujio, S., Goto, Y., and Nishioka, J., Enhanced vertical turbulent nitrate flux in the Kuroshio across the Izu Ridge, *J. Oceanogr.*, **75**, 195-203 (2019). doi:10.1007/s10872-018-0500-2.

Terawaki, T., Yoshikawa, K., Yoshida, G., Uchimura, M., and Iseki, K., Ecology and restoration techniques for Sargassum Beds in the Seto Inland Sea, Japan. *Mar. Pollut. Bull.* **47**, 198-201 (2003).

Thomas, L. N., and Lee, C. M., Intensification of ocean fronts by down-front winds, *J. Phys. Oceanogr.*, **35**, 1086-1102 (2005). doi:10.1175/JPO2737.1.

Thomas, L. N., and Taylor, J. R., Reduction of the usable wind-work on the general circulation by forced symmetric instability, *Geophys. Res. Lett.*, **37**, L18606 (2010). doi:10.1029/2010GL044680.

Tomita, A., Nakura, Y., and Ishikawa, T., 2016. New direction for environmental water management. *Mar. Pollut. Bull*. **102**, 323-328.

Tsuge, T., and Washida, T., Economic valuation of the Seto Inland Sea by using an Internet CV survey. *Mar. Pollut. Bull.* **47**, 230-236 (2003).

Tsujimoto, A., Nomura, R., Yasuhara, M., Yamazaki, H., and Yoshikawa, S., Impact of eutrophication on shallow marine benthic foraminifers over the last 150 years in Osaka Bay, Japan. *Mar. Micropaleont*. **60**, 258-268 (2006).

Tsutsumi, E., Matsuno, T., Lien, R., Nakamura, H., Senjyu, T., and Guo, X., Turbulent mixing within the Kuroshio in the Tokara Strait, *J. Geophys. Res. Oceans*, **122**, 7082-7094 (2017). doi:10.1002/2017JC013049.

Uchiyama, Y., McWilliams, J. C., Shchepetkin A. F., Wave-current interaction in an oceanic circulation model with a vortex force formalism: Application to the surf zone. *Ocean Modell*. **34:1-2**, 16-35 (2010). doi:10.1016/j.ocemod.2010.04.002.

Uchiyama, Y., Idica, E. Y., McWilliams, J. C., Stolzenbach, K. D., Wastewater effluent dispersal in Southern California Bays. *Cont. Shelf Res*. **76**, 36-52 (2014).

Uchiyama, Y., Suzue, Y., Yamazaki, H., Eddy-driven nutrient transport and associated upper-ocean primary production along the Kuroshio. *J. Geophys. Res. Oceans*, **122**, 5046–5062 (2017a). doi:10.1002/2017JC012847.

Uchiyama, Y., Kanki, R., Takano, A., Yamazaki, H., Miyazawa, Y., Mesoscale reproducibility in regional ocean modeling with a 3-D stratification estimate based on Aviso-Argo data, *Atmosphere-Ocean*, **55**, 18 pp. (2017b), doi:10.1080/07055900.2017.1399858.

Uchiyama, Y., McWilliams, J. C., Akan C., Three-dimensional transient rip currents: Bathymetric excitation of low-frequency intrinsic variability. *J. Geophys. Res. Oceans*. **122**. (2017c). doi:10.1002/2017JC013005.

Uchiyama, Y., Odani, S., Kashima, M., Kamidaira, Y., and Mitarai, S., Influences of the Kuroshio on interisland remote connectivity of corals across the Nansei Archipelago in the East China Sea, *J. Geophys. Res. Oceans*, **123**, 9245–9265 (2018a). doi: 10.1029/2018JC014017.

Uchiyama, Y., Kanki, R., Takano, A., Yamazaki, H., and Miyazawa, Y., Mesoscale reproducibility in regional ocean modeling with a 3-D stratification estimate based on Aviso-Argo data, *Atmosphere-Ocean*, **56:4**, 212-229 (2018b), doi: 10.1080/07055900.2017.1399858.

Uchiyama, Y., Zhang, X., Suzue, Y., Kosako, T., Miyazawa, Y., and Nakayama, A., Residual effects of treated effluent diversion on a seaweed farm in a tidal strait using a multi-nested high-resolution 3-D circulation-dispersal model, *Mar. Pollut. Bull.*, **130**, 40–54 (2018c). doi:10.1016/j.marpolbul.2018.03.007.

Uitz, J., Claustre, H., Gentili, B., and Stramski, D., Phytoplankton class-specific primary production in the world's oceans: Seasonal and interannual variability from satellite observations, *Global Biogeochem. Cycles*, **24**, GB3016 (2010). doi:10.1029/2009GB003680.

Woodruff, S. D., Slutz, R. J., Jenne, R. L., and Steurer, P. M., A comprehensive ocean-atmosphere data set. *Bull. American Meteorolog. Soc*, **68**, 1239–1250 (1987). doi:10.1175/1520-0477(1987)068<1239:ACOADS>2.0.CO;2.

Yamada, K., Ishizaka, J., Yoo, S., Kim, H., and Chiba, S., Seasonal and interannual variability of sea surface chlorophyll *a* concentration in the Japan/East Sea (JES), *Prog. Oceanogr.*, **61**, 193–211 (2004). doi:10.1016/j.pocean.2004.06.001

Yoo, S., and Kim, H., Suppression and enhancement of the spring bloom in the southwestern East Sea/Japan Sea, *Deep-Sea Res. II*, **51**, 1093–1111 (2003). doi:10.1016/j.dsr2.2003.10.008.

Xu, L., Xie, S., Jing, Z., Wu, L., Liu, Q., Li, P., and Du, Y., Observing subsurface changes of two anticyclonic eddies passing over the Izu-Ogasawara Ridge, *Geophys. Res. Lett.*, **44**, 1857-1865 (2016). doi:10.1002/2016GL072163.

Zhang, X., Uchiyama, Y., and Nakayama, A., On relaxation of the influences of treated sewage effluent on an adjacent seaweed farm in a tidal strait, *Mar. Pollut. Bull.*, **144**, 265–274 (2019). doi:10.1016/j.marpolbul.2019.04.050.

Doctoral Dissertation, Kobe University
Dynamical impacts on marine ecosystem of coastal and marginal seas around Japan, 111 pages

Submitted on January 21, 2021

The date of publication is printed in cover of repository version published in Kobe University Repository Kernel.